



Claudio Ferrara

## High-Fidelity Illumination Modelling and N-Body Trajectory Optimisation for Enceladus Surface Groundtrack Design

Faculty of Engineering and Applied Sciences  
Astronautics and Space Engineering

MSc  
Academic Year: 2024–2025

Supervisors: Prof. J.P. Sanchez Cuartielles, Prof. M.  
Ceccaroni  
September 2025



Faculty of Engineering and Applied Sciences  
Astronautics and Space Engineering

MSc

Academic Year: 2024–2025

Claudio Ferrara

High-Fidelity Illumination Modelling and N-Body Trajectory  
Optimisation for Enceladus Surface Groundtrack Design

Supervisors: Prof. J.P. Sanchez Cuartielles, Prof. M.  
Ceccaroni  
September 2025

This thesis is submitted in partial fulfilment of the  
requirements for the degree of MSc.

© Cranfield University 2025. All rights reserved. No part of  
this publication may be reproduced without the written  
permission of the copyright owner.

## **Academic Integrity Declaration**

I declare that:

- the thesis submitted has been written by me alone.
- the thesis submitted has not been previously submitted to this university or any other.
- that all content, including primary and/or secondary data, is true to the best of my knowledge.
- that all quotations and references have been duly acknowledged according to the requirements of academic research.

I understand that knowingly submit work in violation of the above statement will be considered by examiners as academic misconduct.

# Abstract

The European Space Agency's funded GIGANTES project aims to develop advanced software for designing complex interplanetary tours to the moons of Saturn, with a primary focus on Enceladus. Preliminary mission design within this framework relies on the linked-conics model, a computationally efficient two-body approximation. However, two significant limitations arise when transitioning to high-fidelity analysis: trajectories optimised in this simplified model can become unfeasible in an n-body dynamical environment, and the absence of illumination modelling can lead to scientifically unproductive flybys scheduled in darkness.

This thesis addresses these gaps by enhancing the GIGANTES software suite with two critical capabilities. First, a high-fidelity illumination model for Enceladus was developed, which accurately predicts surface lighting conditions by incorporating both the terminator line and, crucially, the frequent and long-lasting eclipses cast by an oblate Saturn. Validation against NASA's SPICE toolkit demonstrated excellent agreement, with eclipse timing accurate to within one second.

Second, an n-body trajectory optimisation algorithm was implemented to bridge the gap between the linked-conics and high-fidelity models. After identifying the principal perturbers of the Enceladus flybys (the Sun, Titan, and Saturn's  $J_2$  zonal harmonic), a differential correction scheme using a State Transition Matrix (STM) and B-plane targeting was developed. This algorithm iteratively adjusts a single Trajectory Correction Manoeuvre (TCM) to ensure the final n-body groundtrack precisely matches the scientific objectives of the initial linked-conics design. The methodology demonstrates reliable convergence,

achieving quasi-ballistic corrections ( $\Delta V < 20$  m/s) that yield groundtracks virtually indistinguishable from their intended targets.

The integrated tools provide mission designers with a robust framework for creating physically realistic and scientifically viable trajectories, ensuring that mission objectives for Enceladus exploration are met with high fidelity. The MATLAB code developed for this research has been published as open-source software.

**Keywords:**

Mission Design, Multiple Gravity Assist (MGA), Astrodynamics, GIGANTES, Linked Conics, B-plane Targeting, State Transition Matrix (STM), Eclipse

# Acknowledgements

I would like to thank my supervisors for their support and guidance throughout this research internship. I am especially grateful to Prof. J.P. Sanchez Cuartielles for the opportunity he gave me to come to ISAE SUPAERO and work on this exciting project. I would also like to thank Prof. M. Ceccaroni for her valuable insights and feedback that greatly improved the quality of this thesis.

I am grateful to my coursemates at Cranfield University and my colleagues at ISAE SUPAERO for their camaraderie and for making this year both productive and enjoyable.

Finally, I want to thank my family and friends for their constant encouragement and belief in me. Their support has been invaluable to me throughout this journey.

# Contents

<b>Academic Integrity Declaration</b>	<b>i</b>
<b>Abstract</b>	<b>ii</b>
<b>Acknowledgements</b>	<b>iv</b>
<b>Contents</b>	<b>v</b>
<b>List of Figures</b>	<b>viii</b>
<b>List of Tables</b>	<b>xii</b>
<b>List of Abbreviations</b>	<b>xiii</b>
<b>1 Introduction</b>	<b>1</b>
1.1 Issues . . . . .	4
1.2 Aim and Objectives . . . . .	6
1.3 Thesis Structure . . . . .	7
<b>2 Illumination</b>	<b>8</b>
2.1 Terminator Shadow . . . . .	9
2.1.1 Derivation of the Terminator Formula . . . . .	9
2.1.1.1 The Topocentric-Horizon Coordinate System (SEZ) .	11
2.1.1.2 Terminator Equation . . . . .	12
2.1.2 EBRF - Enceladus body-fixed reference frame . . . . .	13
2.1.3 Terminator Shadow results and verifications . . . . .	16
2.2 Eclipse shadow . . . . .	19

2.2.1	Earth eclipse classic model . . . . .	19
2.2.2	Saturn eclipse formula . . . . .	20
2.2.3	Saturn eclipse results and verifications . . . . .	23
2.3	Other moon eclipses . . . . .	26
2.3.1	Mathematical Framework . . . . .	26
2.3.1.1	Umbra Height . . . . .	26
2.3.1.2	Eclipse Duration . . . . .	27
2.3.1.3	Eclipse Season Window . . . . .	27
2.3.1.4	Eclipse Opportunities . . . . .	28
2.3.2	Results . . . . .	28
2.4	Illumination final results . . . . .	31
2.4.1	Filtering out eclipses . . . . .	31
2.4.2	Final illumination plots . . . . .	33
<b>3</b>	<b>N-body dynamics</b> . . . . .	<b>36</b>
3.1	Multiple Gravity Assist Modelling . . . . .	38
3.1.1	Linked-Conics Approximation . . . . .	38
3.1.2	Flyby Geometry . . . . .	43
3.2	Main Perturbers of the flyby . . . . .	46
3.2.1	N-body propagator . . . . .	46
3.2.2	Identification of Principal Perturbers . . . . .	48
3.3	Local Groundtrack Convergence . . . . .	51
3.3.1	Existing Literature on Groundtrack Dynamics . . . . .	51
3.3.2	Local Propagation of Groundtracks . . . . .	51
3.4	Global Convergence . . . . .	55
3.4.1	B-plane Fundamentals . . . . .	56
3.4.1.1	B-plane Coordinate System . . . . .	56
3.4.1.2	B-plane Targeting and Computation . . . . .	58
3.4.2	State Transition Matrix (STM) Fundamentals . . . . .	59
3.4.2.1	STM Differential Equation and Gravity Gradient . . . . .	59
3.4.2.2	Gravity Gradient Matrix for Central Body and $J_2$ . . . . .	60

3.4.3	Velocity Correction via Pseudo-Inverse . . . . .	61
3.4.3.1	Formulation of the Correction Problem . . . . .	61
3.4.3.2	Computation of the Sensitivity Matrix . . . . .	62
3.4.4	Iterative Correction Procedure and Verification . . . . .	62
3.4.4.1	True Anomaly-Based Initial Condition Setup . . . . .	63
3.4.4.2	Iterative Correction with Singularity Avoidance . . . . .	63
3.4.4.3	Convergence Criteria and Verification . . . . .	63
3.4.5	Algorithm Summary . . . . .	64
3.4.6	Final Results . . . . .	66
<b>4</b>	<b>Conclusions and future work</b>	<b>72</b>
4.1	Conclusions . . . . .	72
4.2	Future work . . . . .	73
4.2.1	Illumination improvements . . . . .	73
4.2.2	N-body multiple flyby improvements . . . . .	73
4.2.2.1	Multiple only Enceladus flyby . . . . .	74
4.2.2.2	Multiple burns . . . . .	75
<b>References</b>		<b>77</b>
<b>A Ethical Approval Letter</b>		<b>83</b>
<b>B Mathematical Derivation of Saturn's Angular Size</b>		<b>84</b>
B.1	Geometric Setup . . . . .	85
B.2	Tangency Condition . . . . .	87
B.3	Spherical coordinate angles . . . . .	88
B.4	Derivation . . . . .	89
B.5	Verification . . . . .	90
B.5.1	Trigonometric Identity . . . . .	90
B.5.2	Equatorial Direction ( $\beta = 0$ ) . . . . .	91
B.5.3	Polar Direction ( $\beta = 90^\circ$ ) . . . . .	91

# List of Figures

1.1	Cassini image of the southern polar plumes of Enceladus, 2008 [12]. . . . .	2
1.2	Possible mission profiles for Enceladus and Titan. A green mark indicates "can be fully addressed", a yellow mark indicates "can be partially addressed", and a red mark indicates "cannot or cannot be addressed well" by the given mission profile. The starred missions indicate the final candidates and both contain an Enceladus plume sampler. . . . .	3
1.3	Crossing ground-tracks at the near-equatorial latitudes of Enceladus, generated by two sequential partial Crank-over-the-Top (COT) manoeuvres. The trajectory utilizes a 7:1 resonant orbit between the spacecraft and Enceladus, with a relative flyby velocity of 4 km/s. White arrows indicate the latitudinal progression of surface coverage for each sequence: south-to-north for the first partial-COT and north-to-south for the second. . . . .	3
1.4	Ground-tracks for the two solutions involving minimum TOF to achieve Enceladus global mapping at $v_\infty = 0.7$ km/s with (a) 6 flybys and (b) 20 flybys, using a COT sequence with the 7:6 resonance [21]. . . . .	5
1.5	QR code linking to the project GitHub repository: <a href="https://github.com/codscino/GIGANTES_master_thesis">https://github.com/codscino/GIGANTES_master_thesis</a> . . . . .	6
2.1	Terminator shadow on Enceladus [22]. . . . .	9
2.2	Umbra and penumbra diagram [26]. . . . .	10
2.3	The Topocentric-Horizon (SEZ) reference frame [26]. . . . .	11
2.4	Spherical triangle at the observation site [26] . . . . .	12
2.5	Radial reference frame used in GIGANTES . . . . .	13
2.6	ICRF to EBRF transformation [30] . . . . .	14
2.7	Terminator shadow and subsolar point on an Enceladus Mercator projection at Saturn's spring equinox (11 August 2009). . . . .	16
2.8	Umbral and penumbral terminator shadow on an Enceladus Mercator projection . . . . .	17

2.9	Error in subsolar latitude (blue) and longitude (orange) on Enceladus between the developed method and SPICE, evaluated from 2010 to 2020 with 10,000 samples. Spikes correspond to the longitude discontinuity at $\pm 180^\circ$ and are not physically meaningful. . . . .	18
2.10	Terminator shadow and subsolar point on an Enceladus Mercator projection at Saturn's summer solstice (23 May 2017). . . . .	18
2.11	Lit, Umbra and penumbra for an observer on Enceladus. Sizes and proportions are not to scale. . . . .	20
2.12	Schematic representation of the reference frame with Saturn, its radii, and angles. Sizes and proportions are not to scale. . . . .	22
2.13	Illumination map on Enceladus at the start of the Eclipse during Saturn equinox . . . . .	23
2.14	Saturn eclipse onset as seen from Enceladus at 10/05/2025 21:45:23 UTC (Stellarium screenshot). . . . .	24
2.15	Example of a brief rare Titan-induced eclipse on Enceladus, as observed from the surface of the icy moon. Image generated using Stellarium [35]. . . . .	30
2.16	Max phasing angle $\theta_{max}$ to have an eclipse on Enceladus . . . . .	31
2.17	Plots of a flyby during the start of an eclipse. The first plot is the illumination on the groundtrack, the second is the illumination on the whole Enceladus surface. . . . .	34
2.18	Plots of the flyby with selected Sun incidence angles. The first plot is the illumination on the groundtrack, the second is the illumination on the whole Enceladus surface. . . . .	35
3.1	Linked conics flyby representation (adapted from[18]) . . . . .	38
3.2	Hyperbolic flyby geometry[16] . . . . .	39
3.3	Reference frame for the incoming hyperbolic excess velocity, illustrating the turning angle $\delta$ and the angle $\zeta$ [16] . . . . .	41
3.4	Transition from the linked conics approximation to a physically consistent hyperbolic flyby (adapted from [18]). . . . .	42
3.5	Visualisation of the pump ( $\alpha$ ) and crank ( $k$ ) angles for the flyby geometry. $v_{sc}$ is the velocity of the spacecraft in the Saturn-centric reference frame 2.1.2; $v_{ga}$ is the velocity of the gravity-assist body (Enceladus) in the same frame; $v_\infty$ is the hyperbolic excess velocity vector; $r_{ga}$ is the distance from the gravity-assist body(Enceladus) to the central body(Saturn) at the time of the flyby. Adapted from [46]. . . . .	43
3.6	TCN reference frame definition (from ESA MIDAS [13]) . . . . .	44

3.7	Linked-conics reference trajectory for the Enceladus flyby scenario. The positions of Enceladus, Titan, and the spacecraft are shown at the space-craft apocentre. Celestial body sizes are not to scale. . . . .	49
3.8	Principal perturbers of the Enceladus flyby scenario, excluding Enceladus, ranked by the deviation in semi-major axis from the linked-conics solution. The perturbation, measured in kilometres, is evaluated over multiple epochs from 2020 to 2050. . . . .	50
3.9	Comparison of groundtracks from two-body (linked-conics) and $n$ -body propagation over a ten-minute interval around the Enceladus flyby. The maximum altitude considered is 300 km. The two trajectories exhibit a maximum deviation of only $0.01^\circ$ in latitude and $0.4^\circ$ in longitude. The groundtrack corresponds to a first flyby of a COT sequence(see table 3.1).	52
3.10	Cartesian deviation in kilometres between the two-body (linked-conics) and $n$ -body propagation over a ten-minute interval around the Enceladus flyby. The red portion of the plot corresponds to the segment of the flyby below 300 km altitude. The maximum deviation is 19 km. . . . .	53
3.11	Three-dimensional perspective of the flyby. The eccentricity is very high (621.35), and the trajectory appears almost as a straight line. . . . .	54
3.12	B-Plane illustration from Vallado[26] . . . . .	57
3.13	Screenshot of the STM B-plane targeting algorithm outputs in MATLAB command window. The algorithm converges in 10 iterations with a quasi-ballistic $\Delta V$ of 5.45 m/s, 0.832 minutes of flyby epoch difference and a final B-plane error of 0.002 km. The flyby geometry is defined by $\text{node}_{\text{in}} = [4, 8.6918, -86.9406]$ and $\text{node}_{\text{out}} = [4, 8.6918, -88.1610]$ . The periapsis altitude is constrained to be above 10 km; the epoch of the linked-conics flyby is 1 January 2030. The perturbing bodies considered, in addition to Saturn, are Saturn $J_2$ , the Sun, Titan, and Enceladus. . . . .	65
3.14	Results of the STM B-plane targeting algorithm for various backward true anomaly propagations. The flyby geometry is defined by $\text{node}_{\text{in}} = [4, 8.6918, -86.9406]$ and $\text{node}_{\text{out}} = [4, 8.6918, -88.1610]$ . The periapsis altitude is constrained to be above 10 km; the epoch of the linked-conics flyby is 1 January 2030. The perturbing bodies considered, in addition to Saturn, are Saturn $J_2$ , the Sun, Titan, and Enceladus. The upper left plot shows the required $\Delta V$ ; the upper right plot shows the difference in minutes between the periapsis epochs of the $n$ -body and linked-conics solutions; the lower left plot shows the number of iterations to convergence; and the lower right plot shows the final B-plane targeting error. . . . .	66

3.15	Groundtracks and altitude profiles as a function of time from pericentre for a 100-degree true anomaly back-propagation. Three trajectories are shown: the linked-conics solution with the virtual pericentre state propagated in the two-body model (see Sec. 3.1.2), the original $n$ -body trajectory, and the corrected $n$ -body trajectory following STM B-plane targeting (see Algorithm 3.4.5). The maximum altitude considered is 300 km. The maximum deviation between the two trajectories is $0.01^\circ$ in latitude and $0.04^\circ$ in longitude. The groundtrack corresponds to the first flyby of a COT sequence (see Table 3.1). The original $n$ -body trajectory impacts Enceladus. . . . .	69
3.16	Groundtracks and altitude profiles as a function of time from pericentre for a 170-degree true anomaly back-propagation. Two trajectories are shown: the linked-conics solution with the virtual pericentre state propagated in the two-body model (see Sec. 3.1.2) and the corrected $n$ -body trajectory following STM B-plane targeting (see Algorithm 3.4.5), as the original $n$ -body trajectory deviates excessively from the linked-conics solution. Even with a 30-minute difference in flyby epoch, the groundtracks largely overlap. The groundtrack corresponds to the first flyby of a COT sequence (see Table 3.1). . . . .	70
3.17	Visualisation of the three-dimensional flyby scenario using custom-built MATLAB animation software. The snapshot, taken two minutes prior to periapsis, shows that both the linked-conics and original $n$ -body trajectories result in impact with Enceladus, whereas the corrected $n$ -body trajectory avoids collision and satisfies the flyby constraints. Enceladus orbit is represented as multiple black dashed lines, since its orbital elements osculates due to full $n$ -body SPICE ephemeris effects. . . . .	71
B.1	Schematic representation of a spherical Sun and oblate Saturn projected onto the celestial sphere as observed from the surface of Enceladus. Sizes and proportions are not to scale . . . . .	84
B.2	Schematic representation of the reference frame with Saturn, its radii, and angles. Sizes and proportions are not to scale. . . . .	86
B.3	Schematic of the spherical coordinates angles $\delta$ and $\beta$ . . . . .	88
B.4	Right triangle tangent to a spherical body of radius $R$ at a distance $d$ from the observer. . . . .	90

# List of Tables

2.1	Comparison of Methods for Determining Penumbra Contact Time on Enceladus . . . . .	25
2.2	Calculated umbra properties for eclipses on Enceladus by other moons. . . . .	28
2.3	Estimated characteristics of moon-on-Enceladus eclipses per season. . . . .	29
3.1	Initial and final node parameters for the Enceladus flyby scenario. . . . .	48
3.2	Results of the STM B-plane targeting algorithm for various backward true anomaly propagations. The flyby geometry is defined by $\text{node}_{\text{in}} = [4, 8.6918, -86.9406]$ and $\text{node}_{\text{out}} = [4, 8.6918, -88.1610]$ . The periapsis altitude is constrained to be above 10 km; the epoch of the linked-conics flyby is 1 January 2030. The perturbing bodies considered, in addition to Saturn, are Saturn $J_2$ , the Sun, Titan, and Enceladus. . . . .	68
4.1	COT sequence flyby parameters. . . . .	74

# List of Abbreviations

AU	Astronomical Unit
COT	Crank-over-the-Top
EBRF	Enceladus Body-Fixed Reference Frame
ESA	European Space Agency
ET	Ephemeris Time
FEAS	Faculty of Engineering and Applied Sciences
GIGANTES	Giant Planets Tour Design Tools for Orbiter/Lander Applications
GTOC	Global Trajectory Optimisation Competition
ICRF	International Celestial Reference Frame
LHA	Local Hour Angle
MGA	Multiple Gravity Assist
MIDAS	Mission Design and Analysis Suite
MINLP	Mixed-Integer Nonlinear Programming
NASA	National Aeronautics and Space Administration
SEZ	South-East-Zenith
SOI	Sphere of Influence
SPICE	Spacecraft Planet Instrument C-matrix Events
SRP	Solar Radiation Pressure
STEM	Science, Technology, Engineering and Mathematics
STM	State Transition Matrix
TAI	International Atomic Time
TCM	Trajectory Correction Manoeuvre
TCN	Tangential, Cross, Normal
TSP	Travelling Salesman Problem

TT	Terrestrial Time
UTC	Coordinated Universal Time
ZSOI	Zero Sphere of Influence

# Chapter 1

## Introduction

The exploration of the outer Solar System has been profoundly shaped by the discoveries of the joint NASA/ESA Cassini-Huygens mission [1]. Since its arrival in the Saturnian system in 2004, the mission has fundamentally altered the scientific understanding of planetary moons and the potential for habitable environments beyond Earth [2]. The data returned over its 13-year tenure provided an unprecedented characterisation of Saturn’s complex system of rings and moons, with findings that continue to emerge from posterior analysis of its vast dataset [3].

Among the mission’s most significant achievements was the successful descent of the Huygens probe through Titan’s dense, opaque atmosphere in 2005 [4]. This historic event unveiled a complex, Earth-like world with seas and river channels carved by liquid hydrocarbons, offering a unique natural laboratory for studying prebiotic chemistry [5]. Subsequently, during targeted flybys, the Cassini orbiter made the paradigm-shifting discovery of cryovolcanic plumes erupting from the south polar region of the small, icy moon Enceladus [6]. Direct in-situ sampling of these plumes provided compelling evidence of a subsurface, liquid water ocean containing salts and complex organic molecules—key ingredients for life as we know it [7]. More recently, detailed analysis of Cassini’s orbital data has suggested that Mimas, a moon previously considered geologically inert, may also host a young, subsurface global ocean [8].

These groundbreaking discoveries have established the Saturnian system as a prime target in the search for extraterrestrial habitability [9]. In response to these findings, the European Space Agency’s Voyage 2050 Senior Committee has identified the ”Moons of the Giant Planets” as a priority science theme for its next Large-class (L-class) mission [10]. L-class missions represent ESA’s flagship scientific endeavours, designed to address the most ambitious and transformative questions in space science [11].

Within this context, the expert committee has prioritised a future mission to Saturn’s moons, structured around three principal scientific themes [10]. The first objective is to assess the habitability of these ocean worlds through comprehensive characterisation of their internal structure and subsurface oceans. The second is to investigate the mechanisms linking the interior to the near-surface environment, including mass and energy exchanges within the broader moon-planet system. The third theme is to conduct a dir-



Figure 1.1: Cassini image of the southern polar plumes of Enceladus, 2008 [12].

ect search for bio-signatures and prebiotic chemistry within plumes, atmospheres, and on the surfaces, employing both remote and in situ instrumentation. To address these aims, several mission architectures have been proposed, all incorporating an in situ Enceladus plume sampling element, as this offers the most direct means of accessing and analysing material from a potentially habitable extraterrestrial ocean [10].

In this context, the European Space Agency (ESA) initiated the GIGANTES (Giant Planets Tour Design Tools for Orbiter/Lander Applications) project, led by Deimos and ISAE-SUPAERO, to develop an advanced software suite for the design of complex interplanetary tours. The resulting tools are intended for integration into ESA's Mission Design and Analysis Suite (MIDAS) [13]. During the preliminary design phase (Phase A), operational constraints for Enceladus flybys are defined primarily by scientific objectives and Cassini mission heritage [10]. Plume sampling requires a flyby altitude between 10 and 50 km to balance spacecraft safety with sufficient material density for analysis. In-situ mass spectrometers require a relative encounter velocity of 3–5 km/s to preserve complex organic molecules [10]. Additionally, a minimum lead time of one day has been informally specified for any correction manoeuvre prior to the flyby.

GIGANTES provides the computational tools to explore the extensive parameter space of possible mission trajectories, addressing the unique dynamical environment of the Saturian system. It enables mission designers to construct and analyse various architectures, with the "pseudo-orbiter" concept being a principal focus [14]. This architecture employs a long sequence of targeted flybys to achieve extensive scientific characterisation without the spacecraft being gravitationally bound to the moon. By utilising resonant or pseudo-resonant orbits around Saturn, this strategy avoids a propellant-intensive orbit insertion manoeuvre, thus maximising the available mass for the scientific payload and enhancing mission flexibility [14].

The GIGANTES software automates the design of these complex tours. It can generate specific ground-tracks to satisfy scientific coverage requirements and construct specialised sequences, such as 'Crank-over-the-Top' (COT) trajectories (see Fig. 1), to achieve the high-latitude coverage essential for exploring the polar regions of Enceladus [14].

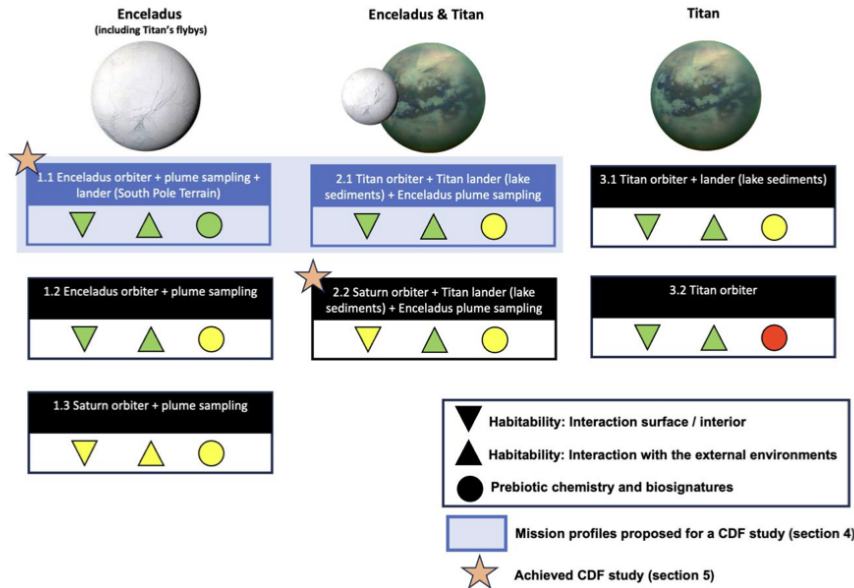


Figure 1.2: Possible mission profiles for Enceladus and Titan. A green mark indicates "can be fully addressed", a yellow mark indicates "can be partially addressed", and a red mark indicates "cannot or cannot be addressed well" by the given mission profile. The starred missions indicate the final candidates and both contain an Enceladus plume sampler.

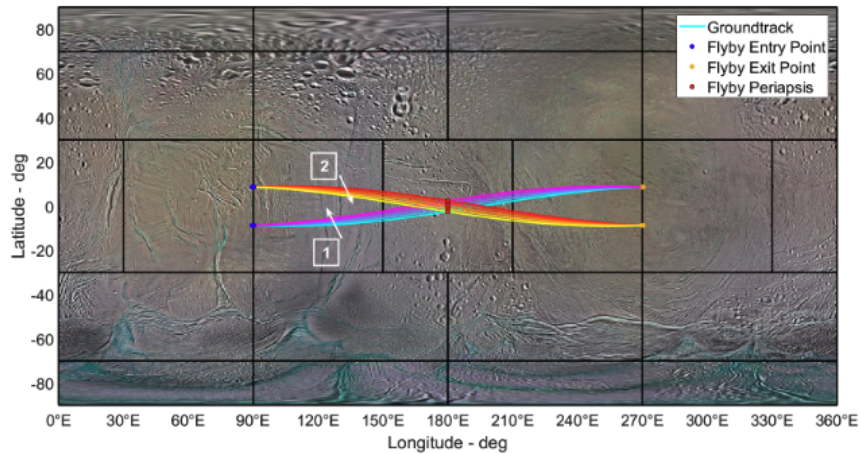


Figure 1.3: Crossing ground-tracks at the near-equatorial latitudes of Enceladus, generated by two sequential partial Crank-over-the-Top (COT) manoeuvres. The trajectory utilizes a 7:1 resonant orbit between the spacecraft and Enceladus, with a relative flyby velocity of 4 km/s. White arrows indicate the latitudinal progression of surface coverage: south-to-north for the first partial-COT and north-to-south for the second.

## 1.1 Issues

A primary objective within the GIGANTES framework is the design of intricate Multiple Gravity Assist (MGA) trajectories for Enceladus exploration.

This design challenge is a specialised instance of the multi-target mission problem, analogous to the "Travelling Salesman Problem" (TSP) in astrodynamics [15], where each "city" is a sequential Enceladus flyby. Formulated as a mixed-integer nonlinear programming (MINLP) task [16], it involves selecting the optimal sequence of flyby parameters and computing the corresponding orbital transfers. Due to the combinatorial explosion of possible solutions, exhaustive high-fidelity analysis is infeasible. GIGANTES addresses this by efficiently linking individual flyby nodes using the linked conics model [17], a limiting case of the patched conic approximation where the sphere of influence is reduced to a point (zero sphere of influence, ZSOI) [18]. This simplification, justified by Saturn's dominant mass, models each flyby as an instantaneous rotation of the spacecraft's velocity vector ( $v_\infty$ ) at the moon's position, enabling rapid exploration of dynamically feasible trajectory families.

However, a significant limitation emerges when transitioning from the simplified two-body linked-conics approach to a high-fidelity n-body model, such as that implemented in ESA GODOT [19]. Solutions optimised within the linked-conics framework may become infeasible in the n-body context: the actual flyby groundtrack can deviate substantially from the two-body prediction, potentially failing to satisfy scientific requirements or even resulting in a missed flyby due to Enceladus's small size. This discrepancy arises because the solver treats flyby parameters as independent of arrival time; even a small timing error can cause the spacecraft to miss Enceladus entirely, given its limited sphere of influence [20].

These trajectory feasibility challenges represent just one aspect of the broader mission design problem. Multiple Gravity Assists (MGA) have been instrumental in designing missions to map moons in our solar system. A notable example is the work of Sanchez and Garcia [21] for the 6th Global Trajectory Optimisation Competition (GTOC6), where they developed a mapping algorithm specifically for Enceladus. The image above illustrates two potential solutions from such an optimisation (see Fig. 1.4). However, a critical limitation in their analysis was the lack of consideration for illumination conditions during flybys, which are essential for imaging and surface mapping. The current GIGANTES framework also does not incorporate these illumination constraints, which could lead to suboptimal or infeasible mission designs.

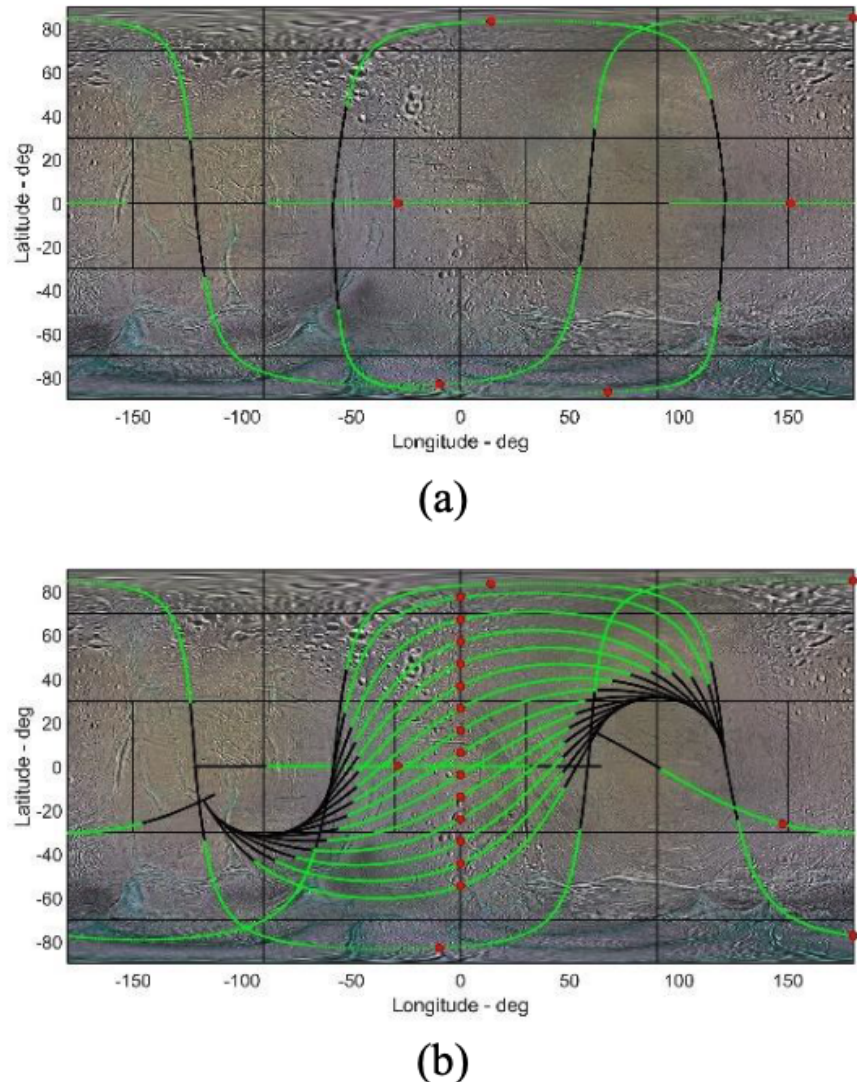


Figure 1.4: Ground-tracks for the two solutions involving minimum TOF to achieve Enceladus global mapping at  $v_\infty = 0.7$  km/s with (a) 6 flybys and (b) 20 flybys, using a COT sequence with the 7:6 resonance [21].

## 1.2 Aim and Objectives

In response to the identified issues, this thesis was undertaken as a research internship within the GIGANTES project at ISAE SUPAERO, Toulouse, under the supervision of Prof. J.P. Sanchez Cuartielles and Prof. M. Ceccaroni, with the objective of refining existing tools and methodologies. The principal aim is to enhance the GIGANTES software suite by integrating high-fidelity illumination modelling and n-body flyby trajectory optimising capabilities.

To achieve this aim, the following objectives were established:

- Develop a high-fidelity illumination model for Enceladus capable of accurately predicting surface lighting conditions by incorporating both the terminator line and eclipses cast by Saturn.
- Upgrade existing two-body trajectory models, which assume circular and coplanar orbits, to instead utilize high-precision SPICE kernels and ephemerides for a more realistic initial trajectory estimation.
- Implement an n-body flyby trajectory optimisation algorithm to refine initial solutions from the linked-conics model, ensuring that the final groundtracks satisfy mission scientific requirements.
- Publish the MATLAB code developed during this research internship as open-source software on GitHub: [https://github.com/codscino/GIGANTES\\_master\\_thesis](https://github.com/codscino/GIGANTES_master_thesis).



Figure 1.5: QR code linking to the project GitHub repository: [https://github.com/codscino/GIGANTES\\_master\\_thesis](https://github.com/codscino/GIGANTES_master_thesis).

## 1.3 Thesis Structure

This thesis is organised into four main chapters, supplemented by an appendix.

- **Chapter 1: Introduction** sets the scientific context for the exploration of Saturn’s moons, highlighting the discoveries of the Cassini-Huygens mission and the objectives of the GIGANTES project. It identifies the key issues with existing trajectory design models, namely the lack of high-fidelity illumination constraints and the discrepancies between simplified and n-body dynamical models. The chapter concludes by defining the aim and objectives of this research.
- **Chapter 2: Illumination** addresses the development of a high-fidelity illumination model for Enceladus. This chapter details the analytical derivation of the terminator line, the formulation of a model for eclipses cast by an oblate Saturn, and an analysis of the negligible impact of eclipses from other moons. It concludes by presenting the integrated model’s application to generating accurate surface illumination maps for mission planning.
- **Chapter 3: N-body Dynamics** focuses on refining the trajectory optimisation process. It begins by describing the linked-conics approximation used in preliminary mission design. It then identifies the principal gravitational perturbers in the Saturnian system to construct an efficient n-body model. The core of the chapter is the implementation of a differential correction algorithm, using B-plane targeting and the State Transition Matrix (STM), to converge initial two-body solutions to be feasible in a high-fidelity n-body environment.
- **Chapter 4: Conclusions and Future Work** summarises the main achievements of the thesis, reviewing the successful integration of the illumination and n-body optimisation capabilities into the GIGANTES framework. It concludes by outlining promising directions for future research, including the extension of the optimisation algorithm to handle multiple-flyby sequences and the incorporation of advanced multi-burn optimisation techniques using primer vector theory.
- **Appendices** A detailed mathematical derivation of the formula for Saturn’s angular size as seen from Enceladus, which is a key component of the eclipse model.

# Chapter 2

## Illumination

This chapter addresses the first objective of the thesis: the accurate determination of surface illumination on Enceladus, which is essential for mapping purposes. Illumination modelling is inherently complex, as it is affected not only by the terminator shadow but also by eclipses, which must be considered due to the unique geometric configuration of the Enceladus–Saturn–Sun system.

Two principal methodological approaches may be adopted:

1. A faster development approach that leverages existing SPICE routines for shadow and illumination calculations.
2. A more comprehensive approach involving the development of a custom illumination model, tailored to the specific requirements of this investigation.

A hybrid strategy has been selected for this work. The primary logic and algorithms have been developed independently to facilitate future reimplementation in C++ by Deimos software navigation team [14]. Nevertheless, SPICE routines and modified SPICE kernels have been employed for rigorous verification and validation of the results.

Accordingly, the structure of this chapter is as follows:

- 2.1 **Terminator Shadow:** Derivation and implementation of the analytical formula for the terminator line on Enceladus, including necessary reference frame definitions and validation against SPICE routines.
- 2.2 **Saturn-Induced Eclipses:** Development of a model to compute the shadow cast by Saturn on Enceladus, accounting for Saturn’s oblateness and the geometric configuration of the system.
- 2.3 **Minor Eclipses:** Assessment of the relevance of eclipses caused by Saturn’s other moons, with justification for their exclusion in the analysis.
- 2.4 **Final Illumination Results:** Integration of the terminator and eclipse models to generate comprehensive surface illumination maps along groundtracks, with discussion of filtering strategies and visualisation options.

## 2.1 Terminator Shadow

The primary source of shadow on Enceladus' surface is the terminator, which separates the illuminated and non-illuminated hemispheres. This section outlines the derivation of the terminator line formula, its verification, and its application.

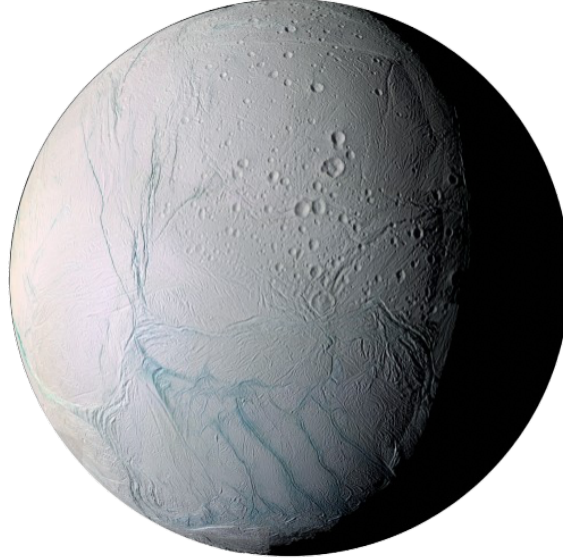


Figure 2.1: Terminator shadow on Enceladus [22].

### 2.1.1 Derivation of the Terminator Formula

The terminator can be conceptually defined as the locus of points on a celestial body's surface where the Sun is exactly at the horizon [23]. To translate this concept into a mathematical formula, it is necessary to first establish the appropriate coordinate systems for defining the positions of an observer on the surface and the Sun.

The derivation relies on two key simplifications:

1. **Enceladus is modelled as a perfect sphere.** This introduces a minor inaccuracy, as Enceladus exhibits an oblateness of approximately 2% [24], compared to Earth's 0.335%. The implications of this simplification are discussed in subsection 2.1.3.
2. **The Sun is treated as a point source at infinite distance.** This results in parallel incident solar rays, a standard assumption for Earth [25] and even more justified for Enceladus, which is roughly ten times farther from the Sun.

The validity of the second simplification can be demonstrated using the equations provided by Vallado (2013) [26]. The umbral and penumbral angles are nearly identical for Enceladus, thereby justifying the neglect of the penumbral region in subsequent analyses. Specifically:

$$\begin{aligned}\alpha_{\text{umb}} &= \arcsin\left(\frac{r_s - r_p}{R_p}\right) = 0.02781^\circ \\ \alpha_{\text{pen}} &= \arcsin\left(\frac{r_s + r_p}{R_p}\right) = 0.02783^\circ\end{aligned}\quad (2.1)$$

where:

- $r_s$  is the radius of the Sun (696,340 km).
- $r_p$  is the radius of Enceladus (252 km).
- $R_p$  is the distance from the Sun to Enceladus ( $1.5 \times 10^9$  km).

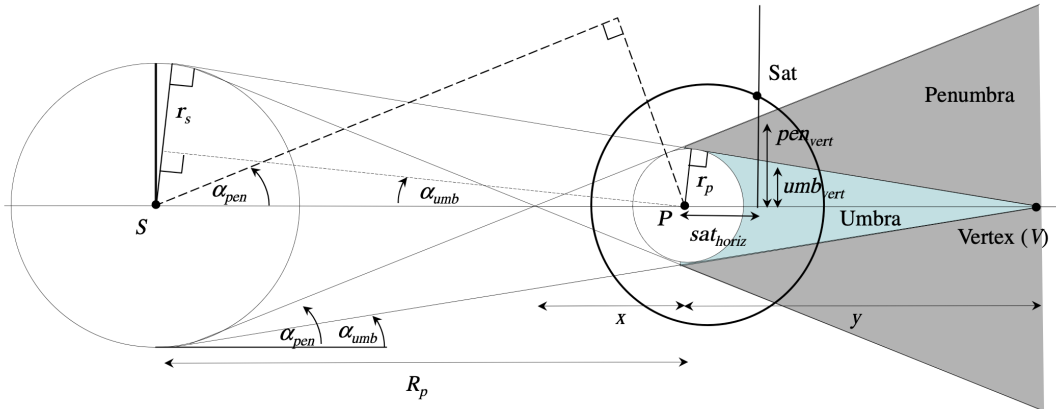


Figure 2.2: Umbra and penumbra diagram [26].

With these assumptions, the derivation begins by defining a local reference frame to describe the Sun's position from the perspective of a surface observer.

### 2.1.1.1 The Topocentric-Horizon Coordinate System (SEZ)

To define the position of the Sun relative to an observer on Enceladus, we use the **Topocentric-Horizon Coordinate System (SEZ)**. This is a local frame centred on the observer.

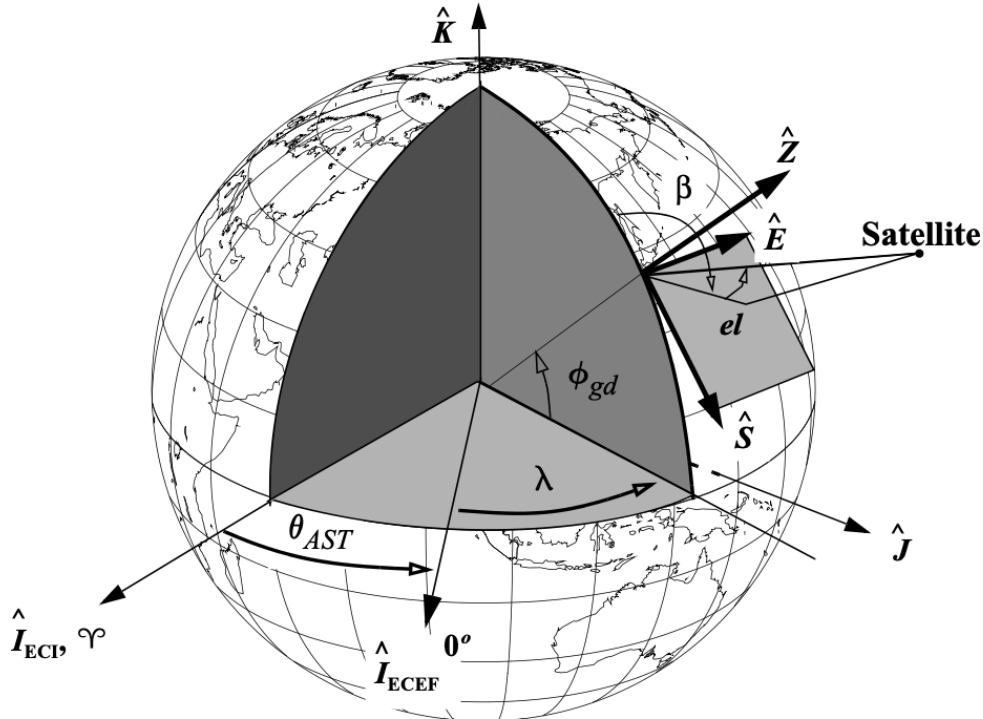


Figure 2.3: The Topocentric-Horizon (SEZ) reference frame [26].

In the SEZ (South-East-Zenith) frame:

- The  $S$  axis points towards the south.
- The  $E$  axis points towards the east.
- The  $Z$  (zenith) axis points radially outward from the observation site, normal to the local surface.

Within this frame, the Sun's position is described by two angles:

- **Azimuth ( $\beta$ ):** The angle measured clockwise from the north, ranging from  $0^\circ$  to  $360^\circ$ .
- **Elevation ( $el$ ):** The angle measured from the local horizon plane. It ranges from  $-90^\circ$  (nadir) to  $+90^\circ$  (zenith) and is positive when the object is above the horizon.

The **elevation angle is the key parameter for our derivation**, as the terminator is precisely the set of points where the Sun's elevation is zero.

### 2.1.1.2 Terminator Equation

The elevation angle ( $el$ ) of the Sun for an observer at a given location can be calculated using the spherical triangle relation shown in Figure 2.4.

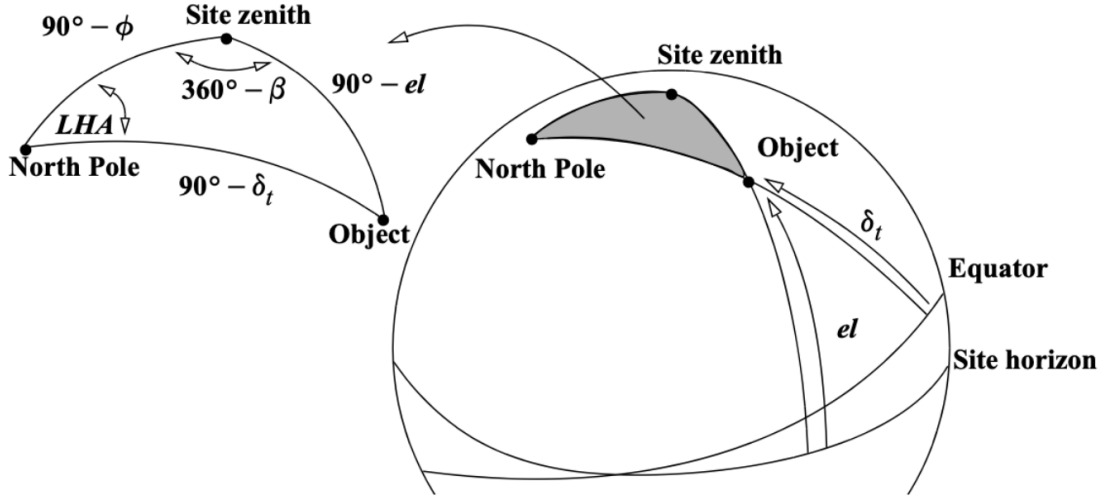


Figure 2.4: Spherical triangle at the observation site [26]

The relationship is given by:

$$\sin(el) = \sin(\phi) \sin(\delta_t) + \cos(\phi) \cos(\delta_t) \cos(LHA) \quad (2.2)$$

where:

- $\phi$ : Observer's latitude.
- $\delta_t$ : Sun's declination.
- $LHA$ : Local Hour Angle, which represents the angular distance between the observer's meridian and the Sun's meridian.

By definition, the terminator is where the Sun is on the horizon [23], so the elevation angle  $el$  is set equal to zero. Equation 2.2 then becomes:

$$0 = \sin(\phi) \sin(\delta_t) + \cos(\phi) \cos(\delta_t) \cos(LHA)$$

Rearranging this equation to solve for the observer's latitude ( $\phi$ ) gives the formula for the terminator line:

$$\phi = \arctan \left( -\frac{\cos(LHA)}{\tan(\delta_t)} \right) \quad (2.3)$$

### 2.1.2 EBRF - Enceladus body-fixed reference frame

To plot the terminator line using Eq. 2.3 an EBRF is required for defining the subsolar point coordinates ( $\phi_{\text{sun}}, \lambda_{\text{sun}}$ ).

The GIGANTES toolbox adopts an EBRF based on two principal assumptions: (1) Enceladus follows a circular, coplanar orbit around Saturn, and (2) Enceladus is tidally locked [27] to Saturn. Under these assumptions, the reference frame is defined as follows:

- The  $X$  axis points from Enceladus centre to Saturn centre.
- The  $Y$  axis is oriented in the direction of Enceladus' orbital motion, tangential to the orbit.
- The  $Z$  axis is perpendicular to the orbital plane, completing the right-handed coordinate system.

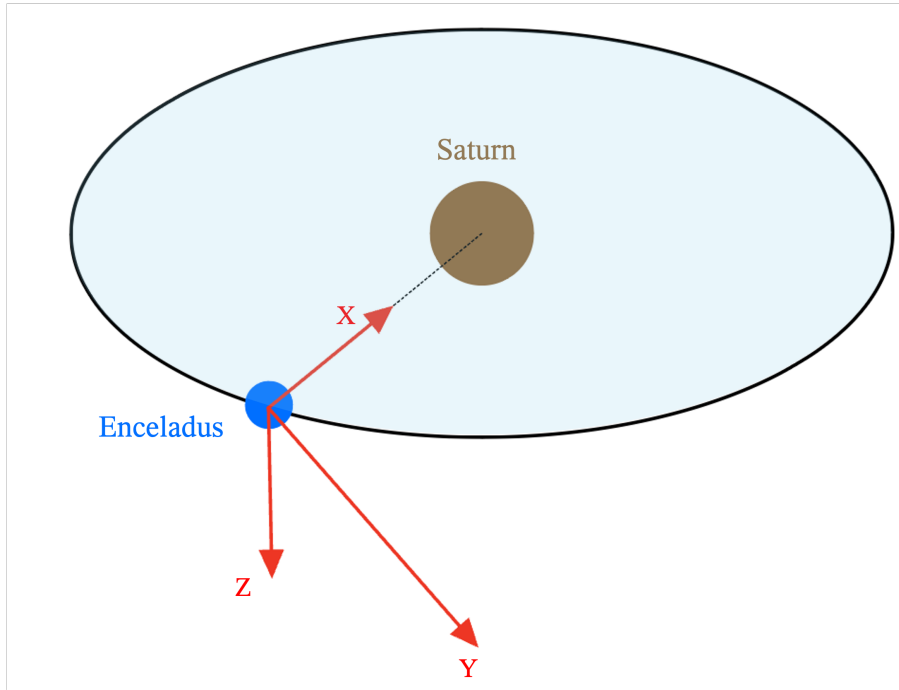


Figure 2.5: Radial reference frame used in GIGANTES

For rigorous verification with SPICE, it is preferable to adopt the same reference frame as used by SPICE. Strict adherence to the simplified GIGANTES body-fixed reference frame would introduce errors due to its underlying assumptions, which are not fully accurate. Specifically, (1) Enceladus has a small but non-negligible orbital eccentricity of 0.0045 [28], and (2) the moon is not perfectly tidally locked to Saturn owing to libration effects [27]. Nonetheless, this reference frame is relevant for the n-body dynamics analysis in Chapter 3 where it has been adopted to be consistent with the rest of GIGANTES libraries.

To ensure consistency with SPICE calculations, we therefore adopt the NAIF reference frame convention used by SPICE. In this framework, the body-fixed reference frame is established through a sequence of three passive Euler angle rotations from ICRF:

$$R_3(W) \cdot R_1\left(\frac{\pi}{2} - \delta_0\right) \cdot R_3\left(\frac{\pi}{2} + \alpha_0\right) \quad (2.4)$$

where:

- $\alpha_0$  is the right ascension of the body's North Pole, expressed as a function of time.
- $\delta_0$  is the declination of the body's North Pole, also time-dependent.
- $W$  is the prime meridian location, representing a rotation about the North Pole and varying with time.
- $R_i(\theta)$  denotes a passive rotation of the reference frame by an angle  $\theta$  about the  $i$ -th coordinate axis [29].

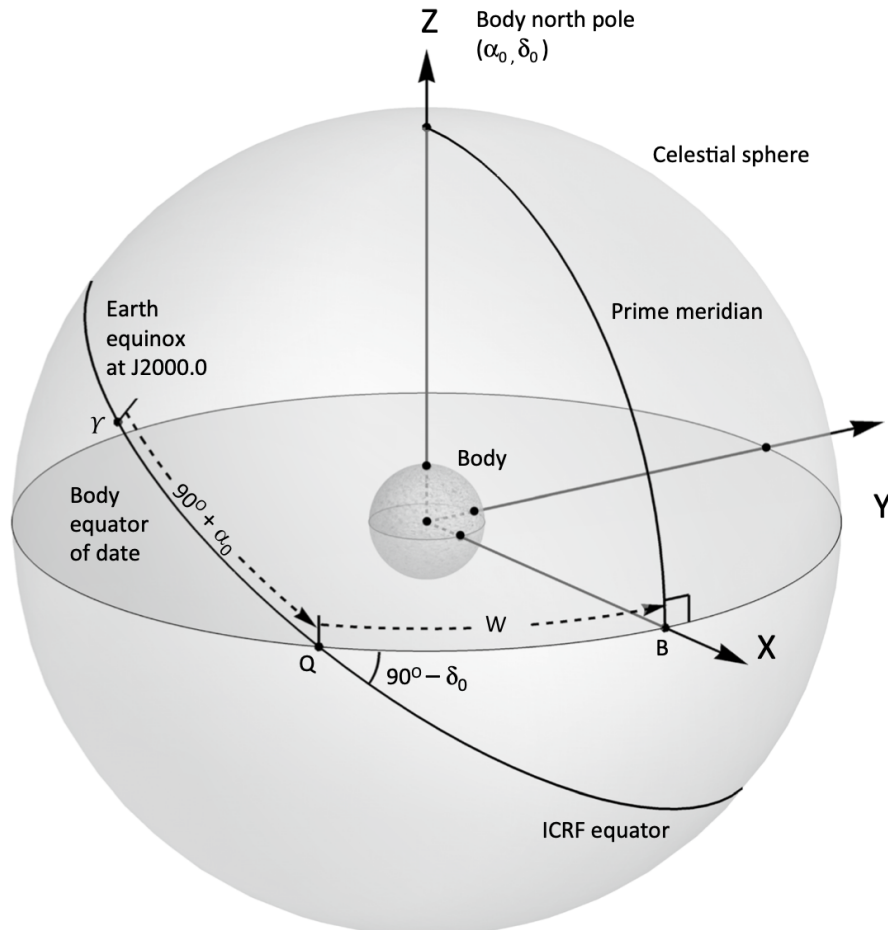


Figure 2.6: ICRF to EBRF transformation [30]

The definition of this reference system is non-trivial, as each of the three Euler angles is expressed as a harmonic series comprising 17–18 terms [27]:

$$\begin{aligned}\alpha(t) &= \alpha_0 + \dot{\alpha}_0 t + \sum_{j=1}^q A_j \sin(\dot{\Omega}_j t + \Omega_j) \\ \delta(t) &= \delta_0 + \dot{\delta}_0 t + \sum_{j=1}^q B_j \cos(\dot{\Omega}_j t + \Omega_j) \\ W(t) &= W_0 + \dot{W}_0 d + \sum_{j=1}^q C_j \sin(\dot{\Omega}_j t + \Omega_j)\end{aligned}\quad (2.5)$$

Where:

- $\alpha_0, \delta_0, W_0$  are constant terms.
- $\dot{\alpha}_0, \dot{\delta}_0, \dot{W}_0$  are rate terms.
- $q$  is the number of terms in the nutation series.
- $A_j, B_j, C_j$  are nutation amplitudes.
- $\dot{\Omega}_j$  is the nutation frequency.
- $\Omega_j$  is the nutation phase.
- $t$  is the time in seconds since J2000.
- $d$  is the time in days since J2000.

Of particular note is the parameter  $W_0$ , which is defined by the location of the small crater Salih, situated at a longitude of  $-5^\circ$ . Determining an absolute value for  $W_0$  is non-trivial, as values reported in the literature [27] [30] [31] can vary by up to  $2^\circ$ . For the purposes of this thesis,  $W_0 = 7.120600$  is adopted, consistent with the value utilised by the SPICE kernel.

Given the reference frame definition, the Sun's coordinates in EBRF can be computed directly. The subsolar latitude and longitude are then obtained by converting the Sun's position vector as follows (assuming a spherical Enceladus):

$$\begin{aligned}\phi_{\text{sun}} &= \arcsin(u_{\text{sun},z}) \\ \lambda_{\text{sun}} &= \arctan2(u_{\text{sun},y}, u_{\text{sun},x})\end{aligned}\quad (2.6)$$

where  $\mathbf{u}_{\text{sun}} = [u_{\text{sun},x}, u_{\text{sun},y}, u_{\text{sun},z}]^T$  is the Sun unit vector in EBRF.

### 2.1.3 Terminator Shadow results and verifications

The methodology outlined in the preceding subsection enables the computation of the terminator line for any specified epoch. In order:

1. Given an epoch, determine the ICRF Sun position using SPICE.
2. Transform the Sun position from ICRF to EBRF using equation 2.4.
3. Determine the subsolar point coordinates ( $\phi_{\text{sun}}, \lambda_{\text{sun}}$ ) via equation 2.3.
4. Obtain the latitude of the terminator as a function of longitude by evaluating equation 2.3 over the desired range of longitudes.

The methodology described above has been implemented in a dedicated MATLAB function. **Preliminary qualitative verifications** have been conducted using this implementation to ensure the correctness of the approach.

Firstly, the behaviour of the terminator at Saturn equinox was examined. At this epoch, the subsolar latitude is zero, and the terminator is expected to manifest as a straight line extending from pole to pole. The results, depicted in Figure 2.7, confirm this expectation.

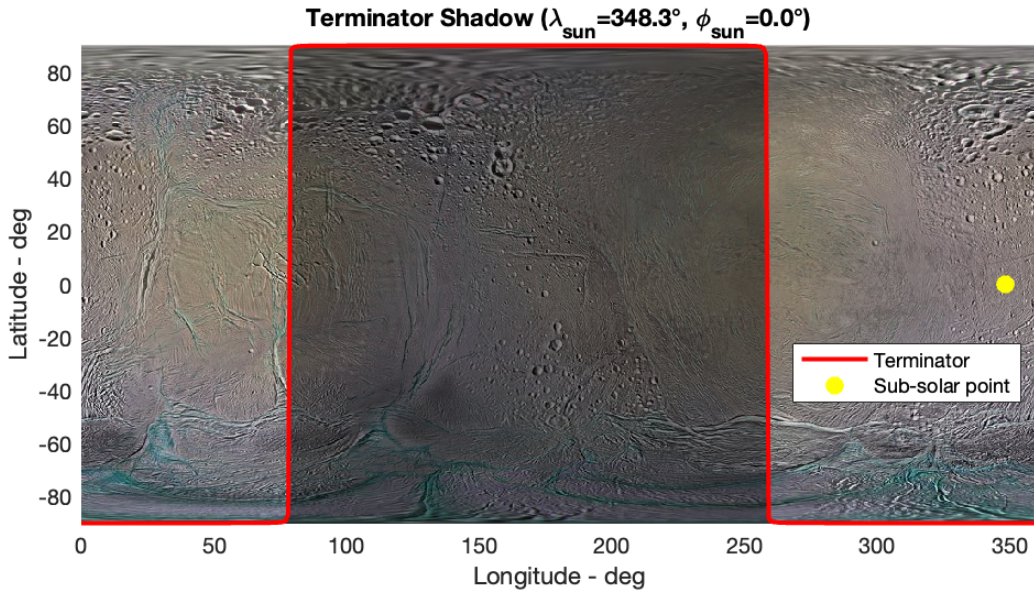


Figure 2.7: Terminator shadow and subsolar point on an Enceladus Mercator projection at Saturn’s spring equinox (11 August 2009).

Secondly, the terminator was evaluated at solstice, when the subsolar latitude attains its maximum value. Given that Enceladus' orbital plane is nearly coincident with Saturn's equatorial plane, the maximum subsolar latitude should correspond to Saturn's obliquity with respect to the ecliptic, approximately  $26.72^\circ$  [20]. The results, depicted in Figure 2.8, confirm this expectation.

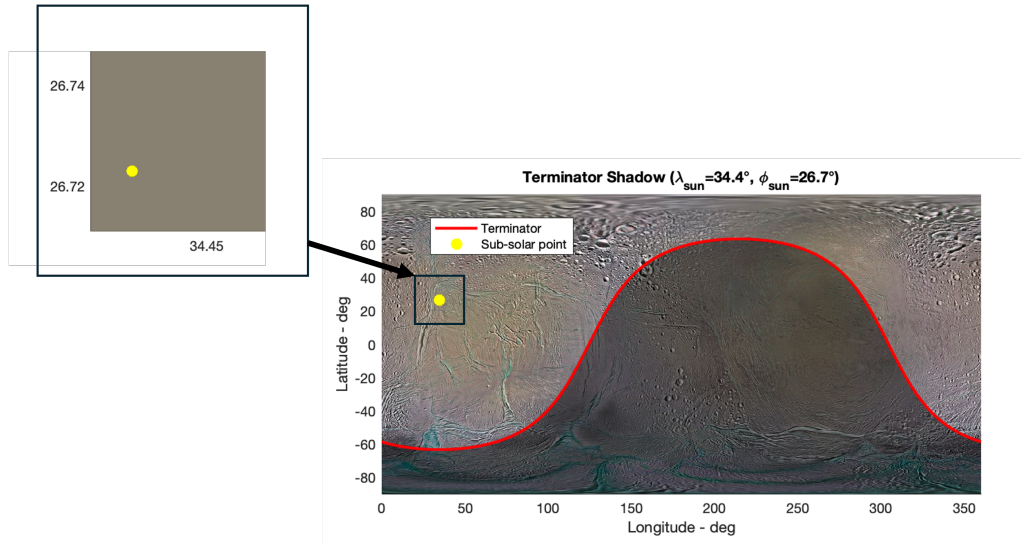


Figure 2.8: Umbral and penumbral terminator shadow on an Enceladus Mercator projection

Further **rigorous validations** of the methodology have been conducted **using the SPICE toolkit**.

Firstly, the subsolar point coordinates derived from the developed approach were compared with those obtained from the `cspice_subslr` [32] SPICE routine, employing a modified Enceladus kernel in which all three principal radii were set to the mean volumetric radius of 252 km to conform to the spherical Enceladus hypothesis. Under these conditions, both the subsolar longitude ( $\lambda_{\text{sun}}$ ) and latitude ( $\phi_{\text{sun}}$ ) exhibited discrepancies of less than  $10^{-10}$  degrees (see details in Fig. 2.9), thereby confirming the accuracy of the method.

Secondly, the same verification was performed using the original kernel, where the three radii assume slightly different values (256.14 km, 251.16 km, and 248.68 km), using planetodetic (ellipsoidal) coordinates. In this case, an error of  $1.05^\circ$  was observed for  $\lambda_{\text{sun}}$  and of  $0.29^\circ$  for  $\phi_{\text{sun}}$ . This result indicates that the spherical approximation does not hold perfectly for Enceladus, and that a more accurate ellipsoidal model should be adopted for higher-fidelity simulations of the moon's surface.

Finally, the SPICE routine `cspice_edterm` [33] was utilised to plot both the umbral and penumbral terminator lines. As illustrated in Figure 2.10, the discrepancy between the analytical and SPICE-derived terminators is minimal (less than  $0.01^\circ$ ), thereby demonstrating that the assumption of parallel solar rays at infinite distance is well justified for Enceladus.

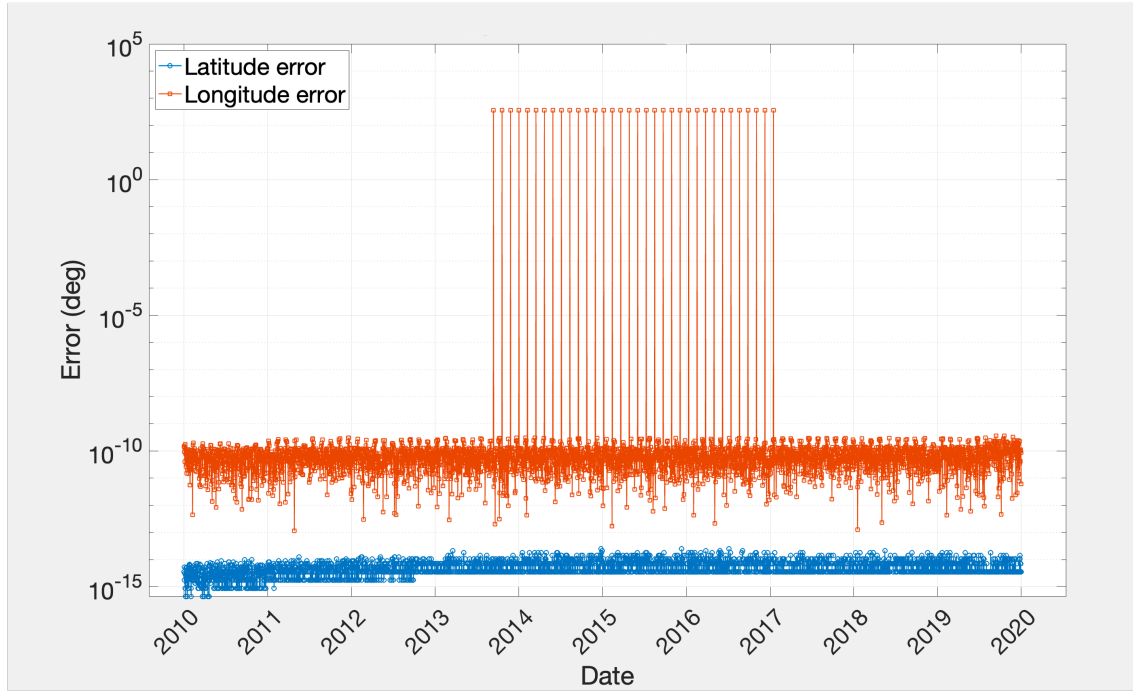


Figure 2.9: Error in subsolar latitude (blue) and longitude (orange) on Enceladus between the developed method and SPICE, evaluated from 2010 to 2020 with 10,000 samples. Spikes correspond to the longitude discontinuity at  $\pm 180^\circ$  and are not physically meaningful.

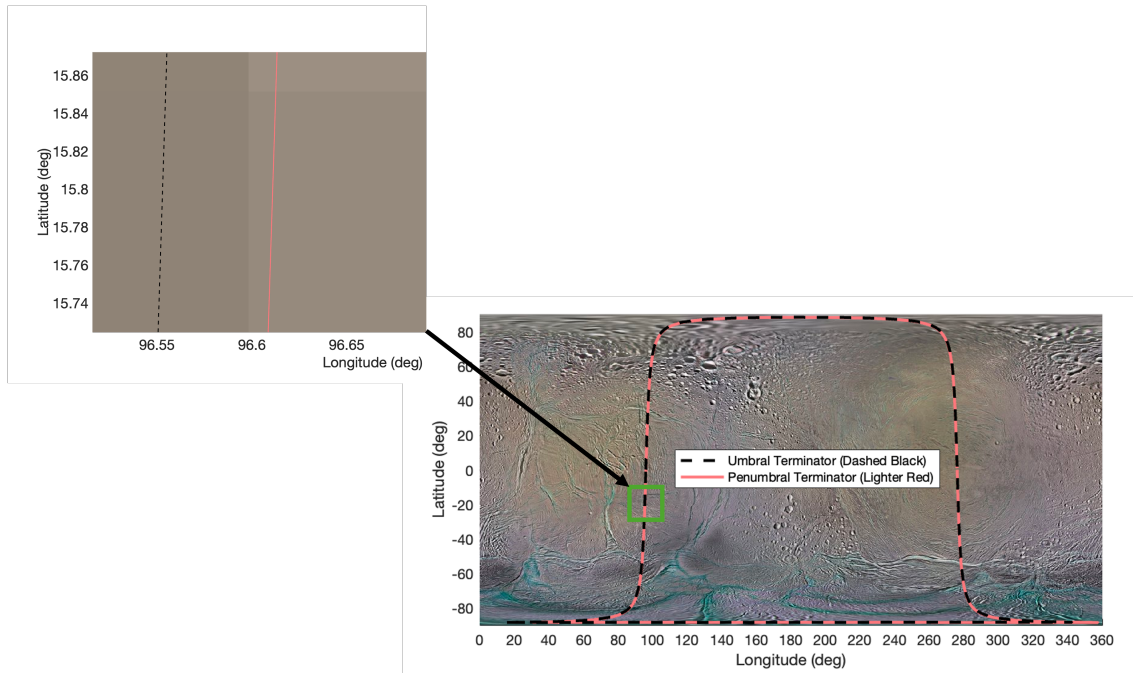


Figure 2.10: Terminator shadow and subsolar point on an Enceladus Mercator projection at Saturn's summer solstice (23 May 2017).

## 2.2 Eclipse shadow

In the classic Earth Moon configuration, lunar eclipses, which occur when the central planet casts a full shadow on its moon, are rare events that take place fewer than 3 times per year [34]. Accounting for them is typically reserved for advanced stages of mission analysis. This rarity is due to the Moon’s orbital plane being inclined by approximately five degrees with respect to Earth’s equator, making Sun Earth Moon alignments infrequent.

By contrast, in the Enceladus–Saturn system, eclipses occur much more frequently. Enceladus orbits nearly in Saturn’s equatorial plane, and Saturn subtends a much larger angular diameter as seen from Enceladus than the Moon does from Earth ( $28^\circ$  versus  $0.5^\circ$ , as calculated in Stellarium [35]). A qualitative estimate of eclipse frequency was obtained using the astronomical software Celestia [36]. The results indicate that:

- Eclipses have a maximum duration of 2h 43min during equinox.
- Within approximately  $\pm 3$  years of equinox, eclipses occur once every Enceladus rotation around Saturn (31.5 hours).

Eclipses caused by Saturn’s rings and other moons are expected to be negligible due to their greater distance and smaller size, but a qualitative analysis has been performed to confirm this assumption (see subsection 2.3).

### 2.2.1 Earth eclipse classic model

To effectively model the complex and frequent eclipses in the Saturn–Enceladus system, it is instructive to first review the established techniques for the Earth–Moon configuration, which serve as a well-understood baseline. Eclipse phenomena for the Earth and Moon have been extensively addressed in the literature [37], [38]. The prediction of lunar eclipses relies on modelling the Moon’s passage through the Earth’s shadow, which, at the Moon’s distance, is typically approximated as a circular cross-section.

A prominent analytical technique for this problem, originally developed for solar eclipses by Friedrich Bessel, involves the use of Besselian elements. This method establishes a coordinate system on a ‘fundamental plane’ passing through the Earth’s center and oriented perpendicular to the axis of the shadow cone. The Besselian elements are a set of time-dependent variables that describe the motion of the center of the Moon relative to the center of the Earth’s circular shadow, as well as the radii of the umbral and penumbral shadows on this plane. These elements typically include:

- $x, y$ : The coordinates of the center of the Moon relative to the shadow axis in the fundamental plane.
- $d$ : The declination of the shadow’s axis.
- $\mu$ : The hour angle of the shadow’s axis.

- $f_1, f_2$ : The angular radii of the penumbral and umbral shadow cones.

By evaluating these elements, astronomers can accurately determine the key moments of an eclipse, such as the times of first and last contact and the time of greatest eclipse.

An alternative classical approach for eclipse prediction involves direct limb-based analysis [38]. This method considers the apparent limbs of both the Sun and the eclipsing body as viewed from a specific point on the shadowed body's surface. Based on the intersection of these limbs, three scenarios can arise:

- If the limbs do not intersect, the point is illuminated.
- If the limbs partially intersect, the point is in the penumbra.
- If the Sun's limb is entirely contained within the limb of the eclipsing body, the point is in the umbra.

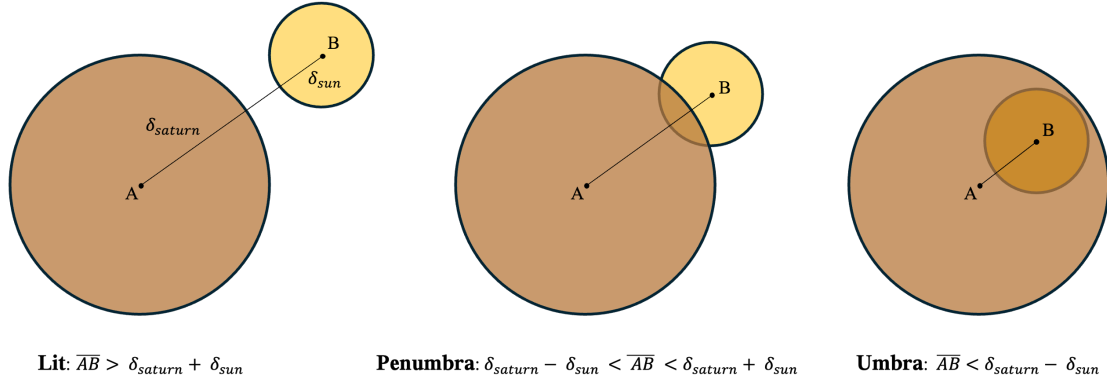


Figure 2.11: Lit, Umbra and penumbra for an observer on Enceladus. Sizes and proportions are not to scale.

While the Besselian method is highly refined and computationally efficient for the Earth-Moon system with its nearly circular shadow, the limb-based approach offers greater geometric flexibility that could be beneficial when dealing with significantly oblate eclipsing bodies, like Saturn.

### 2.2.2 Saturn eclipse formula

In the Saturn–Enceladus system, Saturn's pronounced oblateness, the greatest among the major bodies in the Solar System [39], results in a projected contour that is elliptical rather than circular. This geometric complexity significantly affects the shape and extent of the eclipse shadow cast on Enceladus.

Although oblate eclipse models have been developed for spacecraft applications [40], analogous models tailored for surface-based groundtrack illumination are not available in the literature. As a result, a dedicated formulation is required for this context.

While the conceptual framework illustrated in Fig. 2.11 remains valid, the mathematical treatment is more involved: Saturn must be modelled as a three-dimensional ellipsoid rather than a two-dimensional circle. This is particularly important because Saturn subtends a large angular size as seen from Enceladus, approximately sixty times that of the Moon as seen from Earth (as calculated in Stellarium [35]), so it cannot be approximated as a simple two-dimensional ellipse. Instead, the problem requires considering the intersection of a spheroid with a cone, as depicted in Fig. 2.12.

The only simplification compared to the Earth–Moon configuration is that the penumbral region is almost negligible, owing to the fact that Saturn and Enceladus are approximately ten times farther from the Sun (see equation 2.1).

A complete derivation of Saturn angular size formula is provided in Appendix B. The principal steps are as follows:

1. Saturn is modelled as an oblate spheroid.
2. The contour is determined by imposing the tangency condition between the observer’s line of sight from the surface of Enceladus and the Saturnian spheroid; this is achieved by setting the discriminant of the quadratic equation to zero.
3. The resulting contour is expressed in spherical coordinates.

The final expression is:

$$\delta(\beta) = \arctan \left( \frac{R_{eq}R_{pol}}{\sqrt{(d^2 - R_{eq}^2)(R_{pol}^2 \cos^2(\beta) + R_{eq}^2 \sin^2(\beta))}} \right) \quad (2.7)$$

where:

- $\delta$  is the angular size from Saturn centre to its limb with  $\beta$  direction.
- $\beta$  is the Sun elevation angle as seen from the observer’s location.
- $d$  is the distance from the observer on Enceladus to the centre of Saturn.
- $R_{eq}$  is the equatorial radius of Saturn.
- $R_{pol}$  is the polar radius of Saturn.

Given that flybys on Enceladus are brief (approximately 10 minutes), the angle  $\beta$  is computed once per groundtrack at the time of pericentre.

The distance  $d$  is taken as the average value over the Saturn-facing hemisphere of Enceladus. By evaluating the double integral over this surface, the following expression is obtained:

$$d_{\text{avg}} = \frac{(D^2 + R^2)^{3/2} - (D - R)^3}{3DR} \quad (2.8)$$

where:

- $D$  denotes the distance from the centre of Enceladus to the centre of Saturn.
- $R$  is the mean volumetric radius of Enceladus.

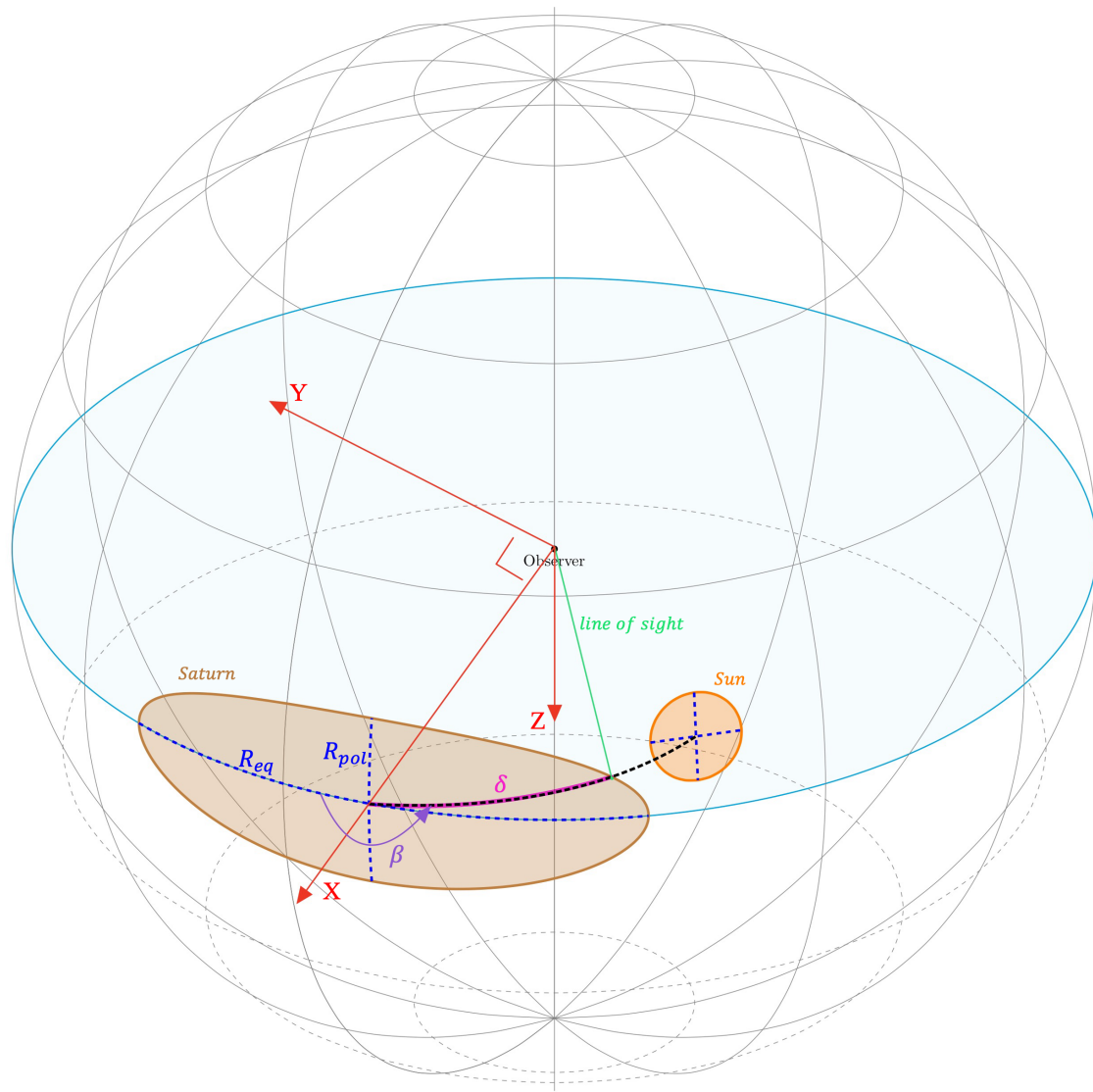


Figure 2.12: Schematic representation of the reference frame with Saturn, its radii, and angles. Sizes and proportions are not to scale.

### 2.2.3 Saturn eclipse results and verifications

With the methodology now fully defined, it is possible to compute the umbral, and penumbral shadow cast by Saturn on Enceladus' surface for any given epoch and overlay it on top of the terminator shadow.

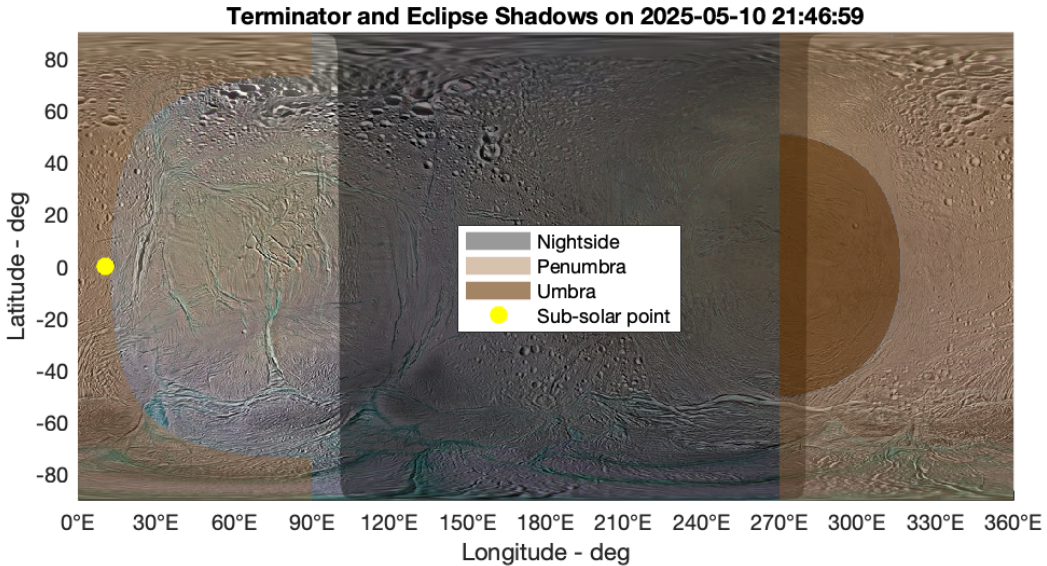


Figure 2.13: Illumination map on Enceladus at the start of the Eclipse during Saturn equinox

To validate the script, a benchmark test was conducted to determine the epoch at which Saturn's penumbra first contacts the surface of Enceladus.

As an initial estimate, Stellarium was used with the observer at latitude  $0^\circ$ , longitude  $0^\circ$  on Enceladus. At approximately 10/05/2025 21:45:23 UTC, the solar limb was observed to begin intersecting Saturn's limb, indicating the onset of the penumbra (see Figure 2.14).

Subsequently, the SPICE routine `gfoclt_c` [41] was employed to obtain a higher-fidelity estimate, modelling both Saturn and the Sun as ellipsoids. This yielded a similar date, but at 21:46:55. It should be noted that `gfoclt_c` computes occultation at the centre of Enceladus and does not allow for an observer on the surface. As a workaround, a custom SPICE kernel was generated, simulating a body of infinitesimal radius located at latitude  $0^\circ$ , longitude  $0^\circ$ , at a distance of 252 km from Enceladus' centre. In this case, the result was 21:46:51.

The script developed for this thesis was then used to determine the time at which the penumbra first reaches Enceladus. The initial result was 21:48:02 UTC, corresponding to an error of just over one minute, which is acceptable but not optimal for this analysis.

Further investigation revealed that SPICE uses Ephemeris Time (ET), a uniform, continuous timescale for celestial mechanics, whereas UTC is the civil time standard, periodically

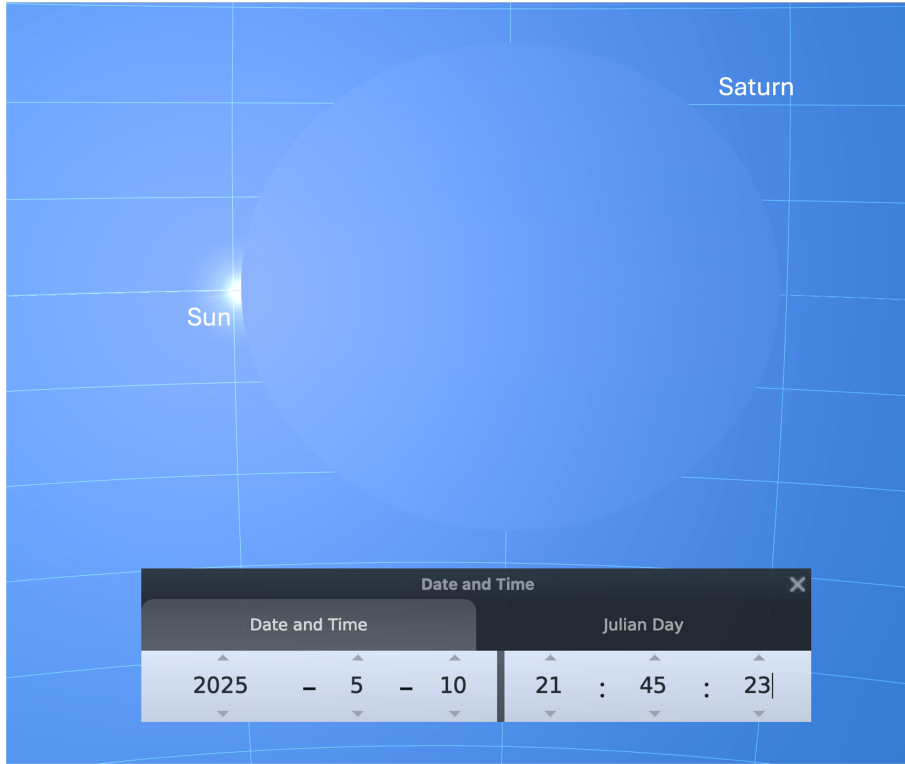


Figure 2.14: Saturn eclipse onset as seen from Enceladus at 10/05/2025 21:45:23 UTC (Stellarium screenshot).

adjusted by leap seconds to account for variations in Earth's rotation.

According to SPICE documentation [42] and time kernels, these two time systems differ by approximately 69 seconds, due to two main components:

1. The atomic offset (DELTA\_T\_A): a constant difference of 32.184 seconds between Terrestrial Time (TT) and International Atomic Time (TAI).
2. Cumulative leap seconds (DELTA\_AT): as of January 2017, 37 leap seconds have been added to UTC.

The sum of these offsets (32.184 s + 37 s) yields a total difference of 69.184 seconds. By applying this correction to the UTC time, the error was reduced to 1 second, yielding a result of 21:46:52, which is considered satisfactory.

A summary of the results is presented in Table 2.1.

A subsequent verification was conducted by evaluating the eclipse onset time over a period of  $\pm 3$  years around the equinox. In all cases, the discrepancy remained below 2 seconds.

The effect of light-time travel was also assessed using the *ABCORR* option in SPICE; however, the resulting difference was negligible, on the order of a few milliseconds, and was therefore omitted from the final implementation.

Table 2.1: Comparison of Methods for Determining Penumbra Contact Time on Enceladus

<b>Method</b>	<b>Timestamp</b>	<b>Error from Reference (s)</b>
Stellarium (Surface Observer) UTC	21:45:23	-88
SPICE gfoclt_c (Centre of Enceladus) ET	21:46:55	+4
SPICE gfoclt_c (Surface Observer) ET	21:46:51	0
Thesis Script UTC	21:48:02	+71
Thesis Script (ET Corrected)	21:46:52	+1

A potential systematic source of error not addressed in this analysis is the influence of Saturn's atmosphere, which may refract light rays. This effect is not considered in the present study.

## 2.3 Other moon eclipses

In this section, an analysis is conducted to determine if eclipses from other Saturn moons on Enceladus were frequent or long-lasting enough to warrant a dedicated implementation. The findings indicate that such events are brief and infrequent, justifying the decision to concentrate efforts on the Saturn-Enceladus system described in Section 2.2.

The following simplifying assumptions were made for this estimation:

- All moons are assumed to follow circular orbits. This is justified by their small eccentricities [20].
- All orbits are assumed to be coplanar within Saturn’s equatorial plane. This is a reasonable approximation [20]; any deviations would primarily affect the timing of eclipse seasons rather than their frequency or duration.
- The moons are modelled as spheres, neglecting oblateness and angular size effects. This is valid given the small apparent sizes of the moons as seen from Enceladus.

If the orbits of Enceladus and another moon are not exactly coplanar, the primary effect is a small temporal shift of the eclipse season. An eclipse season is the period when the Sun is sufficiently close to the moons’ orbital planes to allow for eclipses to occur. For this analysis, it is assumed that these seasons are centred on Saturn’s equinoxes.

To quantify the infrequency and brevity of these events, a detailed methodology was employed. This involved calculating the size of the umbral shadow cast by each moon at the distance of Enceladus, the maximum duration of a potential eclipse, the window of opportunity for such events, and their theoretical frequency.

### 2.3.1 Mathematical Framework

#### 2.3.1.1 Umbra Height

The height of the umbra ( $h_u$ ) cast by an eclipsing moon is determined using algorithm 34 by Vallado [26]: Firstly the umbral cone angle is calculated with equation 2.1 and the umbra height is given by:

$$h_u = \left( \frac{R_b}{\sin(\alpha_u)} - d_{me} \right) \tan(\alpha_u) \quad (2.9)$$

where:

- $R_b$  is the radius of the eclipsing body (moon).
- $\alpha_u$  is the angle of the umbral cone.
- $d_{me}$  is the distance between the eclipsing body and Enceladus.

### 2.3.1.2 Eclipse Duration

The maximum duration of an eclipse ( $t_d$ ) occurs when Enceladus passes through the centre of the moon's umbra. This duration is a function of the umbra's diameter ( $2h_u$ ) and the relative orbital velocity ( $v_{rel}$ ) between Enceladus and the eclipsing moon. For circular, coplanar orbits, the relative velocity is:

$$v_{rel} = |v_e - v_m| = \left| \sqrt{\frac{\mu_{sat}}{a_e}} - \sqrt{\frac{\mu_{sat}}{a_m}} \right| \quad (2.10)$$

where:

- $v_{rel}$  is the relative velocity between Enceladus and the eclipsing moon.
- $v_e$  is the orbital velocity of Enceladus.
- $v_m$  is the orbital velocity of the eclipsing moon.
- $\mu_{sat}$  is the gravitational parameter of Saturn.
- $a_e$  is the semi-major axis of Enceladus's orbit.
- $a_m$  is the semi-major axis of the eclipsing moon's orbit.

The maximum duration is subsequently calculated as:

$$t_d = \frac{2 \cdot h_u}{v_{rel}} \quad (2.11)$$

### 2.3.1.3 Eclipse Season Window

Eclipses of this nature are only possible when the Sun is near Saturn's equatorial plane, which occurs around its equinoxes. Saturn's axial tilt ( $\beta \approx 26.73^\circ$ ) and its orbital period ( $T_{sat}$ ) determine the rate of change of the Sun's declination relative to Saturn's equator. The angular rate of change of the ring plane inclination ( $\dot{\theta}$ ) is maximal at the equinoxes:

$$\dot{\theta} = \frac{360^\circ}{T_{sat}} \sin(\beta) \quad (2.12)$$

For an eclipse to occur, the vertical separation between the centre of the eclipsing moon's umbra and the centre of Enceladus must be less than the sum of Enceladus's radius ( $R_e$ ) and the umbra height ( $h_u$ ). This defines a critical angle ( $\theta_{crit}$ ):

$$\theta_{crit} = \arctan \left( \frac{R_e + h_u}{d_{me}} \right) \quad (2.13)$$

The eclipse season window ( $W_s$ ) is the time it takes for the Sun's declination to sweep through twice this critical angle:

$$W_s = \frac{2 \cdot \theta_{crit}}{\dot{\theta}} \quad (2.14)$$

### 2.3.1.4 Eclipse Opportunities

The frequency of potential eclipses depends on how often Enceladus and the other moon align with Saturn (a conjunction). This is determined by their synodic period ( $T_{syn}$ ) divided by two, calculated from their individual orbital periods ( $T_e$  and  $T_m$ ):

$$T_{conj} = \frac{1}{2} \cdot T_{syn} = \frac{1}{2} \cdot \frac{1}{\left| \frac{1}{T_e} - \frac{1}{T_m} \right|} \quad (2.15)$$

The maximum theoretical number of eclipse opportunities ( $N_{opp}$ ) during a single eclipse season is the duration of the eclipse window divided by the time between conjunctions  $T_{conj}$ . As an eclipse can only occur at conjunction, this provides an estimate of the number of favourable alignments within the window.

$$N_{opp} = \frac{W_s}{T_{conj}} \quad (2.16)$$

## 2.3.2 Results

The calculations for the umbral height cast by Saturn's major inner moons at Enceladus's orbit are presented in Table 2.2. The umbra height is also normalised by the radius of Enceladus (252.1 km) to provide a relative sense of scale.

Table 2.2: Calculated umbra properties for eclipses on Enceladus by other moons.

Moon	Umbra Height (km)	Umbra Height (Normalised)
Mimas	172.7	0.685
Tethys	503.5	1.997
Dione	493.5	1.958
Rhea	623.1	2.472
Titan	2097.1	8.319

The analysis reveals that Mimas is the only moon in this set that casts an umbra smaller than Enceladus itself. The other moons produce umbras that are between two and eight times the radius of Enceladus.

Table 2.3 summarises the key temporal characteristics of these potential eclipses. It shows that the maximum duration for any of these events is short, with the longest being approximately 13 minutes for an eclipse by Tethys. The number of potential opportunities for an

eclipse during each season, which occurs approximately every 14.8 Earth years, is also low.

Table 2.3: Estimated characteristics of moon-on-Enceladus eclipses per season.

Moon	Max. Duration (min)	Window (days)	Opportunities
Mimas	3.4	61.8	~20.4
Tethys	13.1	101.7	~20.3
Dione	6.3	40.8	~14.9
Rhea	5.0	23.1	~11.7
Titan	9.9	18.2	~12.1

These results represent upper-bound estimates, as they do not account for the requirement that the Sun must be precisely aligned for an eclipse to occur during a conjunction between Enceladus and the Saturn moons. Furthermore, the calculated durations correspond to idealised, central alignments; even minor orbital inclinations would significantly reduce eclipse durations. Consequently, eclipses of Enceladus by other moons, though geometrically possible, are extremely brief and infrequent. Given their negligible scientific impact relative to Saturn-induced eclipses, further modelling was not undertaken.

Inclusion of these events in future work would be comparatively easier than a Saturn eclipse, as the moons can be modelled as small spheres, locally approximated as planar on the celestial sphere (thus avoiding the need for spheroidal equations and spherical coordinates). A practical approach would involve iterating with SPICE routines (such as `gfoclt_c` [41]) to generate a table of potential eclipse events and their epochs. These results could then be mapped from the centre of Enceladus to its surface and incorporated into the main script as hard-coded values, thereby avoiding any significant computational overhead.

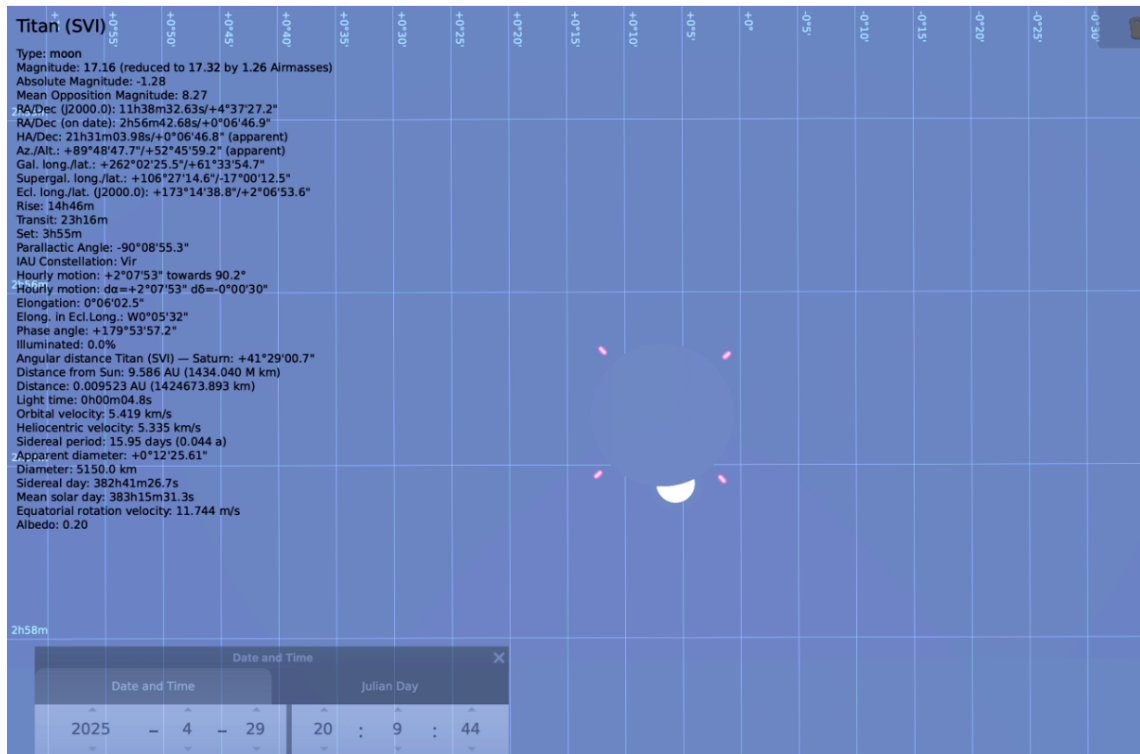


Figure 2.15: Example of a brief rare Titan-induced eclipse on Enceladus, as observed from the surface of the icy moon. Image generated using Stellarium [35].

## 2.4 Illumination final results

This section outlines the integration of the terminator (Section 2.1) and eclipse (Section 2.2) algorithms to produce an efficient script for plotting surface illumination along a groundtrack. Final plots with various configuration options are subsequently presented.

### 2.4.1 Filtering out eclipses

As eclipse computation is computationally intensive, particularly when generating illumination maps for the entire Mercator projection of Enceladus, two filters have been implemented to improve script efficiency:

1. A date filter, using a qualitative range calculated in Stellarium, which has been proven in the subsection 2.2.3 to be a reliable tool for this kind of analysis. A filter of  $\pm 3$  years around the closest equinox has been estimated.
2. A phasing angle filter, see figure 2.16, of  $15^\circ$  between Saturn and Enceladus.

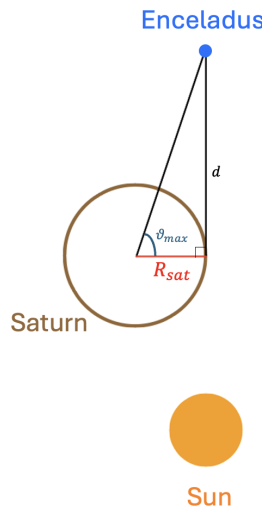


Figure 2.16: Max phasing angle  $\theta_{max}$  to have an eclipse on Enceladus

The derivation of the phasing angle  $\theta_{max}$  is clear from figure 2.16 and is given by:

$$\theta_{max} = \arcsin\left(\frac{R_{Sat}}{d}\right) \approx 15^\circ \quad (2.17)$$

where:

- $R_{Sat}$  is the equatorial radius of Saturn.
- $d$  is the mean distance from Enceladus to Saturn.

It should be noted that the phasing angle threshold adopted here corresponds to the worst-case scenario at the day of equinox, using Saturn's equatorial radius. While a more precise, date-dependent threshold could be computed dynamically, a simpler fixed value has been preferred for this analysis.

The complete filtering algorithm is presented below:

---

**Algorithm 1** Eclipse Filtering Algorithm
 

---

**Require:** Epoch of the flyby pericentre,  $t_{epoch}$  (in Ephemeral Time)

**Ensure:** Boolean: true if an eclipse is possible and should be computed

```

1:  $t_{equinox} \leftarrow$  Compute time of the closest Saturnian equinox to  $t_{epoch}$ 
2:  $year_{equinox} \leftarrow$  Extract year from  $t_{equinox}$ 
3:  $year_{epoch} \leftarrow$  Extract year from  $t_{epoch}$ 
4: if  $|year_{epoch} - year_{equinox}| > 3$  then
5:   return false
6: else
7:    $\theta \leftarrow$  Compute phasing angle between Saturn and Enceladus at  $t_{epoch}$ 
8:   if  $\theta > 15^\circ$  then
9:     return false
10:  else
11:    return true
12:  end if
13: end if
```

---

### 2.4.2 Final illumination plots

The final illumination plotting script integrates the terminator and eclipse algorithms, incorporating the filtering mechanism described in subsection 2.4.1. The script is designed to be flexible, allowing users to select various configuration options for the illumination maps. These options include:

- Decide whether to plot the illumination on the groundtrack colour or to plot the illumination on the whole Enceladus surface.
- Ability to specify the desired sun incidence angles ranges, which is a common important parameter for orbit mapping.

For the first option, plotting coloured groundtracks is recommended, as illumination is computed at each groundtrack point. Given that the flyby is nearly linear (high eccentricity) and brief in duration (approximately 10 minutes), a linear, constant-velocity time distribution is assumed. This approach is computationally efficient and facilitates the visualisation of multiple flybys. For visualisation or debugging of a single flyby, illumination may instead be plotted over the entire Enceladus surface, providing a more direct representation of conditions at pericentre.

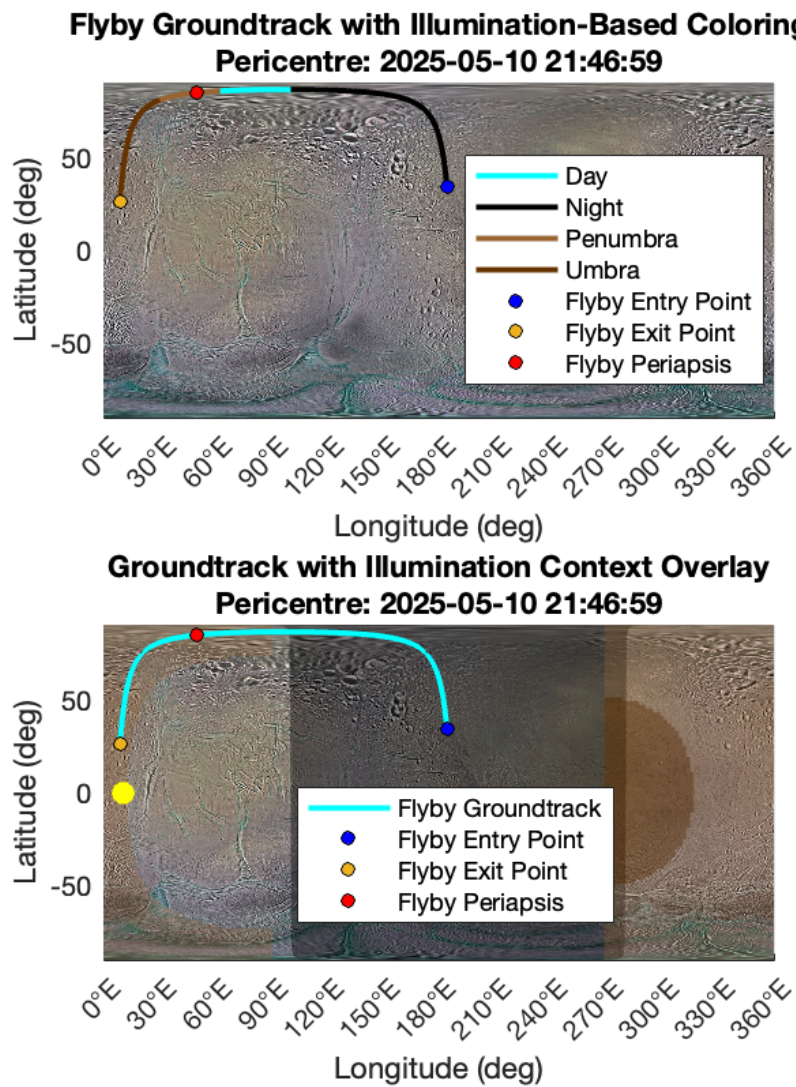


Figure 2.17: Plots of a flyby during the start of an eclipse. The first plot is the illumination on the groundtrack, the second is the illumination on the whole Enceladus surface.

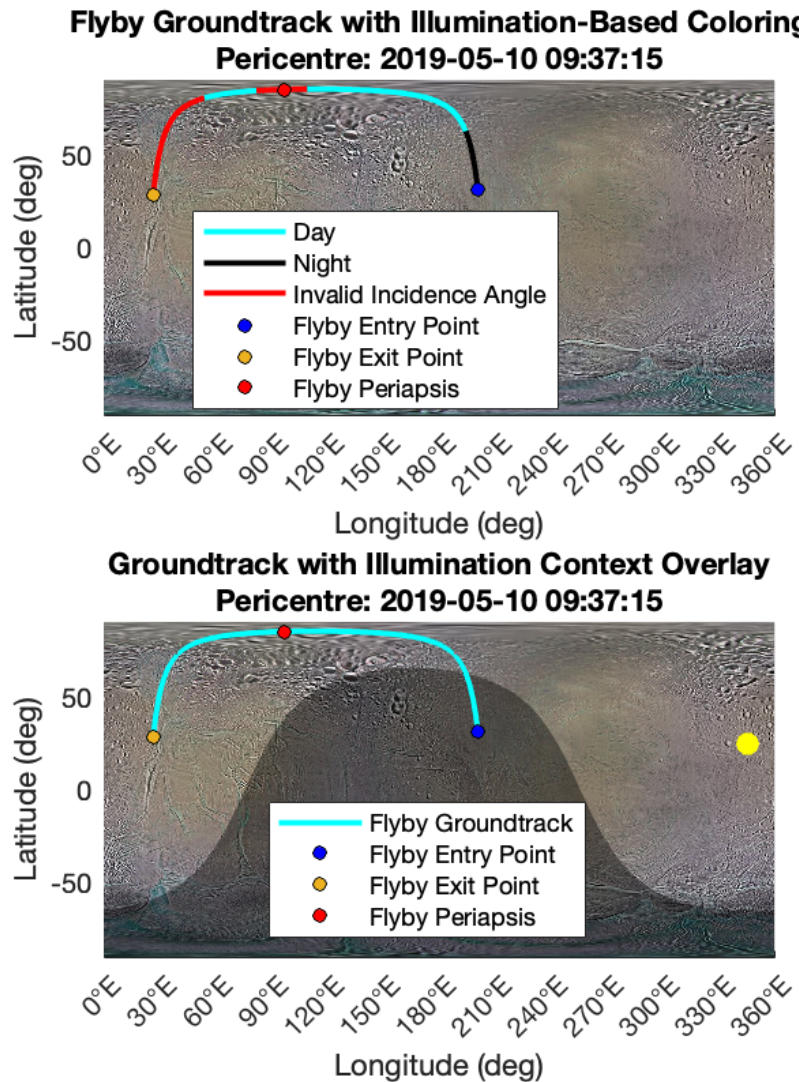


Figure 2.18: Plots of the flyby with selected Sun incidence angles. The first plot is the illumination on the groundtrack, the second is the illumination on the whole Enceladus surface.

# Chapter 3

## N-body dynamics

The design of complex Multiple Gravity Assist (MGA) trajectories for Enceladus missions is a central focus of the GIGANTES framework. This problem can be regarded as a specific case of the multi-target mission scenario, closely related to the Travelling Salesman Problem (TSP) in astrodynamics[15], where each node corresponds to a sequential Enceladus flyby. The associated optimisation is formulated as a mixed-integer nonlinear programming (MINLP) problem[16], requiring the selection of an optimal sequence of flyby parameters and the computation of the corresponding orbital transfers. Due to the combinatorial complexity, exhaustive high-fidelity analysis is computationally prohibitive. To address this, GIGANTES employs the linked conics model[17], a limiting case of the patched conic approximation in which the sphere of influence is reduced to a point (zero sphere of influence, ZSOI)[18]. This approach, justified by the dominance of Saturn's mass, treats each flyby as an instantaneous change in the spacecraft's velocity vector ( $v_\infty$ ) at the moon's location, thereby enabling rapid exploration of feasible trajectory families.

Nevertheless, when transferring solutions from this simplified two-body framework to a high-fidelity n-body environment, such as ESA GODOT[19], significant discrepancies may arise. In fact, in the context of GIGANTES development, it has been observed that trajectories that are feasible and well-targeted in the linked conics model can become unviable in the n-body context: the actual groundtrack of the flyby may diverge from the two-body prediction, potentially failing to satisfy scientific constraints or resulting in a missed encounter with Enceladus due to its small size. To address these challenges, the GIGANTES Toolbox functions were first updated to employ NASA SPICE[43] full n-body ephemerides in place of the simplified circular and coplanar orbits. This modification enables a more accurate initial trajectory estimate.

The research, subsequently, has been structured into the following phases:

1. **Section 1:** The analytical linked conics model and associated flyby geometry are defined. This model, based on the zero sphere of influence (ZSOI) assumption, treats each flyby as an instantaneous velocity change. To ensure physical consistency, the idealised event is converted into a hyperbolic trajectory, enabling determination of the periapsis state. For targeting, a pump and crank angle parameterisation is used, with transformations to the Saturn-centric frame 2.1.2.
2. **Section 2:** A high-fidelity  $n$ -body propagator is developed using Cowell's formulation, incorporating perturbations from major bodies and Saturn's  $J_2$  zonal harmonic. Analysis identifies the Sun, Saturn's  $J_2$ , and Titan as the principal perturbers, together accounting for over 99.9% of total perturbations.
3. **Section 3:** Local comparison of the linked conics and  $n$ -body models is performed by propagating both from the same periapsis state over a ten-minute interval. Despite a maximum Cartesian deviation of 19 km, the groundtrack shape and location remain qualitatively unchanged, confirming the suitability of the simplified model as an initial guess.
4. **Section 4:** An iterative differential correction scheme is implemented, employing B-plane targeting and the State Transition Matrix (STM). The STM maps initial velocity changes to B-plane coordinates, and a pseudo-inverse method yields the minimum velocity correction (TCM) required to match the target flyby in the  $n$ -body environment.

## 3.1 Multiple Gravity Assist Modelling

This section describes the simplified modelling framework employed by GIGANTES for exploring the MGA search space, focusing on the linked-conics approximation<sup>3.1.1</sup> and its associated three-dimensional flyby geometry parameterisation<sup>3.1.2</sup>.

### 3.1.1 Linked-Conics Approximation

The GIGANTES Toolbox utilises a linked conics model to determine optimal solutions in the MGA search space. This method is commonly used in the literature[18][44][45][16][46] for the preliminary design of MGA missions[17].

The linked conics model is a limiting case of the two-body (Saturn and spacecraft) patched conic approximation. Here, the sphere of influence (SOI) of gravity-assist bodies is reduced to a point, also known as the zero sphere of influence (ZSOI)[18]. This approximation is valid when the mass of the primary body is several orders of magnitude greater than that of the secondary bodies, as in the case of moon flybys around Saturn. As a result, the entry point into the SOI of the gravity-assist body is undefined, and an encounter is assumed whenever the spacecraft's position coincides with that of the target body. The flyby is modelled as an instantaneous change in  $v_\infty$ .

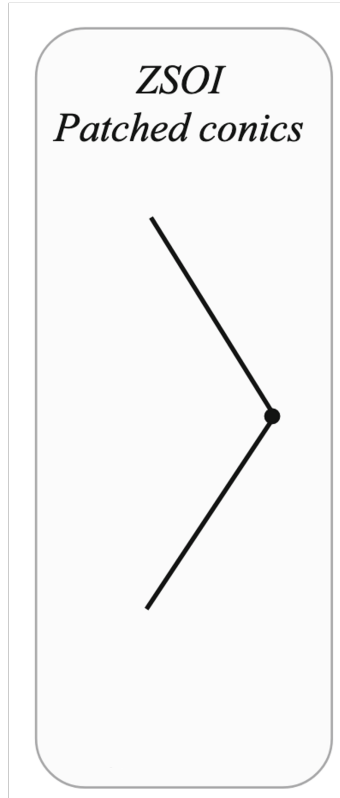


Figure 3.1: Linked conics flyby representation (adapted from[18])

A purely linked-conics representation of the flyby does not allow for a realistic groundtrack to be plotted. Therefore, the GIGANTES Toolbox implements a method to convert the linked-conics flyby into a physically consistent hyperbolic trajectory within the sphere of influence of the flyby body, following the procedure described by Bradley et al.[18] and Bellome et al.[16], as detailed below.

First, the maximum bending angle  $\delta_{\max}$  is determined from the minimum flyby altitude  $h_{\min}$  (e.g., 10km for Enceladus, 200km for Titan) to assess the feasibility of the requested flyby geometry:

1. The minimum pericentre radius  $r_{p,\min}$  is calculated using the flyby moon radius  $R_{\text{moon}}$  and the minimum flyby altitude :

$$r_{p,\min} = R_{\text{moon}} + h_{\min} \quad (3.1)$$

2. The minimum eccentricity of the hyperbolic trajectory is then

$$e_{\min} = 1 + \frac{r_{p,\min} v_{\infty}^2}{\mu_{\text{moon}}} \quad (3.2)$$

3. The maximum turning angle,  $\delta_{\max}$ , is given by

$$\delta_{\max} = 2 \arcsin \left( \frac{1}{e_{\min}} \right) \quad (3.3)$$

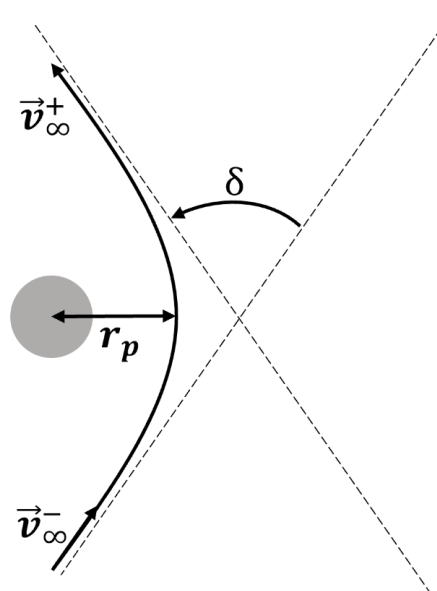


Figure 3.2: Hyperbolic flyby geometry[16]

Once  $\delta_{\max}$  is known, the actual turning angle  $\delta$  of the flyby is computed from the incoming and outgoing hyperbolic excess velocity vectors,  $\vec{v}_\infty^-$  and  $\vec{v}_\infty^+$ , as follows:

$$\delta = \arccos \left( \frac{\vec{v}_\infty^- \cdot \vec{v}_\infty^+}{|\vec{v}_\infty^-| |\vec{v}_\infty^+|} \right) \quad (3.4)$$

If  $\delta < \delta_{\max}$ , the flyby is feasible and no correction is required. If  $\delta > \delta_{\max}$ , the flyby is not possible and the outgoing velocity vector must be adjusted as follows:

1. Set  $\delta = \delta_{\max}$ .
2. The Saturn-centric reference frame 2.1.2 is not ideal for this scenario, a reference frame aligned with the incoming hyperbolic excess velocity is defined:

$$\begin{aligned} \hat{\mathbf{b}}_1 &= \frac{\vec{v}_\infty^-}{|\vec{v}_\infty^-|} \\ \hat{\mathbf{b}}_2 &= \frac{\hat{\mathbf{b}}_1 \times \vec{r}_{\text{moon}}}{|\hat{\mathbf{b}}_1 \times \vec{r}_{\text{moon}}|} \\ \hat{\mathbf{b}}_3 &= \hat{\mathbf{b}}_1 \times \hat{\mathbf{b}}_2 \end{aligned} \quad (3.5)$$

where  $\vec{r}_{\text{moon}}$  is the Saturn-centric position vector of the moon at the time of the flyby.

3. Rewrite the outgoing hyperbolic excess velocity in the new reference frame:

$$\vec{v}_{\infty, \text{transf}}^+ = \frac{1}{|\vec{v}_\infty^-|} B^T (\vec{v}_\infty^+)^T \quad (3.6)$$

where  $B$  is the rotation matrix between the two reference frames:

$$B = [\hat{\mathbf{b}}_1 \quad \hat{\mathbf{b}}_2 \quad \hat{\mathbf{b}}_3] \quad (3.7)$$

4. From this define  $\zeta$ , the angle between  $\hat{\mathbf{b}}_3$  and the projection of  $\vec{v}_\infty^+$  onto the  $\hat{\mathbf{b}}_2$ - $\hat{\mathbf{b}}_3$  plane:

$$\zeta = \arctan \left( \frac{\vec{v}_{\infty, \text{transf}}^+ \cdot \hat{\mathbf{b}}_3}{\vec{v}_{\infty, \text{transf}}^+ \cdot \hat{\mathbf{b}}_2} \right) \quad (3.8)$$

5. Project the outgoing hyperbolic excess velocity onto the plane defined by  $\delta$  and  $\zeta$ :

$$\vec{v}_\infty^+ = v_\infty (\cos \delta \hat{\mathbf{b}}_1 + \sin \delta [\sin \zeta \hat{\mathbf{b}}_2 + \cos \zeta \hat{\mathbf{b}}_3]) \quad (3.9)$$

Now that the outgoing hyperbolic excess velocity vector is corrected, the pericentre state can be fully described following Bradley procedure[18]:

1. Find the unit direction of the periapsis position

$$\hat{r}_p = \frac{\vec{v}_\infty^- - \vec{v}_\infty^+}{|\vec{v}_\infty^- - \vec{v}_\infty^+|} \quad (3.10)$$

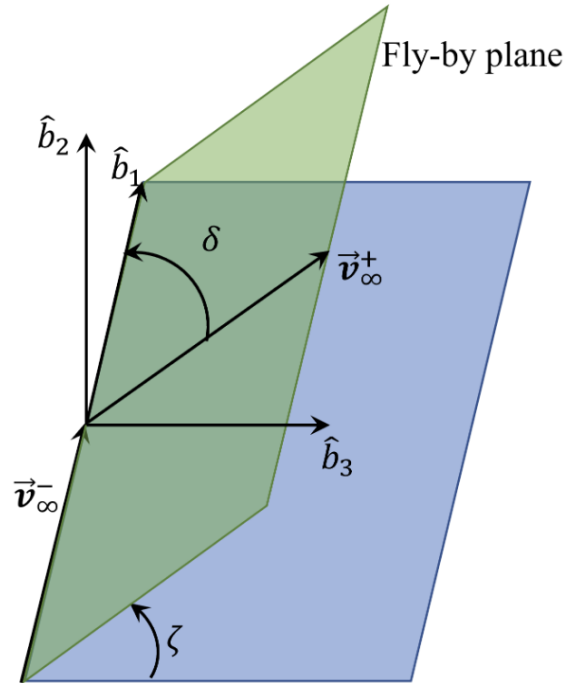


Figure 3.3: Reference frame for the incoming hyperbolic excess velocity, illustrating the turning angle  $\delta$  and the angle  $\zeta$ [16]

2. Calculate the direction of the angular momentum vector

$$\hat{h} = \frac{\vec{v}_{\infty}^{-} \times \vec{v}_{\infty}^{+}}{|\vec{v}_{\infty}^{-} \times \vec{v}_{\infty}^{+}|} \quad (3.11)$$

3. Determine the unit direction of the periapsis velocity

$$\hat{v}_p = \hat{h} \times \hat{r}_p \quad (3.12)$$

4. Find the magnitude of the periapsis position and velocity

$$r_p = \frac{\mu(e-1)}{|\vec{v}_{\infty}|^2} \quad v_p = \sqrt{|\vec{v}_{\infty}|^2 + \frac{2\mu}{r_p}} \quad (3.13)$$

5. Combine direction and magnitude to find the full state at periapsis

$$\mathbf{r}_p = r_p \hat{r}_p \quad \mathbf{v}_p = v_p \hat{v}_p \quad (3.14)$$

Finally, once the periapsis state is determined, the spacecraft trajectory within the sphere of influence is propagated using a two-body model with the moon as the central body. This yields a physically consistent flyby that satisfies the geometric and minimum altitude constraints, as illustrated in Figure 3.4, and enables the plotting of realistic groundtracks on the moon.

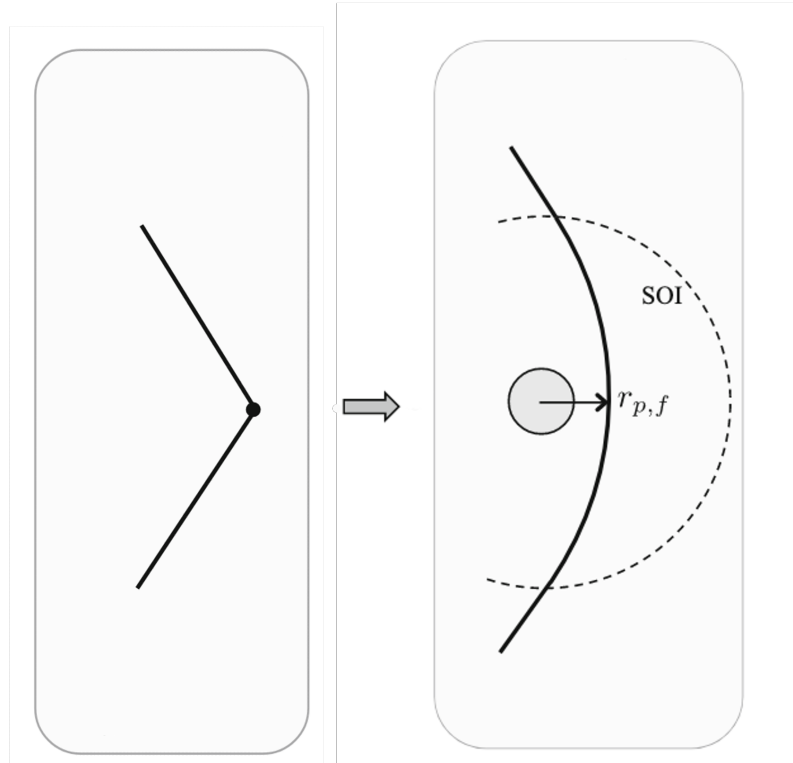


Figure 3.4: Transition from the linked conics approximation to a physically consistent hyperbolic flyby (adapted from [18]).

### 3.1.2 Flyby Geometry

The three-dimensional flyby geometry described in Section 3.1.1 is suitable for determining the periapsis state. For flyby targeting, however, GIGANTES employs an alternative three-dimensional parameterisation, defined by the two nodes representing the states immediately before and after the flyby:

$$\begin{aligned} \text{node}_{\text{in}} &= [v_{\infty}^-, \alpha^-, k^-] \\ \text{node}_{\text{out}} &= [v_{\infty}^+, \alpha^+, k^+] \end{aligned} \quad (3.15)$$

where:

- $v_{\infty}^-$  and  $v_{\infty}^+$  are the magnitudes (in km/s) of the incoming and outgoing hyperbolic excess velocity vectors, respectively;
- $\alpha$  is the pump angle (in radians);
- $\kappa$  is the crank angle (in radians).

A visual representation is provided in Figure 3.5.

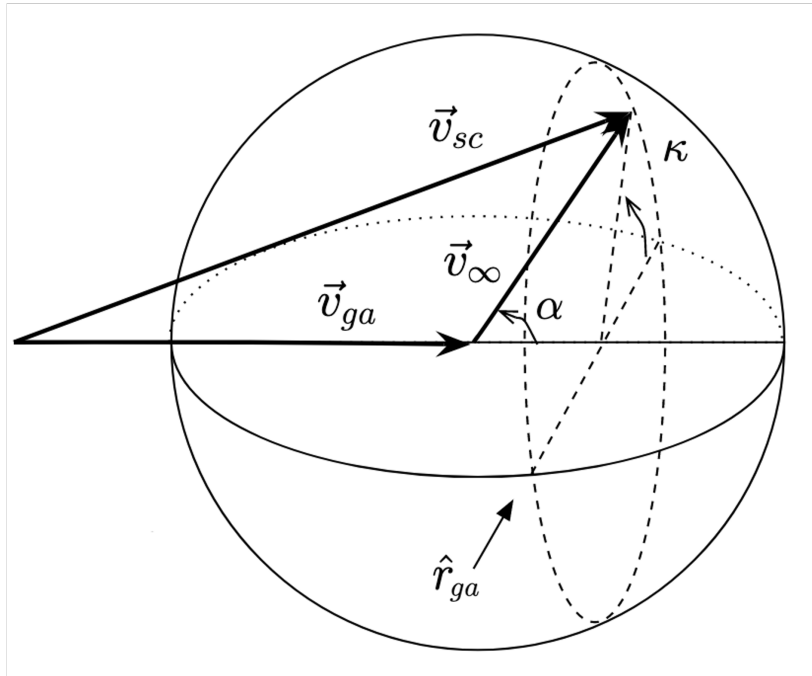


Figure 3.5: Visualisation of the pump ( $\alpha$ ) and crank ( $\kappa$ ) angles for the flyby geometry.  $v_{sc}$  is the velocity of the spacecraft in the Saturn-centric reference frame 2.1.2;  $v_{ga}$  is the velocity of the gravity-assist body (Enceladus) in the same frame;  $v_{\infty}$  is the hyperbolic excess velocity vector;  $r_{ga}$  is the distance from the gravity-assist body (Enceladus) to the central body (Saturn) at the time of the flyby. Adapted from [46].

Once targeting is complete, it is necessary to convert the two  $v_\infty$  vectors to the Saturn-centric inertial reference frame 2.1.2 so that the periapsis state can be determined using the technique defined in Section 3.1.1. The procedure is as follows.

First, a TCN (tangential, cross, normal) reference frame is defined[46]:

$$\begin{aligned}\hat{\mathbf{q}}_3 &= \hat{\mathbf{T}} = \frac{\vec{v}_{\text{ga}}}{|\vec{v}_{\text{ga}}|} \\ \hat{\mathbf{q}}_2 &= \hat{\mathbf{C}} = \frac{\vec{r}_{\text{ga}} \times \vec{v}_{\text{ga}}}{|\vec{r}_{\text{ga}} \times \vec{v}_{\text{ga}}|} \\ \hat{\mathbf{q}}_1 &= \hat{\mathbf{N}} = \hat{\mathbf{T}} \times \hat{\mathbf{C}}\end{aligned}\quad (3.16)$$

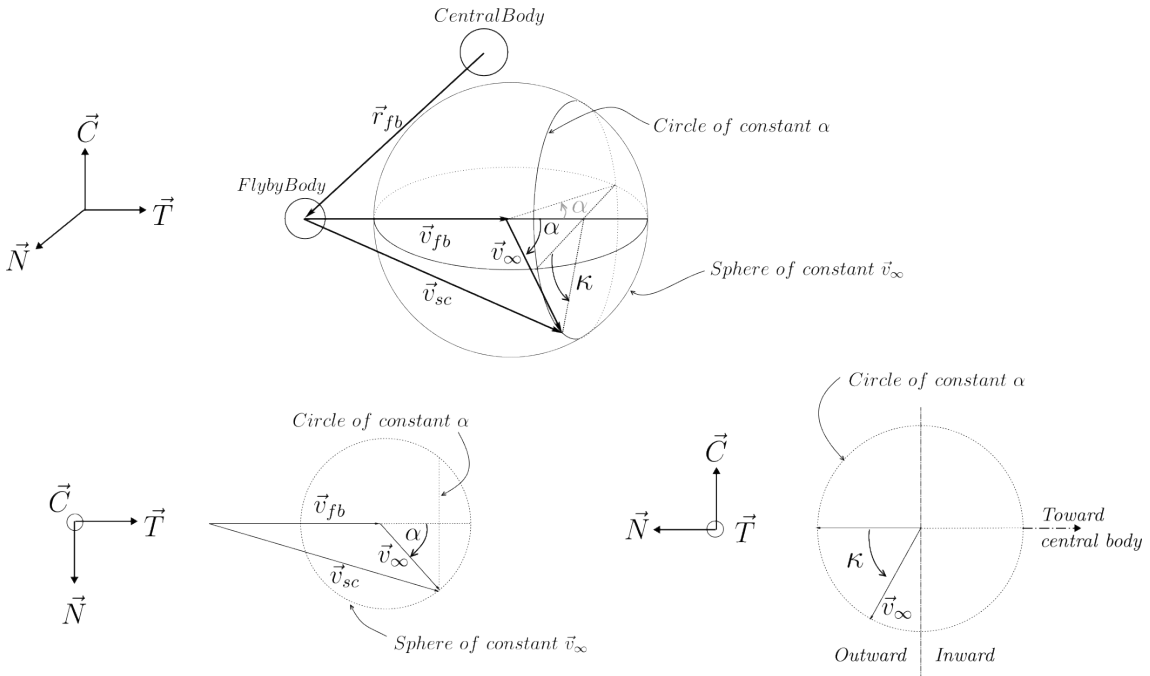


Figure 3.6: TCN reference frame definition (from ESA MIDAS [13])

Using spherical coordinates,  $v_\infty$  can be expressed in TCN as:

$$\vec{v}_{\infty,\text{TCN}} = v_\infty \sin(\alpha) \cos(\kappa) \hat{q}_1 + v_\infty \sin(\alpha) \sin(\kappa) \hat{q}_2 + v_\infty \cos(\alpha) \hat{q}_3 \quad (3.17)$$

Subsequently, the hyperbolic excess velocity in the Saturn-centric inertial frame 2.1.2 is obtained by transforming from the TCN frame:

$$\vec{v}_{\infty,\text{CAR}} = (Q^T \vec{v}_{\infty,\text{TCN}})^T \quad (3.18)$$

where  $Q$  is the rotation matrix whose columns are the unit vectors  $\hat{q}_1$ ,  $\hat{q}_2$ , and  $\hat{q}_3$ :

$$\mathcal{Q} = [\hat{q}_1 \quad \hat{q}_2 \quad \hat{q}_3] \quad (3.19)$$

The computed  $\vec{v}_{\infty, \text{CAR}}$  enables the definition of the spacecraft state at the flyby epoch in Saturn-centric coordinates 2.1.2:

$$\begin{aligned}\vec{r}_{\text{sc}} &= \vec{r}_{\text{ga}} \\ \vec{v}_{\text{sc}} &= \vec{v}_{\text{ga}} + \vec{v}_{\infty, \text{CAR}}\end{aligned}\quad (3.20)$$

This formulation provides the initial conditions for forward and backward propagation of the spacecraft trajectory, yielding a reference linked-conics orbit suitable for comparison with the  $n$ -body solution.

## 3.2 Main Perturbers of the flyby

While the linked-conics model provides computational efficiency for preliminary design, high-fidelity mission analysis requires accurate modelling of Saturn's complex gravitational environment[47]. This section presents the development of an n-body propagator based on Cowell's formulation[26] and identifies the principal perturbing bodies affecting Enceladus flybys.

A key insight in astrodynamics is that typically only three to four dominant perturbing bodies account for the vast majority of the total perturbation from the idealised two-body solution[48]. By systematically ranking the relative influence of potential perturbing bodies, this analysis establishes the minimal set of bodies required for accurate yet computationally efficient trajectory propagation in the Saturnian system.

### 3.2.1 N-body propagator

The two-body orbital motion, governed by Newton's law of universal gravitation, describes the trajectory of a spacecraft of negligible mass under the sole influence of a central body. This admits a closed-form analytical solution, making orbit propagation straightforward and computationally efficient. The equations of motion are:

$$\ddot{\vec{r}} = -\frac{\mu_{CB}}{r^3} \vec{r} \quad (3.21)$$

where  $\vec{r}$  is the position vector of the spacecraft relative to the central body,  $r = |\vec{r}|$ , and  $\mu$  is the standard gravitational parameter of the central body.

When gravitational perturbations from additional bodies are included, the problem becomes more complex and no general analytical solution exists[26]. Numerical methods are therefore employed. The Cowell formulation[26] extends the equations of motion 3.21 to account for perturbing accelerations:

$$\ddot{\vec{r}} = -\frac{\mu_{CB}}{r^3} \vec{r} + \vec{a}_{pert} \quad (3.22)$$

where  $\vec{a}_{pert}$  denotes the cumulative perturbing acceleration from all additional bodies and other effects.

Considering the gravitational influence of  $N$  perturbing bodies and the zonal harmonics of the central body(Saturn),  $\vec{a}_{pert}$  is given by [49]:

$$\vec{a}_{pert} = \vec{a}_{nbody} + \vec{a}_{zonal}$$

$$\vec{a}_{nbody} = -\sum_{i=1}^N \mu_{TB,i} \left( \frac{(\vec{r} - \vec{r}_{TB,i})}{|\vec{r} - \vec{r}_{TB,i}|^3} + \frac{\vec{r}_{TB,i}}{r_{TB,i}^3} \right) \quad (3.23)$$

$$\vec{a}_{zonal} = -\frac{\mu}{r^2} \sum_{n=2}^{N_{max}} J_n \left( \frac{R_{eq}}{r} \right)^n \nabla P_n(\sin \phi)$$

The n-body acceleration  $a_{nbody}$  accounts for the gravitational influence of additional massive bodies (such as the Sun, Jupiter, and Saturn's major moons) and consists of two physically distinct contributions:

### 1. Direct acceleration

$$a_{direct} = -\frac{\mu_{TB,i}}{|\vec{r} - \vec{r}_{TB,i}|^3} (\vec{r} - \vec{r}_{TB,i})$$

This represents the direct gravitational attraction exerted by the  $i$ -th perturbing body on the spacecraft. Here,  $\mu_{TB,i}$  is the standard gravitational parameter of the  $i$ -th third body (e.g., the Sun, a planet, or a moon), and  $\vec{r}_{TB,i}$  is the position vector of the  $i$ -th perturbing body relative to the central body (Saturn).

### 2. Indirect acceleration

$$a_{indirect} = \frac{\mu_{TB,i}}{r_{TB,i}^3} \vec{r}_{TB,i}$$

This term accounts for the fact that the central body (Saturn) is also being accelerated by the perturbing body.

The zonal harmonic acceleration  $a_{zonal}$  captures the effects of Saturn's non-spherical mass distribution. Saturn's rapid rotation causes it to be oblate (flattened at the poles), creating a gravitational field that varies with latitude:

- $J_n$  are the unnormalised zonal harmonic coefficients that quantify the degree of deviation from spherical symmetry
- $R_{eq}$  is Saturn's equatorial radius
- $P_n(\sin \phi)$  are Legendre polynomials where  $\phi$  is the spacecraft's latitude
- The gradient  $\nabla P_n(\sin \phi)$  provides the acceleration components in Cartesian coordinates
- Higher-order terms ( $n > 2$ ) become negligible at large distances but can be significant during close encounters

In this work, the effect of solar radiation pressure (SRP), the force imparted to the spacecraft by the momentum of solar photons, has been neglected in  $a_{pert}$ . In fact The SRP acceleration at Earth's distance from the Sun is given by[50]:

$$P_{srp} = \frac{P_0}{c} \left( \frac{R_0}{R} \right)^2 = 4.57 \times 10^{-6} \left( \frac{R_0}{R} \right)^2 [\text{N/m}^2] \quad (3.24)$$

where  $P_0 = 1367 \text{ W/m}^2$  is the solar flux at 1 AU,  $c = 299,792,458 \text{ m/s}$  is the speed of light,  $R_0$  is the Sun–Earth mean distance (1 AU) and  $R$  is the heliocentric distance of the spacecraft.

But since from eq. 3.24 the solar radiation pressure decreases with the square of the heliocentric distance  $R$ , the SRP at Saturn (at a mean distance of 9.5 AU [28]) is:

$$P_{\text{SRP}, \text{Saturn}} = P_{\text{SRP}, \text{Earth}} \left( \frac{1 \text{ AU}}{9.5 \text{ AU}} \right)^2 = P_{\text{SRP}, \text{Earth}} \times 0.01108 \quad (3.25)$$

This results in an SRP acceleration at Saturn that is approximately two orders of magnitude smaller than at Earth, rendering its effect negligible for the purposes of this study.

Numerical integration of the second-order ordinary differential equation in Equation 3.23 is performed using MATLAB's `ode45` function, which employs a variable-step Runge–Kutta method[51].

### 3.2.2 Identification of Principal Perturbers

The  $n$ -body propagator described in Section 3.2.1 is employed to identify the principal perturbers affecting Enceladus flybys. Determining the dominant perturbing bodies is necessary to characterise the primary dynamical effects and to improve the computational efficiency of  $n$ -body simulations.

The test scenario (see Fig. 3.7) considers a trajectory with a single Enceladus flyby (excluding close approaches to Titan), with parameters( see table 3.1) taken from the GI-GANTES technical report [14].

Table 3.1: Initial and final node parameters for the Enceladus flyby scenario.

	$v_\infty$ [km/s]	Pump angle $\alpha$ [deg]	Crank angle $k$ [deg]
node <sub>in</sub>	4	8.6918	-86.9406
node <sub>out</sub>	4	8.6918	-88.1610

The principal perturbers are identified by computing the Cartesian state from the linked-conics incoming node using Equation 3.20. The semi-major axis is then derived by converting the Cartesian coordinates to Keplerian elements, from which the orbital period is determined.

The state is propagated forward for 1.2 times the orbital period using the  $n$ -body propagator, each time with only one perturber included. The semi-major axis of the perturbed orbit is estimated as:

$$a = \frac{r_p + r_a}{2} \quad (3.26)$$

where  $r_p$  and  $r_a$  are the pericentre and apocentre of the perturbed spacecraft orbit, computed as the minimum and maximum norms of the position vector, respectively.

This analysis is conducted over multiple epochs from 2020 to 2050 (encompassing more than one Saturnian year [20]) to account for epoch-dependent variations. The results,

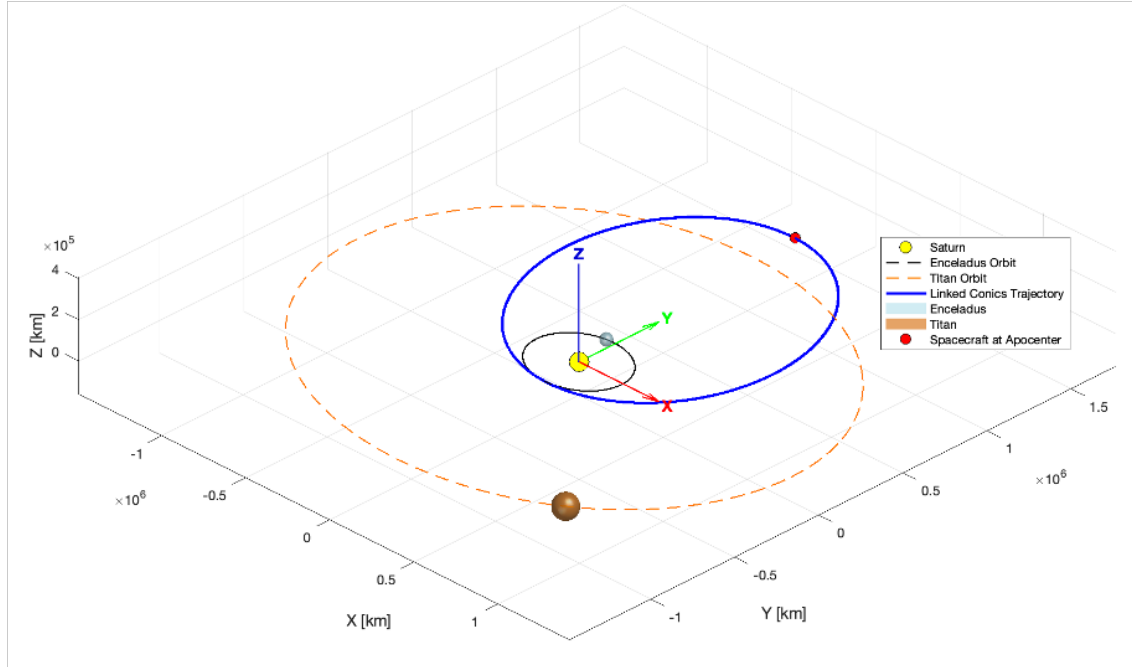


Figure 3.7: Linked-conics reference trajectory for the Enceladus flyby scenario. The positions of Enceladus, Titan, and the spacecraft are shown at the spacecraft apocentre. Celestial body sizes are not to scale.

ranked by the perturbing effect, measured as the difference in kilometres between the linked-conics and perturbed semi-major axis, are presented in Figure 3.2.2.

It is found that, in addition to Saturn and Enceladus, the principal perturbers, accounting for over 99.9% of the total perturbation, are the Sun, Saturn's  $J_2$  zonal harmonic, and Titan. This result is consistent with expectations, as Saturn's oblateness is significant [39], and Titan is the most massive Saturnian moon[20].

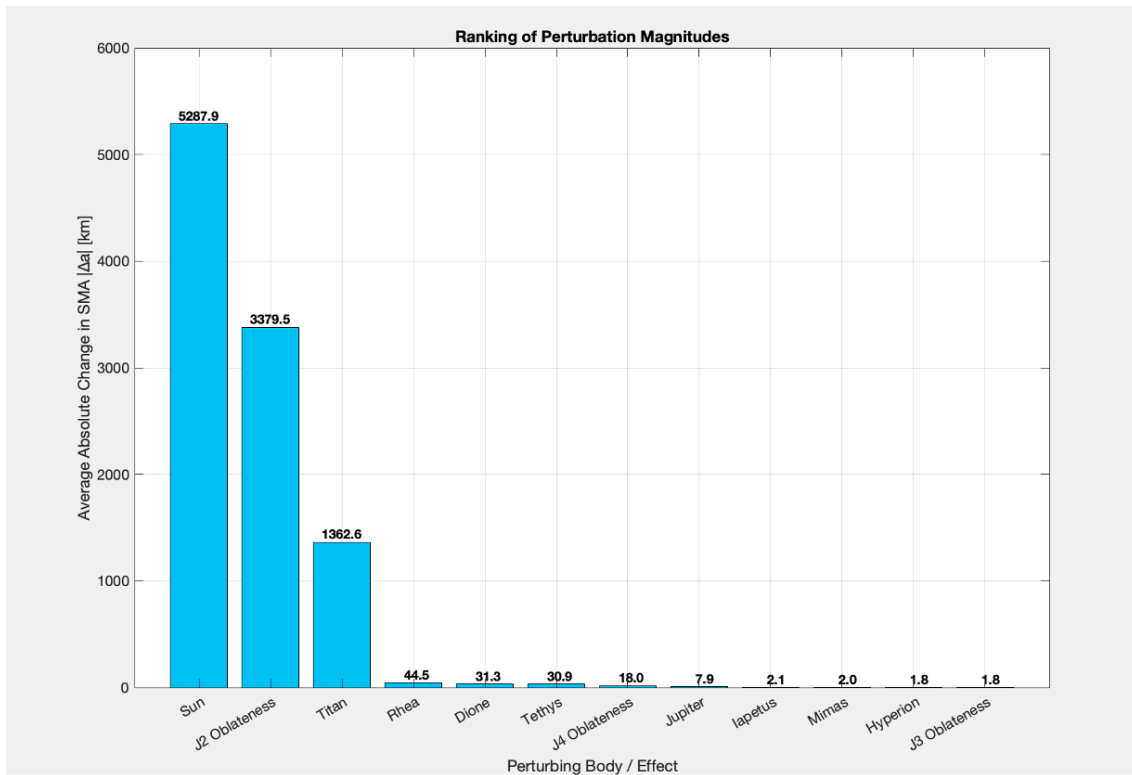


Figure 3.8: Principal perturbers of the Enceladus flyby scenario, excluding Enceladus, ranked by the deviation in semi-major axis from the linked-conics solution. The perturbation, measured in kilometres, is evaluated over multiple epochs from 2020 to 2050.

## 3.3 Local Groundtrack Convergence

### 3.3.1 Existing Literature on Groundtrack Dynamics

Having identified the principal perturbers affecting Enceladus trajectories, the next critical question is how these perturbations affect the actual flyby groundtrack, the spacecraft's path over Enceladus' surface. While the previous sections established that n-body effects cause significant orbital deviations, the specific impact on groundtrack geometry and targeting accuracy requires further investigation. Understanding this impact is crucial for mission planning, as scientific objectives depend heavily on precise ground coverage patterns.

The existing literature on groundtrack dynamics in planetary systems reveals two primary research directions relevant to this challenge. For long-term orbital missions around the moons of Jupiter and Saturn, studies have focused on understanding how n-body perturbations shape groundtrack evolution over extended periods [52], [53]. These investigations have led to the development of specialised orbit designs such as "frozen orbits" that maintain stable groundtrack geometries [54], and "circulating ball-of-yarn orbits" that systematically distribute surface coverage across diverse latitudes [53].

For flyby missions in the Saturnian system, research has concentrated on designing complex "moon tours" that leverage gravity assists to achieve targeted science observations [55], [56]. These studies primarily address the strategic placement of flybys within multi-target sequences, focusing on how third-body perturbations from Saturn influence long-term trajectory evolution and the global distribution of encounter opportunities.

However, both research directions leave a critical gap: the systematic analysis of how n-body perturbations affect the fine-scale geometry and local evolution of individual flyby groundtracks during the actual close approach phase. While the literature addresses either long-term orbital evolution or global tour design, it does not provide sufficient guidance for understanding how the simplified linked-conics approximation used in preliminary design translates to high-fidelity n-body environments during the short but scientifically critical flyby period. This gap motivates the local propagation analysis presented in the following subsection.

### 3.3.2 Local Propagation of Groundtracks

A good starting point for such an investigation could be a local, qualitative propagation to assess the immediate deviations from the simplified model. Before the optimisation described in Section 3.4, a local propagation of the groundtracks was performed to assess the qualitative changes induced by the principal perturbing bodies identified in Section 3.2.2. The methodology follows the procedure outlined in Section 3.2.1 to determine the virtual linked-conics periapsis state (see Equation 3.14). From this state, both the two-body (linked-conics) and  $n$ -body propagators, incorporating  $J_2$ , the Sun, Titan, and Enceladus as the main perturbations, are used to propagate the trajectory forwards and backwards for ten minutes (the Enceladus reference flyby time [14]).

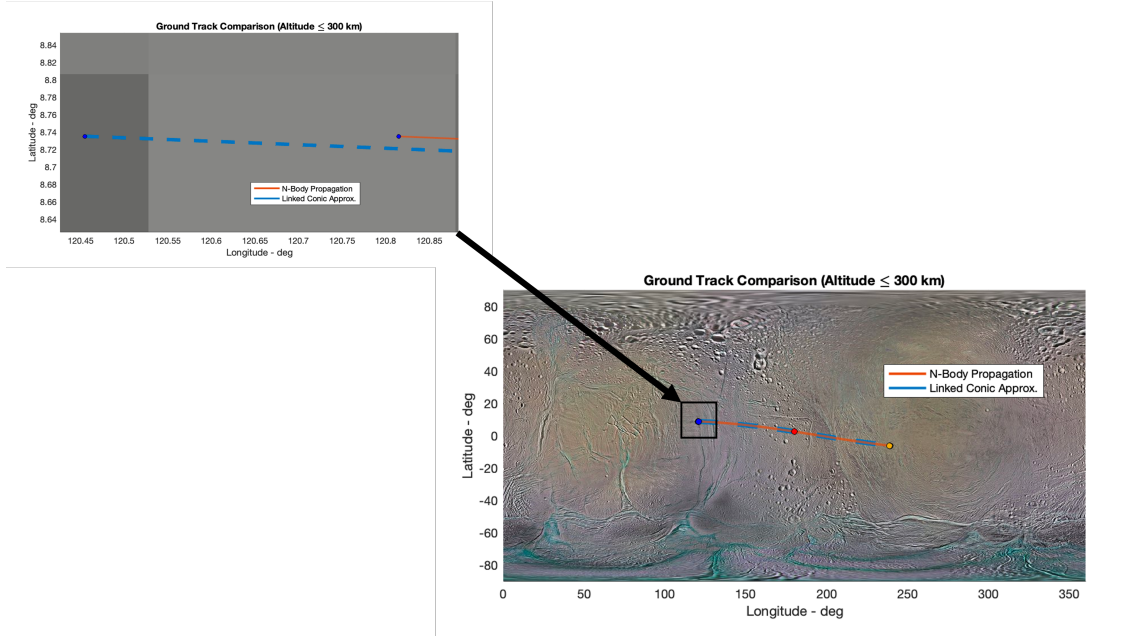


Figure 3.9: Comparison of groundtracks from two-body (linked-conics) and  $n$ -body propagation over a ten-minute interval around the Enceladus flyby. The maximum altitude considered is 300 km. The two trajectories exhibit a maximum deviation of only  $0.01^\circ$  in latitude and  $0.4^\circ$  in longitude. The groundtrack corresponds to a first flyby of a COT sequence(see table 3.1).

The results, presented in Figures 3.9 and 3.10, show that although the maximum Cartesian deviation between the two-body and  $n$ -body flyby trajectories reaches 19 km (see Figure 3.10), the qualitative shape and position of the groundtrack remain essentially unchanged (see Figure 3.9). This is primarily due to the high eccentricity of the flyby, which limits the time spent below 300 km altitude to approximately four minutes (see Figure 3.10).

These results are consistent with expectations and provide a qualitative basis for the global optimisation of  $n$ -body groundtracks towards two-body solutions.

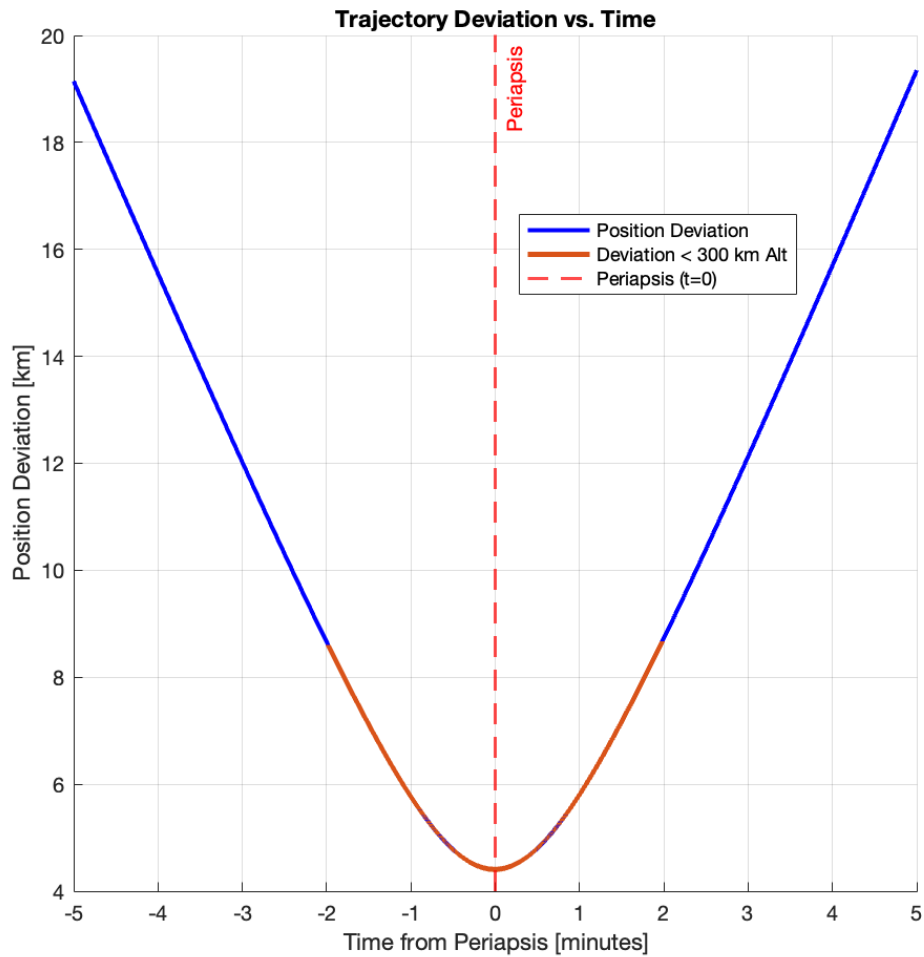


Figure 3.10: Cartesian deviation in kilometres between the two-body (linked-conics) and  $n$ -body propagation over a ten-minute interval around the Enceladus flyby. The red portion of the plot corresponds to the segment of the flyby below 300 km altitude. The maximum deviation is 19 km.

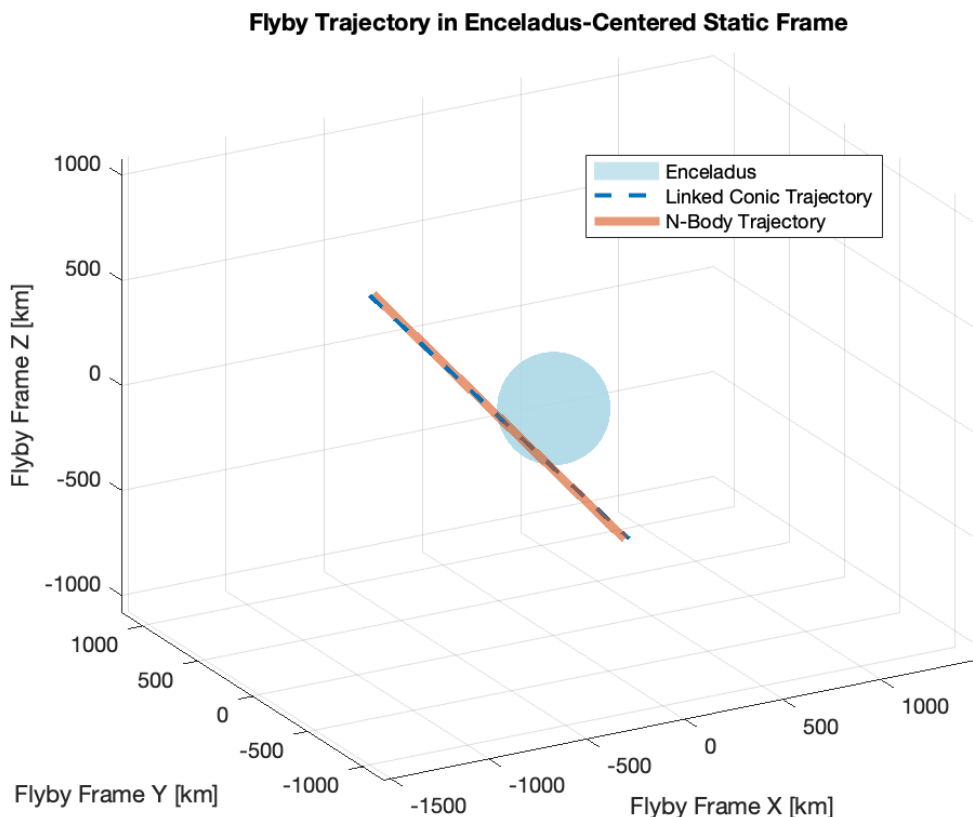


Figure 3.11: Three-dimensional perspective of the flyby. The eccentricity is very high (621.35), and the trajectory appears almost as a straight line.

## 3.4 Global Convergence

This section addresses the objective of implementing an  $n$ -body flyby trajectory optimisation algorithm to refine initial solutions from the linked-conics model, ensuring that the final groundtracks satisfy mission scientific requirements.

To simplify the optimisation problem, a single Enceladus flyby (excluding close approaches to Titan) is considered, with a Trajectory Correction Manoeuvre (TCM) performed at a specified true anomaly before the flyby.

The strategy involves back-propagating the linked-conics trajectory from the centre of Enceladus at the flyby epoch to the TCM epoch, applying a  $\Delta V$ , and then forward-propagating with the  $n$ -body propagator to assess proximity to the target linked-conics trajectory.

The  $n$ -body propagation employs a State Transition Matrix (STM) with the objective of minimising the B-plane targeting error. While this guarantees (see Sec. 3.4.1) correct flyby geometry (maintaining the same pump and crank angles), the flyby epoch may shift, causing a corresponding shift in the groundtrack (see Sec. 3.4.6).

Under this strategy,  $v_\infty$  is not bounded; however, since TCMs are of the order of 100 m/s and  $v_\infty$  is of the order of km/s, the change in  $v_\infty$  is negligible in terms of groundtrack shape variation.

### 3.4.1 B-plane Fundamentals

For high-fidelity trajectory optimisation, B-plane targeting is preferred to the pump and crank angle parameterisation (Section 3.1.2), which exhibits highly non-linear behaviour in response to trajectory correction manoeuvres (TCMs) [57]. The B-plane method provides improved numerical properties, allowing for linearisation and facilitating the convergence of differential correction schemes [58].

The B-plane, or Body-Plane, is an imaginary plane that is orthogonal to the incoming asymptote of a spacecraft's approach trajectory and passes through the centre of the target body [26].

The *B-vector* is a key parameter of this system. It is a vector in the B-plane that extends from the centre of the target body to the piercing point, which is where the spacecraft's trajectory asymptote would intersect the plane if the spacecraft were not influenced by the body's gravity.

#### 3.4.1.1 B-plane Coordinate System

Coordinates in the B-plane are defined by a system of three orthogonal unit vectors, typically denoted  $\hat{S}$ ,  $\hat{T}$ , and  $\hat{R}$ , with the origin at the centre of the target body.

- The  $\hat{S}$  vector is parallel to the spacecraft's incoming velocity vector relative to the target body, also known as the incoming asymptote.[26]
- The  $\hat{T}$  vector lies within the B-plane itself. Its orientation is somewhat arbitrary but is typically aligned with a significant plane, such as the ecliptic plane or the target body's equatorial plane.
- The  $\hat{R}$  vector completes the right-handed orthogonal triad, being normal to both  $\hat{S}$  and  $\hat{T}$ .

The aim point for a flyby is specified in terms of the components of the B-vector along the  $\hat{T}$  and  $\hat{R}$  axes:

$$\mathbf{B} = B_T \hat{T} + B_R \hat{R} \quad (3.27)$$

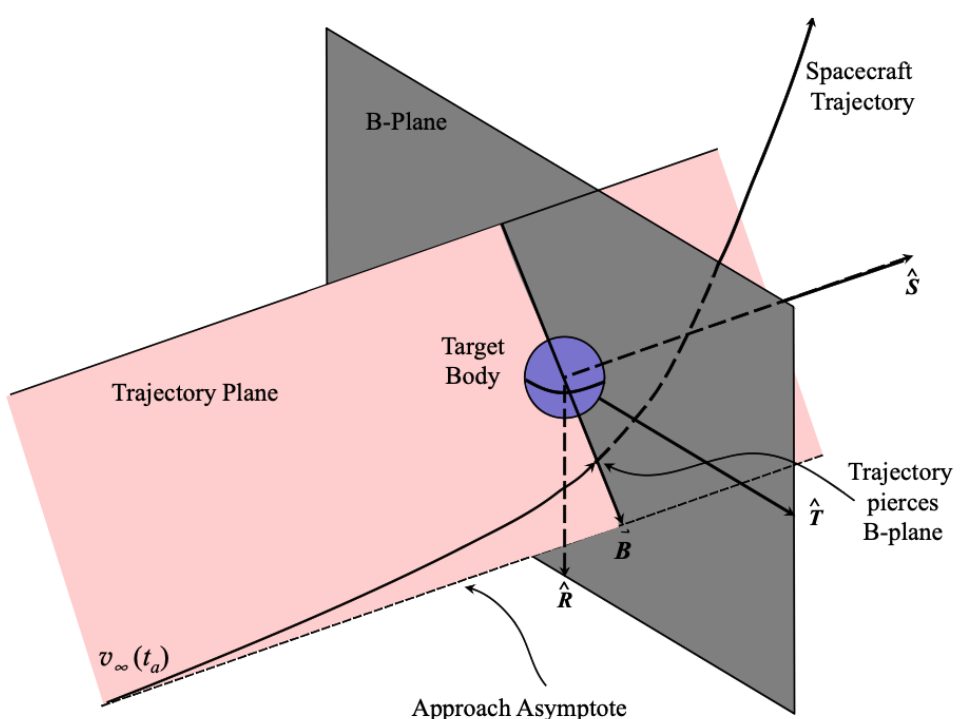


Figure 3.12: B-Plane illustration from Vallado[26]

### 3.4.1.2 B-plane Targeting and Computation

For the purposes of this thesis, B-plane targeting requires two steps:

- Conversion of the linked-conics flyby geometry to B-plane coordinates to define the B-plane target,  $B_{\text{target}}$ .
- Conversion of the  $n$ -body trajectory to B-plane coordinates,  $B_{\text{achieved}}$ , to compute the targeting error  $\Delta B = B_{\text{achieved}} - B_{\text{target}}$  for optimisation.

The transformation from the linked-conics flyby geometry, as defined in Equation 3.15, to B-plane coordinates is performed using a MATLAB implementation of Algorithm 79 from Vallado [26]. This algorithm takes the incoming  $\vec{v}_{\infty}^-$  and outgoing  $\vec{v}_{\infty}^+$  hyperbolic excess velocity vectors as input and returns the B-plane components  $B_T$  and  $B_R$ .

For the  $n$ -body trajectory, the pericentre state is identified as the point of closest approach to Enceladus. The achieved hyperbolic excess velocity is computed from its energy definition:

$$v_{\infty}^2 = v_{p,\text{rel}}^2 - \frac{2\mu_{\text{moon}}}{r_{p,\text{rel}}} \quad (3.28)$$

where:

- $v_{p,\text{rel}}$  is the magnitude of the spacecraft velocity relative to Enceladus at pericentre
- $r_{p,\text{rel}}$  is the magnitude of the spacecraft position relative to Enceladus at pericentre
- $\mu_{\text{moon}}$  is the standard gravitational parameter of Enceladus

Algorithm 78 from Vallado [26] is then implemented in MATLAB to compute the B-plane coordinates  $B_T$  and  $B_R$  from the incoming hyperbolic excess velocity vector  $v_{\infty}$  and the pericentre state  $(\mathbf{r}_p, \mathbf{v}_p)$ .

### 3.4.2 State Transition Matrix (STM) Fundamentals

The state transition matrix (STM) is a fundamental tool in astrodynamics and control theory, providing a linearised mapping between infinitesimal perturbations in the initial state of a dynamical system and the corresponding variations in the final state after a specified time interval [59].

This property renders the STM well suited for the optimisation of B-plane targeting errors via a single trajectory correction manoeuvre (TCM) executed prior to the flyby. By employing the STM, the required state adjustments to minimise the B-plane miss distance can be computed efficiently[60], thereby enhancing targeting accuracy.

When the initial guess is sufficiently close to the true solution, STM-based differential correction methods achieve significantly faster local convergence than global optimisation techniques such as genetic algorithms [61]. As the linked-conics approach yields a suitable initial guess, this method could be particularly effective.

This thesis considers a single trajectory correction manoeuvre (TCM), a variation in the initial velocity and a single flyby, providing a foundation for extension to cases with multiple flybys and TCMs.

#### 3.4.2.1 STM Differential Equation and Gravity Gradient

Mathematically, the state transition matrix (STM) is governed by the differential equation [59]:

$$\frac{d\Phi(t, t_0)}{dt} = A(t) \Phi(t, t_0), \quad \Phi(t_0, t_0) = I_{6 \times 6} \quad (3.29)$$

where  $\Phi(t, t_0)$  is the STM and  $A(t)$  is the Jacobian (dynamic matrix) of the state vector  $\mathbf{X} = [\vec{r} \quad \vec{v}]^\top$  at time  $t$ . Linearisation of the equations of motion  $F(\mathbf{X})$  about a reference state  $\mathbf{X}^*$  yields [62]:

$$\dot{\mathbf{X}} \approx \dot{\mathbf{X}}^* + \frac{\partial F(\mathbf{X}^*)}{\partial \mathbf{X}} \cdot (\mathbf{X} - \mathbf{X}^*) \quad (3.30)$$

where  $\mathbf{X}^*$  is the reference state at  $t_0$ . The matrix  $A(t)$ , comprising the partial derivatives of the acceleration, is given by[63]:

$$\mathbf{A} = \frac{d\mathbf{X}(t)}{d\mathbf{X}_0} = \begin{bmatrix} 0 & 0 & 0 & 1 & 0 & 0 \\ 0 & 0 & 0 & 0 & 1 & 0 \\ 0 & 0 & 0 & 0 & 0 & 1 \\ \frac{\partial a_x}{\partial x} & \frac{\partial a_x}{\partial y} & \frac{\partial a_x}{\partial z} & 0 & 0 & 0 \\ \frac{\partial a_y}{\partial x} & \frac{\partial a_y}{\partial y} & \frac{\partial a_y}{\partial z} & 0 & 0 & 0 \\ \frac{\partial a_z}{\partial x} & \frac{\partial a_z}{\partial y} & \frac{\partial a_z}{\partial z} & 0 & 0 & 0 \end{bmatrix} \quad (3.31)$$

where  $a_x$ ,  $a_y$ , and  $a_z$  are the accelerations along the  $X$ ,  $Y$ , and  $Z$  axes, respectively.

This may be written more compactly as [64]:

$$A(t) = \begin{bmatrix} 0_{3 \times 3} & I_{3 \times 3} \\ G(t) & 0_{3 \times 3} \end{bmatrix} \quad (3.32)$$

where  $I$  is the identity matrix and  $G(t)$  is the gravity gradient matrix[64], representing the sensitivity of the acceleration to position.

### 3.4.2.2 Gravity Gradient Matrix for Central Body and $J_2$

To perform the optimisation, the differential equation 3.29 must be integrated concurrently with the  $n$ -body equations of motion 3.23. Therefore, the gravity gradient matrix  $G(t)$ , the second derivative of the gravitational potential[65], for both  $n$ -body perturbations and the  $J_2$  zonal harmonic must be computed.

For a point mass, the gravitational potential  $U$  is given by:

$$U = \frac{\mu}{r} \quad (3.33)$$

where  $r = \|\vec{r}\|$  is the distance from the body.

The gravity gradient matrix is obtained by differentiating each acceleration component with respect to each position component, yielding[65]:

$$G_{point-mass} = -\frac{\mu}{r^3} I_{3 \times 3} + \frac{3\mu}{r^5} (\vec{r} \otimes \vec{r}^T) \quad (3.34)$$

where  $I$  is the identity matrix and  $\vec{r} \otimes \vec{r}^T$  denotes the outer product of the position vector.

For the harmonic  $J_2$  due to Saturn oblateness, the gravity potential is[49]:

$$U = \frac{\mu}{r} \left[ 1 - J_2 \left( \frac{R}{r} \right)^2 \frac{1}{2} (3 \sin^2 \varphi - 1) \right] \quad (3.35)$$

where  $R$  is the reference equatorial radius of the central body, and  $\varphi$  is the latitude (angle from the equatorial plane), so  $\sin(\varphi) = z/r$ .

The corresponding gravity gradient matrix  $\mathbf{G}_{J2}$  is derived analytically by differentiating the above expression with respect to position[66]:

$$\mathbf{G}_{J2} = -\frac{3}{2} \frac{\mu J_2 R^2}{r^5} \begin{bmatrix} G'_{xx} & G'_{xy} & G'_{xz} \\ G'_{yx} & G'_{yy} & G'_{yz} \\ G'_{zx} & G'_{zy} & G'_{zz} \end{bmatrix} \quad (3.36)$$

Where the matrix components,  $G'_{ij}$ , are given by:

$$\begin{aligned}
G'_{xx} &= \left(1 - \frac{5z^2}{r^2}\right) \left(1 - 5\frac{x^2}{r^2}\right) - 2\frac{x^2}{r^2} \\
G'_{yy} &= \left(1 - \frac{5z^2}{r^2}\right) \left(1 - 5\frac{y^2}{r^2}\right) - 2\frac{y^2}{r^2} \\
G'_{zz} &= \left(3 - \frac{5z^2}{r^2}\right) \left(1 - 5\frac{z^2}{r^2}\right) - 2\left(1 - \frac{3z^2}{r^2}\right) \\
G'_{xy} = G'_{yx} &= -5xy\frac{1}{r^2} \left(1 - 7\frac{z^2}{r^2}\right) \\
G'_{xz} = G'_{zx} &= -5xz\frac{1}{r^2} \left(3 - 7\frac{z^2}{r^2}\right) \\
G'_{yz} = G'_{zy} &= -5yz\frac{1}{r^2} \left(3 - 7\frac{z^2}{r^2}\right)
\end{aligned} \tag{3.37}$$

where  $x$ ,  $y$ , and  $z$  are the Cartesian components of the position vector  $\vec{r}$ . The  $\sin(\phi)$  term from Eq. 3.35 is substituted with  $z/r$  to express the matrix entirely in Cartesian coordinates.

### 3.4.3 Velocity Correction via Pseudo-Inverse

#### 3.4.3.1 Formulation of the Correction Problem

The correction of the initial velocity to minimise the B-plane targeting error is formulated as a linear system. The sensitivity matrix  $H$  relates changes in the initial velocity to changes in the B-plane parameters[67]:

$$H = \frac{\partial B}{\partial \vec{v}_0} = \begin{bmatrix} \frac{\partial B_R}{\partial v_{x0}} & \frac{\partial B_R}{\partial v_{y0}} & \frac{\partial B_R}{\partial v_{z0}} \\ \frac{\partial B_T}{\partial v_{x0}} & \frac{\partial B_T}{\partial v_{y0}} & \frac{\partial B_T}{\partial v_{z0}} \end{bmatrix} \tag{3.38}$$

The  $2 \times 3$  sensitivity matrix is formed by multiplying the Jacobian of the B-plane parameters with respect to the periapsis state by the state transition matrix (STM) at periapsis, retaining only the velocity columns.

The linearised relationship between the B-plane error  $\Delta B$  and the velocity

$$H \cdot \delta \vec{v}_0 \approx -\Delta B \tag{3.39}$$

As  $H$  is not square, the system is underdetermined and admits infinitely many solutions. While  $3 \times 3$  formulations including arrival time constraints are common in the literature [67], the present  $2 \times 3$  approach introduces an additional degree of freedom. Numerical results for the Enceladus flyby scenario indicate that this formulation is sufficient: timing discrepancies of less than 30 minutes produce only minor groundtrack variations

(see Sec. 3.4.6), and the pseudo-inverse algorithm converges within acceptable time deviations. The minimum-norm solution, corresponding to the smallest required velocity change, is obtained using the Moore–Penrose pseudo-inverse [68]:

$$H^+ = H^T (HH^T)^{-1} \quad (3.40)$$

The velocity correction is then:

$$\delta\vec{v}_0 = -H^+ \Delta B = -H^T (HH^T)^{-1} \Delta B \quad (3.41)$$

This approach ensures that the computed correction minimises the Euclidean norm of  $\delta\vec{v}_0$ , yielding the most fuel-efficient manoeuvre. In practice, the pseudo-inverse is computed numerically (e.g., using `pinv(H)` [69] in MATLAB).

### 3.4.3.2 Computation of the Sensitivity Matrix

The sensitivity of the B-plane parameters to the initial state is computed using the chain rule:

$$\frac{\partial B}{\partial X_0} = \frac{\partial B}{\partial X_{\text{peri}}} \frac{\partial X_{\text{peri}}}{\partial X_0} \quad (3.42)$$

Here,  $\frac{\partial X_{\text{peri}}}{\partial X_0}$  is the STM evaluated at periapsis. Since only the initial velocity is adjusted, the relevant submatrix is extracted to form  $H$ .

In practice, the sensitivity matrix  $H = \frac{\partial B}{\partial \vec{v}_0}$  is computed using numerical differentiation in MATLAB rather than analytical expressions. For each velocity component  $v_i$ , the B-plane parameters are evaluated with a small perturbation  $\varepsilon = 10^{-6}$  km/s:

$$\frac{\partial B_j}{\partial v_i} = \frac{B_j(\vec{v}_0 + \varepsilon \hat{e}_i) - B_j(\vec{v}_0)}{\varepsilon} \quad (3.43)$$

where  $\hat{e}_i$  is the unit vector in the  $i$ -th direction and  $j \in \{R, T\}$ .

### 3.4.4 Iterative Correction Procedure and Verification

The STM-based B-plane targeting algorithm employs a true anomaly-based backward propagation combined with iterative differential correction. This approach is applicable to a single flyby; for multiple flybys, a Poincaré section[63] is preferable, as the eccentricity vector oscillates in the  $n$ -body problem.

### 3.4.4.1 True Anomaly-Based Initial Condition Setup

Rather than using arbitrary backward propagation times, the algorithm uses true anomaly changes to establish consistent initial conditions. Starting from the linked-conics flyby state, the spacecraft is propagated backward by a specified true anomaly increment (typically  $50^\circ$ - $150^\circ$ ) to provide sufficient separation from the flyby epoch for meaningful corrections.

The backward propagation uses an event detection function that monitors the true anomaly change:

$$\Delta v = v_{\text{initial}} - v_{\text{current}} = v_{\text{target}} \quad (3.44)$$

where the angular change is computed accounting for the  $2\pi$  periodicity of true anomaly.

### 3.4.4.2 Iterative Correction with Singularity Avoidance

Adaptive singularity avoidance is implemented during optimisation to address close approaches to perturbing bodies. Specifically, a distance threshold of Enceladus mean radius ( $d_{\min,2} = 252$  km) is applied: within this limit, third-body contributions to the gravity gradient matrix are omitted from the STM computation. This measure prevents the propagation of trajectories that, after B-plane correction, would otherwise result in impact with Enceladus.

### 3.4.4.3 Convergence Criteria and Verification

The algorithm terminates when the B-plane targeting error falls below  $\varepsilon = 0.01$  km or after a maximum of 25 iterations. The damping factor  $\alpha = 0.7$  enhances stability by preventing overshoot corrections that could lead to oscillatory behaviour. Upon convergence, the corrected initial state is propagated forward using the complete  $n$ -body model to verify the achieved periapsis altitude and final B-plane parameters, thereby confirming compliance with mission constraints.

### 3.4.5 Algorithm Summary

The complete procedure for the STM-based B-plane targeting described in Section 3.4 is summarised below:

---

**Algorithm 2** True Anomaly-Based STM B-plane Targeting
 

---

**Require:** Linked-conics flyby parameters, backward true anomaly  $\Delta v_{\text{back}}$ , B-plane tolerance  $\varepsilon$

**Ensure:** Corrected initial state, required  $\Delta V$ , final B-plane parameters

- 1: Compute target B-plane parameters  $B_{\text{target}}$  from linked-conics model
  - 2: Calculate initial state at flyby epoch from linked-conics geometry
  - 3: Determine initial true anomaly  $v_0$  from flyby state
  - 4: Propagate backward using event detection until  $\Delta v = \Delta v_{\text{back}}$
  - 5: Extract initial state  $X_0$  at backward propagation endpoint
  - 6: Set epoch offset  $t_{\text{offset}}$  for n-body ephemeris synchronisation
  - 7: Initialise total  $\Delta V = 0$ , damping factor  $\alpha = 0.7$
  - 8: **repeat**
  - 9:   Propagate forward using n-body dynamics with STM integration
  - 10:   Apply singularity avoidance: exclude perturbations if  $d < d_{\min,1}$
  - 11:   Compute STM gravity gradient with threshold  $d_{\min,2}$
  - 12:   Find periapsis as minimum distance to target body
  - 13:   Extract periapsis state  $X_{\text{peri}}$  and STM  $\Phi(t_{\text{peri}}, t_0)$
  - 14:   Compute achieved B-plane parameters from periapsis state
  - 15:   Calculate targeting error  $\Delta B = B_{\text{achieved}} - B_{\text{target}}$
  - 16:   Compute B-plane sensitivity  $\frac{\partial B}{\partial X_{\text{peri}}}$  numerically
  - 17:   Form sensitivity matrix  $H = \frac{\partial B}{\partial X_{\text{peri}}} \cdot \Phi_v$
  - 18:   Calculate velocity correction  $\delta v_0 = -H^+ \Delta B$
  - 19:   Apply damped update:  $v_0 \leftarrow v_0 + \alpha \cdot \delta v_0$
  - 20:   Update total  $\Delta V += |\alpha \cdot \delta v_0|$
  - 21:   **until**  $\|\Delta B\| < \varepsilon$  or maximum iterations reached
  - 22:   Verify final solution through forward propagation
  - 23:   Compute final periapsis altitude and B-plane accuracy
  - 24: **return** Corrected initial state, total  $\Delta V$ , convergence status
-

```
== STM OPTIMIZATION FOR B-PLANE TARGETING ==
B_R = -30.147649 km   B_T = 278.345753 km   |B| = 279.973640 km
Periapse Velocity: 4.006 km/s, Periapse Altitude: 27.423 km
```

```
== TRUE ANOMALY BACKWARD PROPAGATION ==
Initial true anomaly: 0.01 degrees
Target backward propagation: 100.00 degrees
Time duration: 11.89 hours (0.496 days)
Final true anomaly: 259.91 degrees
Starting STM optimization...
Forward propagation duration: 23.78 hours
```

Iter	B_R Error	B_T Error	Total Error	DeltaV	Time Diff (min)
1	30.147650	-278.345754	279.973641	0.000 m/s	-0.024
2	10.471118	-98.778009	99.331462	3.519 m/s	0.547
3	3.090212	-29.585377	29.746326	4.872 m/s	0.737
4	0.914898	-8.871656	8.918706	5.277 m/s	0.832
5	0.274260	-2.661150	2.675245	5.398 m/s	0.832
6	0.082259	-0.798313	0.802540	5.434 m/s	0.832
7	0.024676	-0.239491	0.240759	5.445 m/s	0.832
8	0.007403	-0.071847	0.072227	5.448 m/s	0.832
9	0.002221	-0.021554	0.021668	5.449 m/s	0.832
10	0.000666	-0.006466	0.006500	5.450 m/s	0.832

Optimization CONVERGED in 10 iterations!

Final B-plane errors:  
 B\_R error: 0.000666 km  
 B\_T error: -0.006466 km  
 Total error: 0.006500 km

Required Correction:  
 DeltaV magnitude: 5.450 m/s  
 DeltaV vector: [-1.307501, -4.972017, 1.807526] m/s  
 Linked Conics Period: 230.87 hours  
 Propagation Duration (T\_LC/2.1): 115.43 hours each direction  
 N-Body initial epoch: 10957.004491 MJD2000 (11.89 hours before flyby)  
 Linked Conics reference epoch: 10957.500000 MJD2000 (flyby epoch)

Figure 3.13: Screenshot of the STM B-plane targeting algorithm outputs in MATLAB command window. The algorithm converges in 10 iterations with a quasi-ballistic  $\Delta V$  of 5.45 m/s, 0.832 minutes of flyby epoch difference and a final B-plane error of 0.002 km. The flyby geometry is defined by  $\text{node}_{\text{in}} = [4, 8.6918, -86.9406]$  and  $\text{node}_{\text{out}} = [4, 8.6918, -88.1610]$ . The periapsis altitude is constrained to be above 10 km; the epoch of the linked-conics flyby is 1 January 2030. The perturbing bodies considered, in addition to Saturn, are Saturn  $J_2$ , the Sun, Titan, and Enceladus.

### 3.4.6 Final Results

A sweep analysis was performed by varying the backward true anomaly propagation from 15 to 255 degrees in steps of 5 degrees.

The scenario considered is a single Enceladus flyby (excluding close approaches to Titan). The flyby epoch, aside from phasing, does not significantly affect the orbital geometry, as the principal perturbers, namely the Sun and Saturn's  $J_2$ , exhibit relatively constant influence with respect to Enceladus.

Figure 3.14 presents the results of the true anomaly sweep for the trajectory defined by  $\text{node}_{\text{in}} = [4, 8.6918, -86.9406]$  and  $\text{node}_{\text{out}} = [4, 8.6918, -88.1610]$  (as in ??).

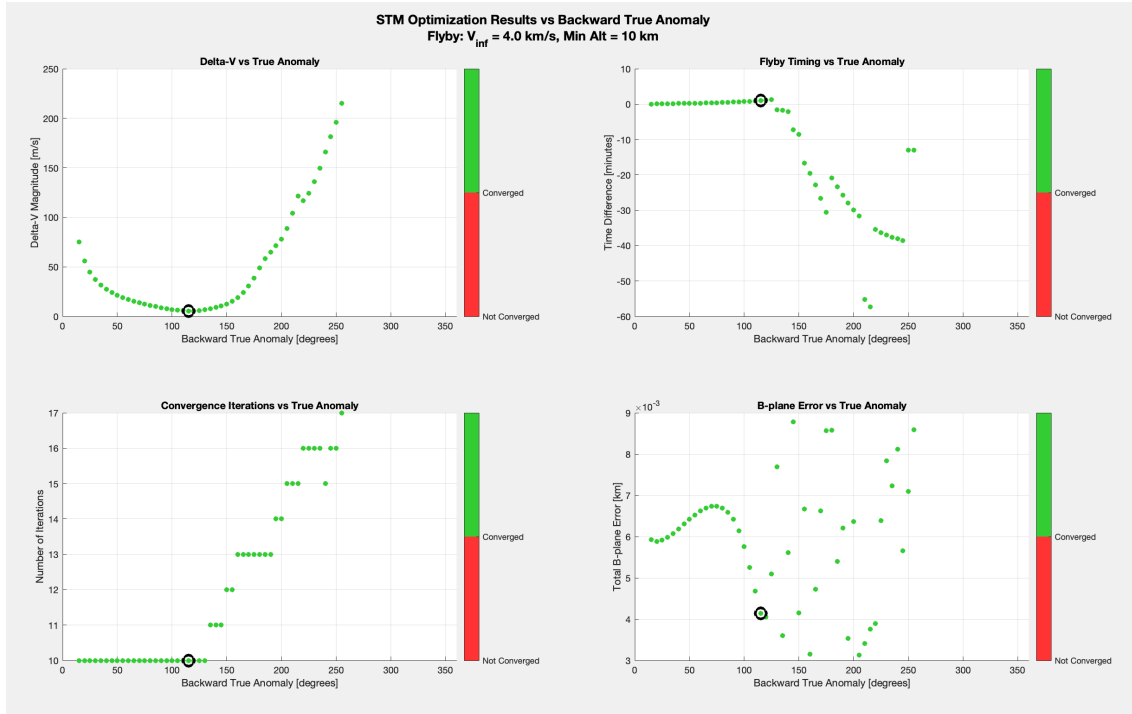


Figure 3.14: Results of the STM B-plane targeting algorithm for various backward true anomaly propagations. The flyby geometry is defined by  $\text{node}_{\text{in}} = [4, 8.6918, -86.9406]$  and  $\text{node}_{\text{out}} = [4, 8.6918, -88.1610]$ . The periapsis altitude is constrained to be above 10 km; the epoch of the linked-conics flyby is 1 January 2030. The perturbing bodies considered, in addition to Saturn, are Saturn  $J_2$ , the Sun, Titan, and Enceladus. The upper left plot shows the required  $\Delta V$ ; the upper right plot shows the difference in minutes between the periapsis epochs of the  $n$ -body and linked-conics solutions; the lower left plot shows the number of iterations to convergence; and the lower right plot shows the final B-plane targeting error.

The range of 15–255 degrees was selected to avoid excessive  $\Delta V$  requirements. Small true anomaly back-propagations do not provide sufficient time for significant deviation from the centre of Enceladus, as the reference linked-conics trajectory is computed to intersect its centre. Conversely, large true anomaly propagations increase the influence

of  $n$ -body perturbations, making it more challenging to match the ideal two-body linked-conics trajectory without incurring high  $\Delta V$ . Analysis of Table 3.4.6 and Figure 3.14 demonstrates that the algorithm reliably converges within 25 iterations, achieving a B-plane targeting error below 0.01 km. This confirms that the initial guess is well posed and that the damping factor  $\alpha = 0.7$  is suitably selected.

The optimal interval for the backward true anomaly lies between 50 and 125 degrees, where the required  $\Delta V$  remains below 20 m/s and the flyby epoch offset does not exceed 1.5 minutes. Within this range, the resulting groundtrack is virtually indistinguishable from the reference solution (see Fig. 3.15).

For true anomaly values between 125 and 205 degrees, the required  $\Delta V$  remains below 100 m/s and the maximum flyby epoch difference is 30 minutes. This yields groundtracks with substantial overlap, although some divergence is observed (see Fig. 3.16). Such timing discrepancies may be significant for illumination-sensitive operations, as discussed in Section 2.2. While eclipses of the entire groundtrack by Saturn are not uncommon, the terminator advances slowly (360 degrees in 31.5 h, i.e., one Enceladus day), so a 30-minute offset has limited shift of about 6 degrees on groundtrack illumination.

Table 3.2: Results of the STM B-plane targeting algorithm for various backward true anomaly propagations. The flyby geometry is defined by  $\text{node}_{\text{in}} = [4, 8.6918, -86.9406]$  and  $\text{node}_{\text{out}} = [4, 8.6918, -88.1610]$ . The periapsis altitude is constrained to be above 10 km; the epoch of the linked-conics flyby is 1 January 2030. The perturbing bodies considered, in addition to Saturn, are Saturn  $J_2$ , the Sun, Titan, and Enceladus.

True Anomaly	15°	20°	25°	30°	35°	40°	45°	50°	55°	60°	65°	70°
Delta V burn (m/s)	75.005	56.046	44.672	37.051	31.551	27.360	24.031	21.298	18.994	17.007	15.264	13.711
Pericentre epoch diff. (min)	-0.063	0.085	0.107	0.130	0.154	0.179	0.206	0.236	0.269	0.307	0.351	0.404
Number of iterations	10	10	10	10	10	10	10	10	10	10	10	10
B-plane targeting error (km)	0.00593	0.00588	0.00591	0.00598	0.00608	0.00619	0.00632	0.00647	0.00664	0.00682	0.00702	0.00723

True Anomaly	75°	80°	85°	90°	95°	100°	105°	110°	115°	120°	125°	130°
Delta V burn (m/s)	12.313	11.042	9.880	8.818	7.852	6.993	6.265	5.714	5.410	5.430	5.824	6.587
Pericentre epoch diff. (min)	0.470	0.554	0.664	0.815	1.031	1.346	1.831	2.617	3.967	6.435	11.057	19.785
Number of iterations	10	10	10	10	10	10	10	10	10	10	10	10
B-plane targeting error (km)	0.00747	0.00772	0.00799	0.00829	0.00861	0.00896	0.00934	0.00976	0.01022	0.01073	0.01130	0.01194

True Anomaly	135°	140°	145°	150°	155°	160°	165°	170°	175°	180°	185°	190°
Delta V burn (m/s)	7.671	9.022	10.625	12.584	15.138	18.642	23.566	30.529	40.332	54.155	73.738	101.669
Pericentre epoch diff. (min)	36.578	68.542	127.680	235.710	430.570	779.830	1399.900	2489.800	4384.200	7655.300	13237.000	22593.000
Number of iterations	10	10	10	10	10	10	10	10	10	10	10	10
B-plane targeting error (km)	0.01267	0.01350	0.01446	0.01538	0.01689	0.01846	0.02036	0.02269	0.02557	0.02919	0.03380	0.03976

True Anomaly	195°	200°	205°	210°	215°	220°	225°	230°	235°	240°	245°	250°	255°
Delta V burn (m/s)	141.774	199.668	282.570	398.860	559.364	778.397	1075.390	1476.290	2014.090	2731.320	3682.860	4937.020	6572.830
Pericentre epoch diff. (min)	37807.000	61558.000	96471.000	146251.000	214965.000	308062.000	43159.000	502397.000	790027.000	1062150.000	1394030.000	1810680.000	2332440.000
Number of iterations	10	11	11	12	13	13	14	15	15	16	16	16	17
B-plane targeting error (km)	0.04754	0.05775	0.07120	0.08897	0.11238	0.14317	0.18356	0.23642	0.30549	0.39556	0.51250	0.66332	0.85627

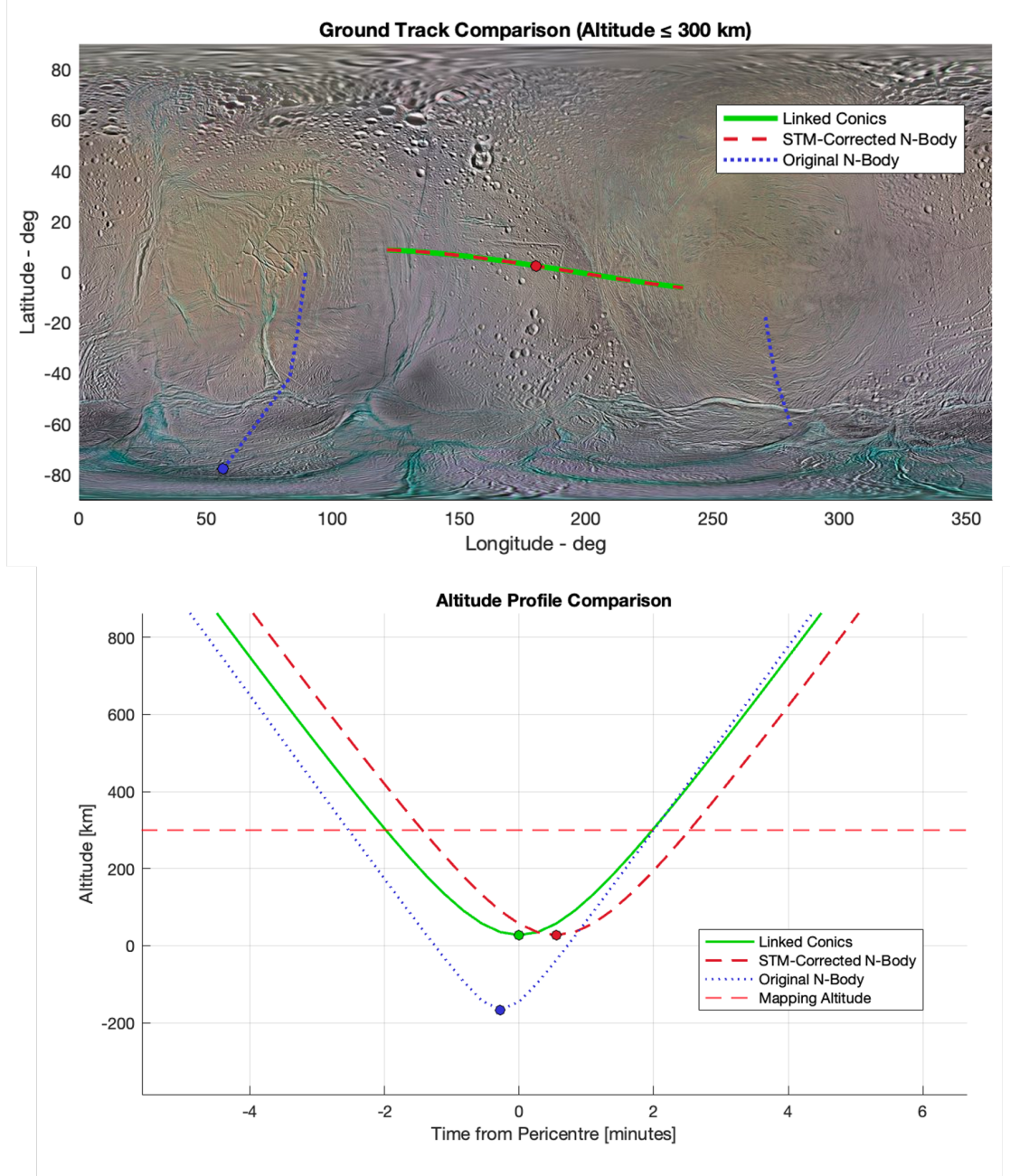


Figure 3.15: Groundtracks and altitude profiles as a function of time from pericentre for a 100-degree true anomaly back-propagation. Three trajectories are shown: the linked-conics solution with the virtual pericentre state propagated in the two-body model (see Sec. 3.1.2), the original  $n$ -body trajectory, and the corrected  $n$ -body trajectory following STM B-plane targeting (see Algorithm 3.4.5). The maximum altitude considered is 300 km. The maximum deviation between the two trajectories is  $0.01^\circ$  in latitude and  $0.04^\circ$  in longitude. The groundtrack corresponds to the first flyby of a COT sequence (see Table 3.1). The original  $n$ -body trajectory impacts Enceladus.

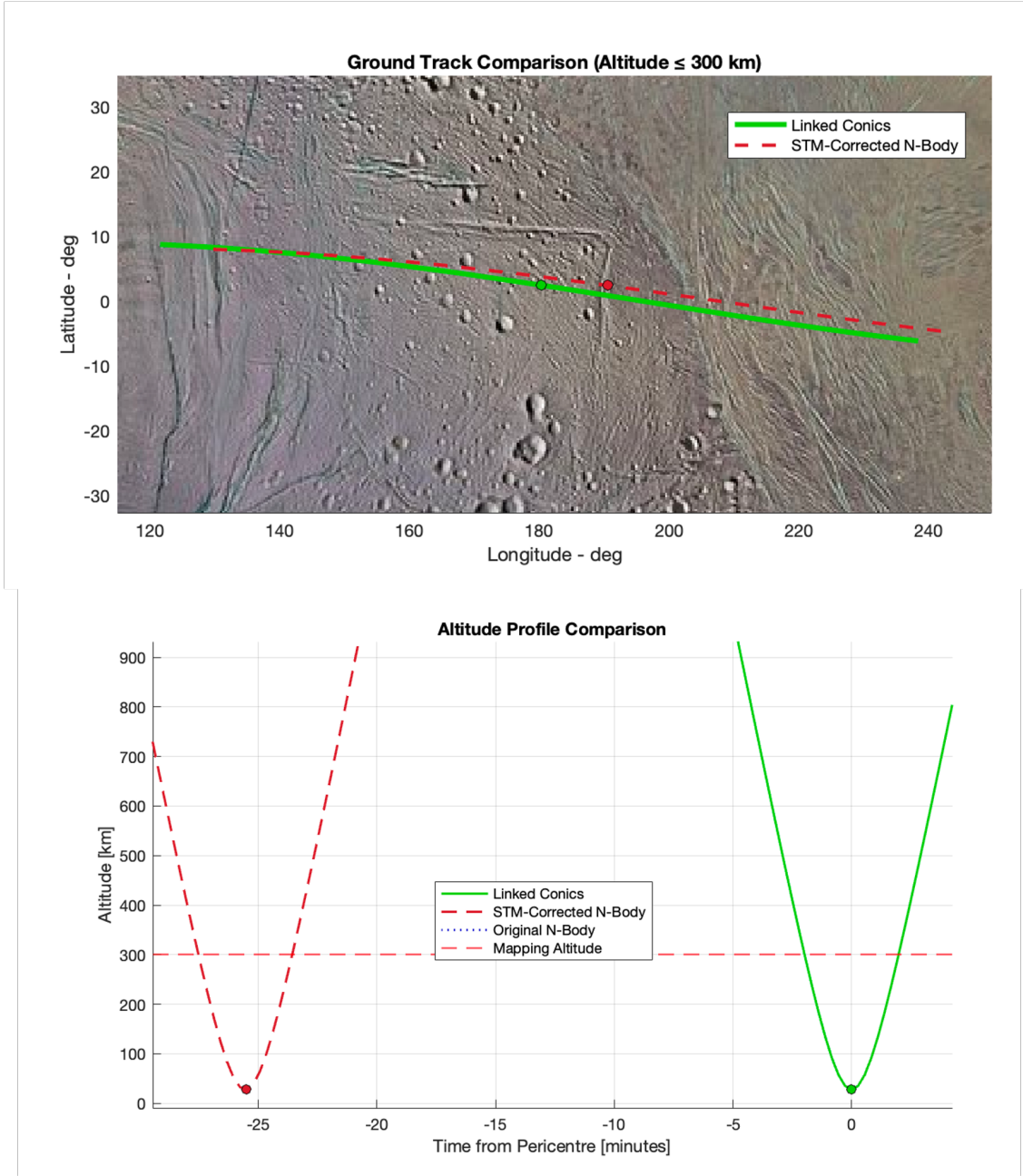


Figure 3.16: Groundtracks and altitude profiles as a function of time from pericentre for a 170-degree true anomaly back-propagation. Two trajectories are shown: the linked-conics solution with the virtual pericentre state propagated in the two-body model (see Sec. 3.1.2) and the corrected  $n$ -body trajectory following STM B-plane targeting (see Algorithm 3.4.5), as the original  $n$ -body trajectory deviates excessively from the linked-conics solution. Even with a 30-minute difference in flyby epoch, the groundtracks largely overlap. The groundtrack corresponds to the first flyby of a COT sequence (see Table 3.1).

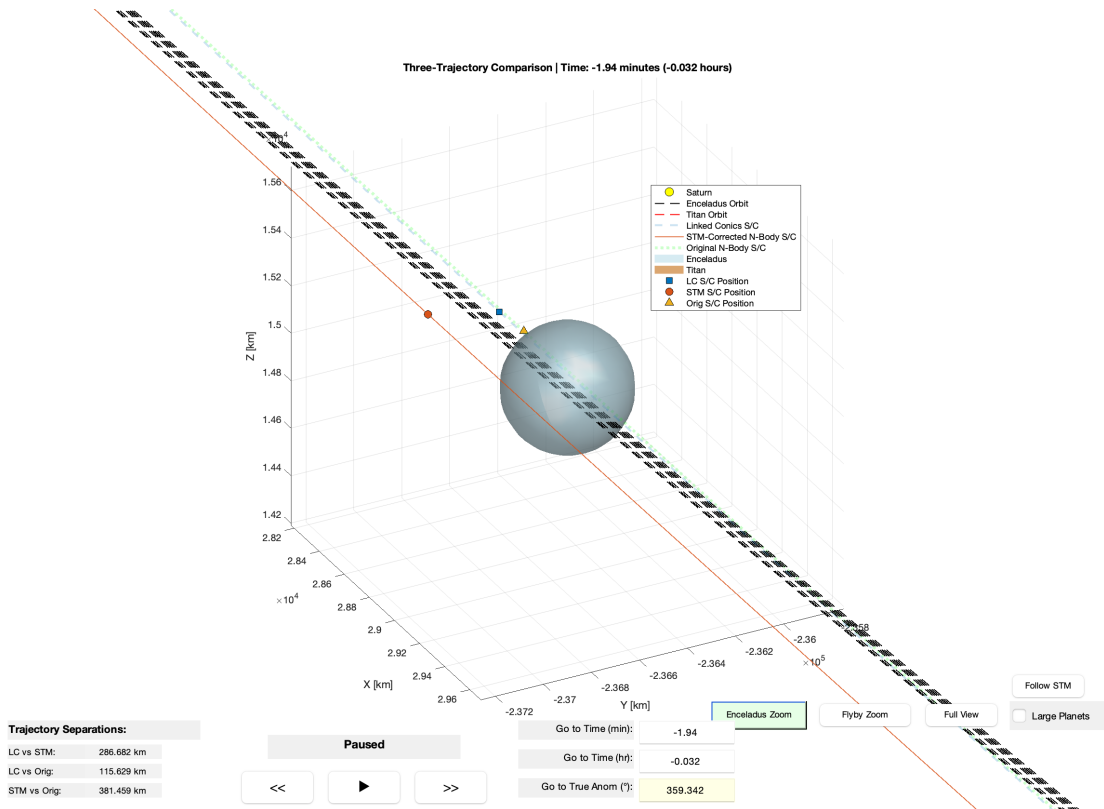


Figure 3.17: Visualisation of the three-dimensional flyby scenario using custom-built MATLAB animation software. The snapshot, taken two minutes prior to periapsis, shows that both the linked-conics and original  $n$ -body trajectories result in impact with Enceladus, whereas the corrected  $n$ -body trajectory avoids collision and satisfies the flyby constraints. Enceladus orbit is represented as multiple black dashed lines, since its orbital elements osculates due to full  $n$ -body SPICE ephemeris effects.

# Chapter 4

## Conclusions and future work

This chapter summarises the research’s key findings and outlines future research directions. The main achievements in illumination modelling and trajectory optimisation for Enceladus missions are presented, followed by proposed enhancements to the framework. These improvements focus on extending the n-body trajectory optimisation to handle multiple flyby scenarios and incorporating advanced multi-burn optimisation techniques.

### 4.1 Conclusions

This research successfully addressed the high fidelity refinements of the groundtracks in the context of Enceladus exploration missions. The work achieved its principal aim of enhancing the GIGANTES toolbox through the development and integration of illumination modelling and trajectory optimisation capabilities.

**Illumination Modelling Achievements:** A high-fidelity illumination model was developed, accurately accounting for both the terminator and Saturn-induced eclipses on Enceladus. Validation against SPICE routines under the spherical Enceladus assumption demonstrated excellent agreement, with subsolar point calculations differing by less than  $10^{-10}$  degrees and Saturn eclipse timing accurate to within 1 second. The analysis revealed that Saturn eclipses are frequent and long-lasting—occurring every 31.5 hours near equinox and lasting up to 2 hours 43 minutes—highlighting the importance of their inclusion in mission analysis. In contrast, eclipses caused by minor moons were found to be infrequent and brief, with maximum durations under 13 minutes, justifying their exclusion from the computational framework. The resulting illumination model enables precise assessment of groundtrack lighting conditions, supports filtering based on Sun incidence angles, and facilitates effective visualisation, thereby providing a robust tool for Enceladus mission design.

**N-body Dynamics and Trajectory Optimisation:** The identification of principal perturbers in addition to Enceladus and Saturn: Sun, Saturn’s  $J_2$  zonal harmonic, and Titan, accounts for over 99.9% of trajectory perturbations, enabling computationally efficient yet accurate propagation. Despite maximum Cartesian deviations of 19 km between

two-body and n-body solutions during local propagation, the groundtrack geometry remains qualitatively preserved, confirming the suitability of linked-conics solutions as initial guesses.

**Operational Performance:** The STM-based B-plane targeting algorithm exhibits reliable convergence, achieving targeting errors below 0.01 km within 25 iterations across the tested parameter space. The current optimisation approach operates within a simplified model involving a single Enceladus flyby (excluding close approaches to Titan), with a Trajectory Correction Manoeuvre (TCM) executed at a specified true anomaly prior to the flyby. The methodology demonstrates optimal performance for true anomaly back-propagations between  $50^\circ$  and  $125^\circ$ , requiring velocity corrections below 20 m/s and maintaining flyby epoch differences under 1.5 minutes. Within this interval, corrected n-body groundtracks are effectively indistinguishable from their linked-conics equivalents. For larger corrections up to  $205^\circ$ , the algorithm sustains acceptable performance, with  $\Delta V$  requirements below 100 m/s and timing discrepancies under 30 minutes, yielding groundtracks with substantial overlap that remain scientifically valid.

The integrated approach successfully bridges the gap between rapid preliminary design capabilities and high-fidelity mission analysis requirements, providing mission designers with reliable tools for Enceladus flyby optimisation while maintaining computational efficiency suitable for the extensive parameter space exploration required by the GIGANTES framework.

## 4.2 Future work

### 4.2.1 Illumination improvements

Although the current illumination model provides high accuracy, further improvements are possible. One logical extension is to adopt an ellipsoidal shape model for Enceladus, which would address the minor discrepancies identified in Sec. 2.1.3. Additionally, enhancing computational efficiency would be beneficial, especially as illumination constraints become integrated into trajectory optimisation routines. While GIGANTES is not intended for real-time navigation, faster illumination calculations would enable more efficient mapping and optimisation, ensuring that the inclusion of lighting constraints does not significantly slow down the trajectory search process. These improvements would support the design of more realistic and computationally tractable mapping missions that fully account for surface illumination.

### 4.2.2 N-body multiple flyby improvements

On the contrary for the n-body trajectory optimisation, there are several avenues for future work. The current implementation focuses on a single Enceladus flyby scenario with only one TCM at an arbitrary selected true anomaly.

### 4.2.2.1 Multiple only Enceladus flyby

The first enhancement would be to enable sequences of multiple Enceladus flybys, such as a complete Crank-over-the-Top (COT) sequence (see Table 4.2.2.1). As the State Transition Matrix (STM) approach converges only locally, a new, well-informed initial guess should be generated for each subsequent flyby. These factors could be considered:

1. The effect of the  $J_2$  zonal harmonic on the precession of the lines of apsides and nodes, particularly for orbits with low inclination and eccentricity [26]:

$$\begin{aligned}\Delta\Omega &= -3\pi \cdot \frac{J_2}{GM_e a^2} \\ \Delta\omega &= +6\pi \cdot \frac{J_2}{GM_e a^2}\end{aligned}\quad (4.1)$$

where:

- $\Delta\Omega$  is the change in longitude of the ascending node per orbit (radians).
  - $\Delta\omega$  is the change in argument of periapsis per orbit (radians).
  - $J_2$  is the second zonal harmonic coefficient of the central body (dimensionless).
  - $G$  is the gravitational constant ( $\text{m}^3 \text{kg}^{-1} \text{s}^{-2}$ ).
  - $M_e$  is the mass of the central body (kg).
  - $a$  is the semi-major axis of the orbit (m).
2. As the orbital elements are osculating in the n-body context, a simple n-body propagation (without STM) should be used to estimate an updated period for the next flyby.
  3. If further convergence is required, the model could be upgraded to a restricted three-body problem, employing non-circular orbits and SPICE ephemerides to account for Sun perturbations.

Event	$V_\infty$ [km/s]	$\alpha_{in}$ [deg]	$\alpha_{out}$ [deg]	$k_{in}$ [deg]	$k_{out}$ [deg]	$\Delta V$ [m/s]
<b>Starting Crank Targeting Manoeuvre</b>	4	8.6918	8.6918	0	-86.9406	95.62
<b>Partial-COT 1 (O/I)</b>						
1 <sup>st</sup> Flyby	4	8.6918	8.6918	-86.9406	-88.1610	-
2 <sup>nd</sup> Flyby	4	8.6918	8.6918	-88.1610	-89.3871	-
3 <sup>rd</sup> Flyby	4	8.6918	8.6918	-89.3871	-90.6075	-
4 <sup>th</sup> Flyby	4	8.6918	8.6918	-90.6075	-91.8337	-
5 <sup>th</sup> Flyby	4	8.6918	8.6918	-91.8337	-93.0598	-

Table 4.1: COT sequence flyby parameters.

While these enhancements yield improved initial guesses, a quantitative trade-off analysis should be conducted to assess the benefits in optimisation convergence relative to the increased computational cost.

Delta-v manoeuvres in this context would be evaluated via a simple parametric sweep of the true anomaly, as previously implemented in this thesis.

#### 4.2.2.2 Multiple burns

To optimise delta-v manoeuvres beyond simple parametric sweeps, primer vector theory provides a rigorous mathematical framework for determining optimal burn locations and magnitudes. Originally developed by Lawden [70], primer vector theory establishes necessary conditions for optimal impulsive transfers through the analysis of costate variables in optimal control theory.

The primer vector  $\mathbf{p}(t)$  represents the costate associated with velocity in the Hamiltonian formulation of the trajectory optimisation problem. For problems involving impulsive velocity increments, such as multiple burn transfers, the primer vector must satisfy specific boundary conditions at each impulse location. According to Lawden's necessary conditions, at any impulse time  $t_i$ , the primer vector direction must align with the velocity increment direction [71]:

$$\mathbf{p}(t_i) = \frac{\Delta \mathbf{v}_i}{|\Delta \mathbf{v}_i|} \quad (4.2)$$

The primer vector magnitude provides crucial information about trajectory optimality. For an optimal trajectory, the primer magnitude must satisfy  $|\mathbf{p}(t)| \leq 1$  throughout the transfer, with equality holding at impulse locations. When  $|\mathbf{p}(t)| > 1$  at intermediate times, additional impulses are required to achieve optimality [71].

The evolution of the primer vector between impulses follows the same dynamics as state perturbations, governed by the state transition matrix (STM). For a two-body system, the primer vector and its time derivative satisfy:

$$\begin{bmatrix} \dot{\mathbf{p}} \\ \mathbf{p} \end{bmatrix} = \begin{bmatrix} \mathbf{0} & \mathbf{I} \\ \mathbf{G} & \mathbf{0} \end{bmatrix} \begin{bmatrix} \mathbf{p} \\ \dot{\mathbf{p}} \end{bmatrix} \quad (4.3)$$

where  $\mathbf{G}$  is the gravity gradient matrix already used in Sec. 3.4.2.2.

In the context of multiple Enceladus flybys, primer vector theory can systematically identify when additional trajectory correction manoeuvres (TCMs) would improve optimality. Rather than limiting analysis to predetermined burn locations, the primer magnitude history reveals natural locations for intermediate burns. This approach enables the development of fuel-optimal multi-burn sequences that account for the complex n-body dynamics during extended mission phases.

The implementation would involve propagating both the state vector and the augmented primer vector dynamics simultaneously, then analysing the primer magnitude profile to

identify violations of the optimality condition. When integrated with the existing STM-based convergence methods, this creates a comprehensive framework for designing optimal multi-burn transfer sequences between successive Enceladus encounters [72].

# References

- [1] A. J. Coates, ‘Cassini–huygens: Saturn, rings and moons,’ *Astronomy & Geophysics*, vol. 58, no. 4, pp. 4.18–4.24, 2017. DOI: 10.1093/astrogeo/atx142.
- [2] A. Coustenis et al., ‘The exploration of habitable worlds with future space missions,’ *Philosophical Transactions of the Royal Society A: Mathematical, Physical and Engineering Sciences*, vol. 374, no. 2072, p. 20 150 392, 2016. DOI: 10.1098/rsta.2015.0392.
- [3] L. J. Spilker, ‘Cassini–huygens exploration of the saturn system: 13 years of discovery,’ *Science*, vol. 364, no. 6445, pp. 1046–1051, 2019. DOI: 10.1126/science.aat3760.
- [4] M. G. Tomasko et al., ‘Rain, winds, and haze during the huygens probe’s descent to titan’s surface,’ *Nature*, vol. 438, no. 7069, pp. 765–778, 2005. DOI: 10.1038/nature04126.
- [5] J. H. Waite et al., ‘The process of tholin formation in titan’s upper atmosphere,’ *Science*, vol. 316, no. 5826, pp. 870–875, 2007. DOI: 10.1126/science.1139727.
- [6] F. Postberg et al., ‘A salt–water reservoir as the source of a compositionally stratified plume on enceladus,’ *Nature*, vol. 474, no. 7353, pp. 620–622, 2011. DOI: 10.1038/nature10175.
- [7] J. H. Waite et al., ‘Liquid water on enceladus from observations of ammonia and  $^{40}\text{Ar}$  in the plume,’ *Nature*, vol. 460, no. 7254, pp. 487–490, 2009. DOI: 10.1038/nature08153.
- [8] V. Lainey et al., ‘A recently formed ocean on saturn’s moon mimas,’ *Nature*, vol. 626, no. 7998, pp. 280–282, 2024. DOI: 10.1038/s41586-023-06975-9.
- [9] C. P. McKay et al., ‘The search for life in the saturn system: A nasa perspective,’ *Astrobiology*, vol. 16, no. 6, pp. 441–443, 2016. DOI: 10.1089/ast.2016.1487.
- [10] ESA Voyage 2050 Senior Committee, ‘Voyage 2050: A long-term plan for space science at esa for the period 2035–2050,’ European Space Agency, Tech. Rep., 2021. [Online]. Available: <https://www.cosmos.esa.int/documents/1866264/1866292/Voyage2050-Senior-Committee-report-public.pdf>.
- [11] M. Blanc et al., ‘The voyage 2050 long–term plan for the esa science programme,’ *Experimental Astronomy*, vol. 54, pp. 539–574, 2022. DOI: 10.1007/s10686-021-09765-5.

- [12] NASA Science Editorial Team. ‘Cassini at enceladus: A decade-plus of discovery,’ Accessed: 26th Aug. 2024. [Online]. Available: <https://science.nasa.gov/missions/cassini/cassini-at-enceladus-a-decade-plus-of-discovery/>.
- [13] The MIDAS Development Team. ‘Midas.design.reso — midas 1.3.0 documentation.’ [Online]. Available: [https://midas.io.esa.int/midas/api\\_reference/generated/midas.design.reso.html](https://midas.io.esa.int/midas/api_reference/generated/midas.design.reso.html).
- [14] GIGANTES Development Team, ‘Gigantes flyby mission technical report,’ Deimos Space, Tech. Rep., 2024.
- [15] M. Grötschel et al., *The Travelling Salesman Problem: A Guided Tour of Combinatorial Optimization*, E. L. Lawler et al., Eds. New York: Wiley, 1985.
- [16] A. Bellome, ‘Trajectory design of multi-target missions via graph transcription and dynamic programming,’ PhD thesis, Cranfield University, Dec. 2022.
- [17] M. Ceriotti, ‘Global optimisation of multiple gravity assist trajectories,’ PhD thesis, University of Glasgow, 2010.
- [18] N. Bradley et al., ‘A continuation method for converting trajectories from patched conics to full gravity models,’ *The Journal of the Astronautical Sciences*, vol. 61, no. 3, pp. 227–254, 2014. DOI: 10.1007/s40295-014-0017-x.
- [19] European Space Agency (ESA), *GODOT (General Orbit Determination Online Tool) Software Documentation*, 2024. [Online]. Available: <https://godot.io.esa.int/docs/1.4.0/>.
- [20] NASA Science. ‘Saturn: Facts,’ Accessed: 26th Aug. 2024. [Online]. Available: <https://science.nasa.gov/saturn/facts/>.
- [21] J. P. Sanchez Cuartielles et al., ‘Automated design of pseudo-orbiter phases for ocean world’s global mapping,’ in *75th International Astronautical Congress (IAC)*, Milan, Italy, 2024.
- [22] NASA Science. ‘Enceladus: In depth.’ Image captured by the Cassini spacecraft in 2008., Accessed: 26th Aug. 2024. [Online]. Available: <https://science.nasa.gov/saturn/moons/enceladus/>.
- [23] S. E. Urban et al., Eds., *Explanatory Supplement to the Astronomical Almanac*, 3rd. Mill Valley, CA: University Science Books, 2013.
- [24] NASA Navigation and Ancillary Information Facility. ‘Cassini pck kernel for ence-ladus: Enceladus\_ssd\_230702\_v1.tpc.’ [Online]. Available: [https://naif.jpl.nasa.gov/pub/naif/CASSINI/kernels/pck/enceladus\\_ssd\\_230702\\_v1.tpc](https://naif.jpl.nasa.gov/pub/naif/CASSINI/kernels/pck/enceladus_ssd_230702_v1.tpc).
- [25] T. Muneer, *Solar Radiation and Daylight Models*, 2nd. London: Routledge, 2007, ISBN: 9780080474410. DOI: 10.4324/9780080474410.
- [26] D. A. Vallado, *Fundamentals of Astrodynamics and Applications*, 4th. Hawthorne, CA: Microcosm Press, 2013, ISBN: 978-1881883180.
- [27] R. S. Park et al., ‘The global shape, gravity field, and libration of Enceladus,’ *Journal of Geophysical Research: Planets*, vol. 129, no. 1, 2024. DOI: 10.1029/2023JE008054.

- [28] D. R. Williams. ‘Saturnian satellite fact sheet,’ NASA Space Science Data Coordinated Archive, Accessed: 25th Aug. 2024. [Online]. Available: <https://nssdc.gsfc.nasa.gov/planetary/factsheet/saturniansatfact.html>.
- [29] NASA Navigation and Ancillary Information Facility (NAIF). ‘Required Reading: Rotation,’ Accessed: 26th Aug. 2024. [Online]. Available: [https://naif.jpl.nasa.gov/pub/naif/toolkit\\_docs/C/req/rotation.html](https://naif.jpl.nasa.gov/pub/naif/toolkit_docs/C/req/rotation.html).
- [30] B. A. Archinal et al., ‘Correction to: Report of the IAU working group on cartographic coordinates and rotational elements: 2015,’ *Celestial Mechanics and Dynamical Astronomy*, vol. 131, no. 12, p. 61, 2019. DOI: 10.1007/s10569-019-9925-1.
- [31] J. Oberst et al., ‘Enceladus geodetic framework,’ *The International Archives of the Photogrammetry, Remote Sensing and Spatial Information Sciences*, vol. XLII-3/W1, pp. 113–118, 2017. DOI: 10.5194/isprs-archives-XLII-3-W1-113-2017.
- [32] NASA Navigation and Ancillary Information Facility (NAIF). ‘cspice\_subslr: IDL Sub-Solar Point Computation,’ Accessed: 26th Aug. 2024. [Online]. Available: [https://naif.jpl.nasa.gov/pub/naif/toolkit\\_docs/IDL/icy/cspice\\_subslr.html](https://naif.jpl.nasa.gov/pub/naif/toolkit_docs/IDL/icy/cspice_subslr.html).
- [33] NASA Navigation and Ancillary Information Facility (NAIF). ‘CSPICE edterm\_c: Ellipse and Terminator Computation,’ Accessed: 26th Aug. 2024. [Online]. Available: [https://naif.jpl.nasa.gov/pub/naif/toolkit\\_docs/C/cspice/edterm\\_c.html](https://naif.jpl.nasa.gov/pub/naif/toolkit_docs/C/cspice/edterm_c.html).
- [34] J. O’Callaghan. ‘Lunar eclipse guide: What they are, when to see them and where,’ Accessed: 26th Aug. 2024. [Online]. Available: <https://www.nhm.ac.uk/discover/lunar-eclipse-guide-what-they-are-when-to-see-them-and-where.html>.
- [35] Stellarium Project, *Stellarium*. [Online]. Available: <https://stellarium.org/fr/>.
- [36] Celestia Project, *Celestia*. [Online]. Available: <https://celestia.space>.
- [37] S. E. Urban et al., ‘Eclipses,’ in *Explanatory Supplement to the Astronomical Almanac*, S. E. Urban et al., Eds., 3rd, University Science Books, 2012, ch. 11, ISBN: 978-1891389856.
- [38] W. M. Smart, ‘Eclipses and occultations,’ in *Textbook on Spherical Astronomy*, R. M. Green, Ed., 6th, Cambridge University Press, 1977, ch. 15, ISBN: 978-0521291804.
- [39] A. Safiya Beevi et al., ‘Oblateness effect of Saturn on periodic orbits in the Saturn-Titan restricted three-body problem,’ *Astrophysics and Space Science*, vol. 340, no. 2, pp. 245–261, Aug. 2012. DOI: 10.1007/s10509-012-1052-3.
- [40] J. Sun et al., ‘A high-accuracy and high-efficiency satellite shadow function model for oblate earth,’ *Journal of Guidance, Control, and Dynamics*, vol. 45, no. 8, pp. 1565–1573, 2022. DOI: 10.2514/1.I011271.

- [41] NASA Navigation and Ancillary Information Facility (NAIF), *Gfoclt\_c*, 2021. [Online]. Available: [https://naif.jpl.nasa.gov/pub/naif/toolkit\\_docs/C/cspice/gfoclt\\_c.html](https://naif.jpl.nasa.gov/pub/naif/toolkit_docs/C/cspice/gfoclt_c.html).
- [42] NASA Navigation and Ancillary Information Facility (NAIF), *Spice time subsystem*, 2021. [Online]. Available: [https://naif.jpl.nasa.gov/pub/naif/toolkit\\_docs/FORTRAN/req/time.html](https://naif.jpl.nasa.gov/pub/naif/toolkit_docs/FORTRAN/req/time.html).
- [43] NASA Navigation and Ancillary Information Facility (NAIF), *About spice*, Accessed: Aug. 26, 2024, Jet Propulsion Laboratory, California Institute of Technology, 2024. [Online]. Available: <https://naif.jpl.nasa.gov/naif/aboutspice.html>.
- [44] S. Campagnola et al., ‘Endgame problem part 2: Multibody technique and the tisserand-poincare graph,’ *Journal of Guidance, Control, and Dynamics*, vol. 33, no. 2, pp. 476–486, 2010. DOI: 10.2514/1.44290.
- [45] D. H. Ellison et al., ‘High-fidelity multiple-flyby trajectory optimization using multiple-shooting,’ in *AIAA/AAS Astrodynamics Specialist Conference*, Aug. 2019. DOI: 10.2514/6.2019-4033.
- [46] N. J. Strange, ‘Analytical methods for gravity-assist tour design,’ Jet Propulsion Laboratory, California Institute of Technology, Tech. Rep. JPL D-31233, 2016.
- [47] F. Peralta et al., ‘Cassini interplanetary trajectory design,’ *Control Engineering Practice*, vol. 3, no. 11, pp. 1603–1610, 1995. DOI: 10.1016/0967-0661(95)00171-P.
- [48] R. V. Domingos et al., ‘A comparison of averaged and full models to study the third-body perturbation,’ *Mathematical Problems in Engineering*, vol. 2013, 2013. DOI: 10.1155/2013/260830.
- [49] R. H. Battin, *An Introduction to the Mathematics and Methods of Astrodynamics*, Revised. AIAA, 1999. DOI: 10.2514/4.861543.
- [50] C. R. McInness et al., *Solar radiation pressure - an overview*, <https://www.sciencedirect.com/topics/engineering/solar-radiation-pressure>, Accessed: Aug. 26, 2024, 2024.
- [51] N. A. F. Senan, ‘A brief introduction to using ode45 in MATLAB,’ University of California at Berkeley, Department of Mechanical Engineering, Tech. Rep.
- [52] M. E. Paskowitz et al., ‘Design of science orbits about planetary satellites: Application to europa,’ *Journal of Guidance, Control, and Dynamics*, vol. 29, no. 5, pp. 1147–1158, 2006. DOI: 10.2514/1.19464.
- [53] R. P. Russell et al., ‘Circulating eccentric orbits around planetary moons,’ *Journal of Guidance, Control, and Dynamics*, vol. 32, no. 2, pp. 423–435, 2009. DOI: 10.2514/1.38593.
- [54] M. Lara et al., ‘Dynamic behavior of an orbiter around europa,’ *Journal of Guidance, Control, and Dynamics*, vol. 28, no. 2, pp. 291–297, 2005. DOI: 10.2514/1.5686.
- [55] B. Buffington, ‘Trajectory design for the europa clipper mission concept,’ in *AIAA/AAS Astrodynamics Specialist Conference*, 2014. DOI: 10.2514/6.2014-4105.

- [56] T. R. Spilker et al., ‘Enabling saturnian moon tours with titan aerogravity assist,’ in *AAS/AIAA Astrodynamics Specialist Conference*, 2013.
- [57] T. Chikazawa et al., ‘B–plane assisted trajectory design with analytical mapping of swing-by parameters,’ *Advances in Space Research*, vol. 74, no. 1, 2024. DOI: 10.1016/j.asr.2024.06.061.
- [58] W. Kizner, ‘A method of describing miss distance for lunar and interplanetary trajectories,’ Jet Propulsion Laboratory, California Institute of Technology, Pasadena, CA, Tech. Rep. External Publication No. 674, 1969.
- [59] B. D. Tapley et al., *Statistical Orbit Determination*. Burlington: Academic Press, 2004, ISBN: 978-0-12-683630-1.
- [60] E. Pellegrini et al., ‘On the computation and accuracy of trajectory state transition matrices,’ *Journal of Guidance, Control, and Dynamics*, vol. 39, no. 11, pp. 2485–2499, 2016. DOI: 10.2514/1.G001920.
- [61] A. S. Weeks, ‘Interplanetary trajectory optimization using a genetic algorithm,’ Master’s thesis, The Pennsylvania State University, 2005.
- [62] C. M. A. Deccia, ‘Analysis of the sun-earth lagrangian environment for the new worlds observer (nwo),’ M.S. thesis, Delft University of Technology, 2017. [Online]. Available: <https://resolver.tudelft.nl/uuid:b5b2b94b-3982-4457-a56f-51b5b3574f51>.
- [63] J. S. Parker et al., *Low-Energy Lunar Trajectory Design* (JPL Deep-Space Communications and Navigation Series). Pasadena, California: Wiley, 2013, ISBN: 978-1-118-85532-4.
- [64] F. L. Markley, ‘Approximate cartesian state transition matrix,’ *The Journal of the Astronautical Sciences*, vol. 34, no. 2, pp. 161–169, 1986.
- [65] T. Soler, ‘A matrix representation of the potential second-rank gradient tensor for local modelling,’ *Geophysical Journal International*, vol. 81, no. 2, pp. 363–379, 1985.
- [66] P. Chen et al., ‘Gravity gradient tensor eigendecomposition for spacecraft positioning,’ *Journal of Guidance, Control, and Dynamics*, vol. 38, no. 11, pp. 2200–2206, 2015. DOI: 10.2514/1.G001195.
- [67] D.-H. Cho et al., ‘Trajectory correction maneuver design using an improved b–plane targeting method,’ *Acta Astronautica*, vol. 72, pp. 47–61, 2012. DOI: 10.1016/j.actaastro.2011.11.009.
- [68] J. S. Golan, ‘The moore-penrose pseudoinverse,’ in *Foundations of Linear Algebra*, ser. Kluwer Texts in the Mathematical Sciences, vol. 11, Kluwer Academic Publishers, 2001, pp. 198–203.
- [69] The MathWorks, Inc., *Pinv - moore-penrose pseudoinverse - matlab*, Sep. 2025. [Online]. Available: <https://www.mathworks.com/help/matlab/ref/pinv.html>.
- [70] D. F. Lawden, *Optimal Trajectories for Space Navigation*. London: Butterworths, 1963.

- [71] R. J. Whitley et al., ‘Direct multiple shooting optimization with variable problem parameters,’ in *AIAA/AAS Astrodynamics Specialist Conference and Exhibit*, Honolulu, Hawaii, 2008. DOI: 10.2514/6.2008-6878.
- [72] L. A. Hiday-Johnston et al., ‘Impulsive time-free transfers between halo orbits,’ *Celestial Mechanics and Dynamical Astronomy*, vol. 64, pp. 281–303, 1996.
- [73] NASA Navigation and Ancillary Information Facility (NAIF). ‘Planetary constants kernel (pck) file for cassini mission.’ Referencing Saturn body parameters (BODY699\_RADII) within file cpck25Mar2010.tpc. [Online]. Available: [https://naif.jpl.nasa.gov/pub/naif/pds/data/co-s\\_j\\_e\\_v-spice-6-v1.0/cosp\\_1000/data/pck/cpck25Mar2010.tpc](https://naif.jpl.nasa.gov/pub/naif/pds/data/co-s_j_e_v-spice-6-v1.0/cosp_1000/data/pck/cpck25Mar2010.tpc).

# Appendix A

## Ethical Approval Letter



15 May 2025

Dear Mr Ferrara ,

Reference: CURES/25156/2025

Project ID: 28213

Title: trajectory design enceladus with linked conics

We are pleased to inform you that you have successfully declared that your research project is a **Literature Review – based solely on openly available literature which is in the public domain, and you are undertaking desk-based research not involving any other form of data or information.**

You have also confirmed that your project **does not meet** any of the literature review specified exceptions, listed both within the relevant section of the CURES form and below:

1) Your supervisor has requested that you apply for approval through CURES because:

- The journals or data are in a sensitive area (please discuss this with your supervisor)
- The project will be embargoed i.e. **will not be publicly available via the Cranfield library immediately or longer term**

2) Approval is/will be specifically required by another external body e.g. journal publishers

Therefore, **you do not require ethical approval** and your CURES application will be automatically closed.

**Please keep a copy of this letter safe, if this exception is in relation to your thesis project, you will need to include a copy with your final thesis submission.**

If you have any queries, please contact CURES Support.

We wish you every success with your project.

Regards,

CURES Team

## Appendix B

# Mathematical Derivation of Saturn's Angular Size

This appendix presents a rigorous mathematical derivation of the expression for the angular size  $\delta$  of an oblate Saturn as observed from the surface of Enceladus.

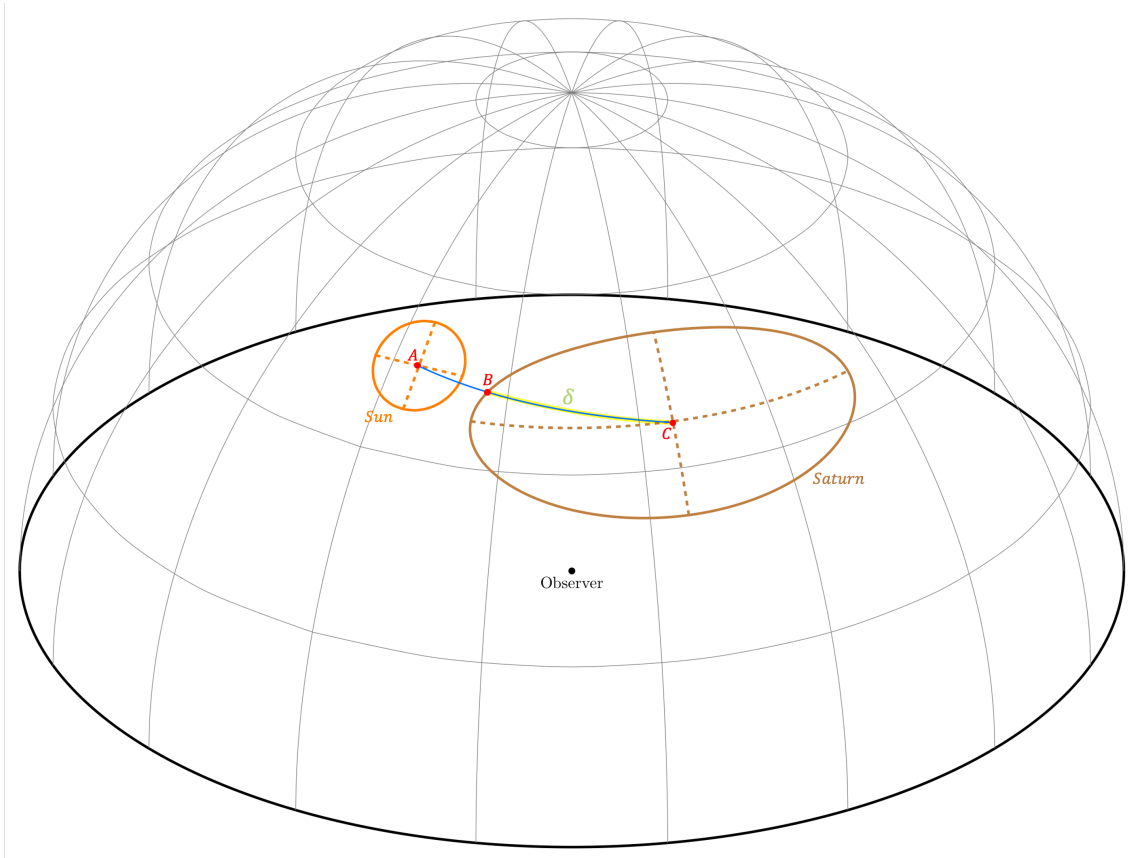


Figure B.1: Schematic representation of a spherical Sun and oblate Saturn projected onto the celestial sphere as observed from the surface of Enceladus. Sizes and proportions are not to scale

## B.1 Geometric Setup

Within the SPICE kernel framework, Saturn is represented as a triaxial ellipsoid defined by three principal radii[73]:

$$\text{BODY699\_RADII} = (60268, 60268, 54364) \text{ km}$$

Given the negligible difference between the two equatorial radii, Saturn may be suitably approximated as an oblate spheroid with an equatorial radius  $R_{eq}$  and a polar radius  $R_{pol}$ . This simplification is adopted throughout the subsequent derivation.

A reference frame is established such that the observer, located at a point on the surface of Enceladus, is positioned at the origin  $(0, 0, 0)$ . The centre of the spheroid (Saturn) is placed along the  $x$ -axis at a distance  $d$  from the observer.

This configuration is justified by the assumption that Saturn’s equatorial plane is coplanar with Enceladus’ orbital plane. This assumption remains valid even under the  $n$ -body problem, as Enceladus’ actual orbital inclination is only  $0.0086^\circ$ [31], resulting in a maximum latitude error of  $10^{-4}$ . This value was calculated by comparing the SPICE-derived latitude of Enceladus’ sub-Saturn point with the latitude computed under the simplified Saturn-centric reference frame detailed in Section 2.1.2, and by varying the epoch over a 10-year sweep with 10,000 points.

The equation describing Saturn as a spheroid centred at  $(d, 0, 0)$  is given by:

$$\frac{(x-d)^2}{R_{eq}^2} + \frac{y^2}{R_{eq}^2} + \frac{z^2}{R_{pol}^2} = 1 \quad (\text{B.1})$$

where  $R_{eq}$  denotes the equatorial radius and  $R_{pol}$  the polar radius of Saturn.

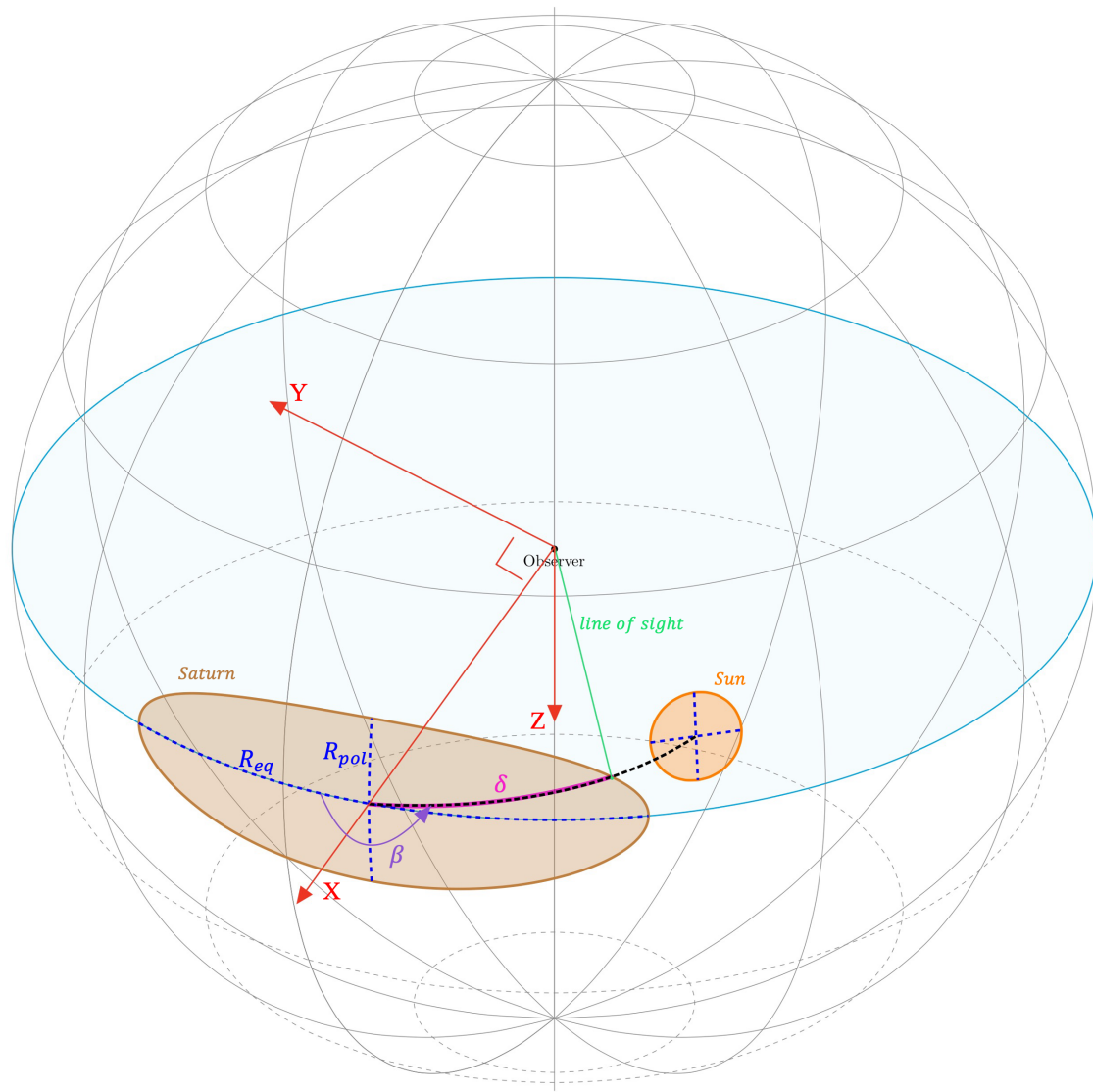


Figure B.2: Schematic representation of the reference frame with Saturn, its radii, and angles. Sizes and proportions are not to scale.

## B.2 Tangency Condition

A line of sight from the observer is represented as a ray originating at the origin, defined by a direction unit vector  $\mathbf{u} = (u_x, u_y, u_z)$  and a scalar parameter  $t$ :

$$\begin{pmatrix} x \\ y \\ z \end{pmatrix} = t \begin{pmatrix} u_x \\ u_y \\ u_z \end{pmatrix} \quad (\text{B.2})$$

The limb of Saturn corresponds to lines of sight tangent to its surface, i.e., rays that intersect the spheroid at exactly one point. Substituting the ray equation into the spheroid equation yields a quadratic in  $t$ :

$$\frac{(u_x t - d)^2}{R_{eq}^2} + \frac{(u_y t)^2}{R_{eq}^2} + \frac{(u_z t)^2}{R_{pol}^2} = 1 \quad (\text{B.3})$$

The coefficients are:

$$\begin{aligned} A &= \frac{u_x^2 + u_y^2}{R_{eq}^2} + \frac{u_z^2}{R_{pol}^2} \\ B &= -\frac{2du_x}{R_{eq}^2} \\ C &= \frac{d^2}{R_{eq}^2} - 1 \end{aligned} \quad (\text{B.4})$$

The tangency condition requires the discriminant to be equal to zero:

$$B^2 - 4AC = 0 \quad (\text{B.5})$$

### B.3 Spherical coordinate angles

The direction vector  $\mathbf{u}$  can be also expressed in spherical coordinates:

$$\begin{aligned} u_x &= \cos(\delta) \\ u_y &= \sin(\delta) \cos(\beta) \\ u_z &= \sin(\delta) \sin(\beta) \end{aligned} \quad (\text{B.6})$$

where:

- $\delta$  denotes the angular separation between the line of sight and the  $z$ -axis. In the context of eclipse geometry  $\delta$  is the angular size from Saturn centre to its limb with  $\beta$  direction.
- $\beta$  specifies the position angle measured around the spheroid's centre, with  $\beta = 0$  corresponding to the equatorial plane and  $\beta = 90^\circ$  corresponding to the polar direction. In the context of eclipse geometry,  $\beta$  is equivalent to the Sun elevation angle as seen from the observer's location.

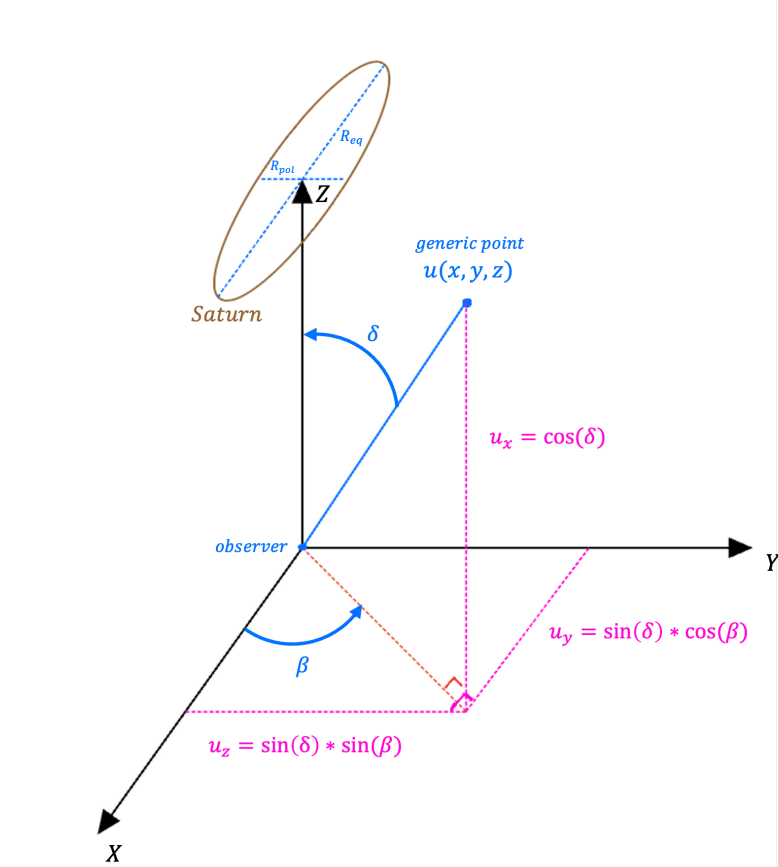


Figure B.3: Schematic of the spherical coordinates angles  $\delta$  and  $\beta$ .

## B.4 Derivation

Substituting the tangency condition B.5 and simplifying gives:

$$\frac{d^2 u_x^2}{R_{eq}^2} = (d^2 - R_{eq}^2) \left( \frac{u_x^2 + u_y^2}{R_{eq}^2} + \frac{u_z^2}{R_{pol}^2} \right) \quad (\text{B.7})$$

Substituting the spherical coordinates of **u** B.6 and dividing by  $\cos^2(\delta)$  yields:

$$\frac{d^2}{d^2 - R_{eq}^2} = 1 + \tan^2(\delta) \left( \cos^2(\beta) + \sin^2(\beta) \frac{R_{eq}^2}{R_{pol}^2} \right) \quad (\text{B.8})$$

Solving for  $\tan^2(\delta)$ :

$$\tan^2(\delta) = \frac{R_{eq}^2}{(d^2 - R_{eq}^2) \left( \cos^2(\beta) + \sin^2(\beta) \frac{R_{eq}^2}{R_{pol}^2} \right)} \quad (\text{B.9})$$

The denominator can be rewritten as:

$$\cos^2(\beta) + \sin^2(\beta) \frac{R_{eq}^2}{R_{pol}^2} = \frac{R_{pol}^2 \cos^2(\beta) + R_{eq}^2 \sin^2(\beta)}{R_{pol}^2} \quad (\text{B.10})$$

Thus, **the final formula is obtained**:

$$\delta(\beta) = \arctan \left( \frac{R_{eq} R_{pol}}{\sqrt{(d^2 - R_{eq}^2)(R_{pol}^2 \cos^2(\beta) + R_{eq}^2 \sin^2(\beta))}} \right) \quad (\text{B.11})$$

where  $d$  is the distance from the observer on Enceladus' surface to Saturn's limb.

## B.5 Verification

To ensure the validity of the derived expression an analytical and limiting-case verification is performed.

### B.5.1 Trigonometric Identity

Consider the right triangle depicted in Figure B.4. The angular radius  $\alpha$  subtended by a sphere of radius  $R$  at a distance  $d$  from the observer can be expressed as:

$$\begin{aligned}\alpha &= \arctan\left(\frac{R}{\sqrt{d^2 - R^2}}\right) \\ \alpha &= \arcsin\left(\frac{R}{d}\right)\end{aligned}\tag{B.12}$$

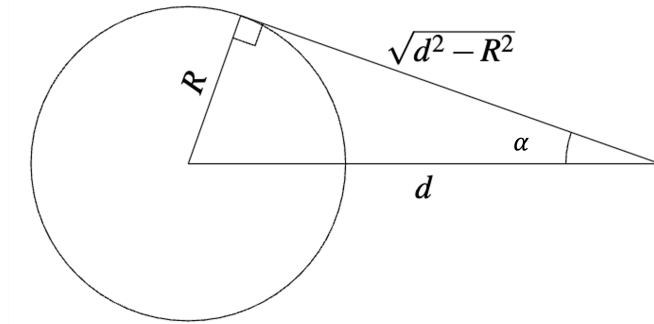


Figure B.4: Right triangle tangent to a spherical body of radius  $R$  at a distance  $d$  from the observer.

This leads to the following trigonometric identity:

$$\arcsin\left(\frac{R}{d}\right) = \arctan\left(\frac{R}{\sqrt{d^2 - R^2}}\right)\tag{B.13}$$

### B.5.2 Equatorial Direction ( $\beta = 0$ )

For  $\beta = 0$  (i.e., the equatorial direction), equation (B.11) reduces to:

$$\delta_{eq} = \arctan \left( \frac{R_{eq}}{\sqrt{d^2 - R_{eq}^2}} \right) \quad (\text{B.14})$$

By equation (B.13), this is equivalent to  $\arcsin \left( \frac{R_{eq}}{d} \right)$ , which is the correct angular radius for a sphere of radius  $R_{eq}$  (add reference)

### B.5.3 Polar Direction ( $\beta = 90^\circ$ )

For  $\beta = 90^\circ$  (i.e., the polar direction), equation (B.11) reduces to:

$$\delta_{pol} = \arctan \left( \frac{R_{pol}}{\sqrt{d^2 - R_{pol}^2}} \right) \quad (\text{B.15})$$

Similarly, by equation (B.13), this is equivalent to  $\arcsin \left( \frac{R_{pol}}{d} \right)$ , which is the correct angular radius for a sphere of radius  $R_{pol}$  (add reference).

These limiting cases confirm the consistency of the general formula.